UNIVERSIDAD DE CHILE
FACULTAD DE CIENCIAS FÍSICAS Y MATEMÁTICAS
DEPARTAMENTO DE ASTRONOMÍA

STUDY OF SURFACE PROPERTIES AS PROBES OF SOLAR SYSTEM DYNAMICAL EVOLUTION

TESIS PARA OPTAR AL GRADO DE DOCTOR EN
CIENCIAS, MENCIÓN ASTRONOMÍA

JOSÉ MIGUEL PEÑA ZAMUDIO

PROFESOR GUÍA:
CESAR FUENTES GONZÁLEZ

MIEMBROS DE LA COMISIÓN:
DAVID TRILLING
FRANCISCO FÖRSTER BURÓN
ANDRÉS JORDAN COLZANI
PATRICIO ROJO RUBKE

Este trabajo ha sido parcialmente financiado por ANID, CATA, DAS, MAS & CMM

SANTIAGO DE CHILE
2022

RESUMEN DE LA MEMORIA PARA OPTAR AL
GRADO DE DOCTOR EN CIENCIAS, MENCIÓN ASTRONOMÍA
POR: JOSÉ MIGUEL PEÑA ZAMUDIO
FECHA: 2022
PROF. GUÍA: CESAR FUENTES GONZÁLEZ

ESTUDIO DE PROPIEDADES DE SUPERFICIES COMO APROXIMACIÓN A LA EVOLUCIÓN DINÁMICA DEL SISTEMA SOLAR

Nuestro conocimiento del Sistema Solar ha aumentado mucho el último tiempo, desde la caracterización de millones de cuerpos del Cinturón de Asteroides hasta el número cada vez mayor de objetos transneptunianos descubiertos. Estos "cuerpos menores", al llevar en sus distribuciones y características las huellas de la evolución del Sistema Solar, son vitales para entender la historia de este. Los modelos actuales de su evolución han tenido éxito en explicar mucho de las características dinámicas de los cuerpos menores, pero aun no han sido bien testeados para explicar sus características físicas (como composición y tamaño), las cuales aun son desconocidas para la muchos de estos objetos. En este trabajo muestro resultados obtenidos de estudiar objectos del Cinturón de Asteroides y satélites irregulares de Saturno, obteniendo colores en ambos casos y tamaños para los asteroides.

Los asteroides fueron detectados dentro del catálogo de fuentes móviles del High Cadence Transient Survey (HiTS, mapeo diseñado para encontrar supernovas). Conectando diferentes detecciones dentro y entre noches se logró detectar alrededor de 20.000 objetos candidatos de ser asteroides (cada uno de ellos de tres o más detecciones), logrando restringir la órbita para unos 9400, perteneciendo la gran mayoría de ellos al Cinturón. La gran mayoría de los candidatos (unos 13.000) fueron encontrados cerca de la eclíptica, mostrando una distribución de luminosidad y de tamaño (para aquellos a los que se les pudo restringir su órbita) similar a las encontradas en la literatura. Observando 5° lejos de la eclíptica se encontraron muchos menos objetos, los cuales muestran pendientes mucho mayores en sus distribuciones de luminosidad y tamaño, lo cual se asume que se debe a la mayor latitud observada. Para estos últimos objetos también se obtuvo colores, sin poder encontrar una relación entre este y su tamaño (para asteroides de entre 1 y 10 km). Sin embargo estos colores están fuertemente afectados por la rotación natural de los asteroides. Se encontró que para medir colores de asteroides las observaciones en diferentes bandas no deberían alejarse más de 14 minutos la una de la otra. Estos resultados muestran la gran utilidad que tienen mapeos como HiTS, o en el futuro cercano el LSST, para estudiar cuerpos menores.

Finalmente se observaron satélites irregulares de Saturno para obtener sus colores. Se midieron colores para 21 satélites, siendo la primera vez para 4 de ellos. Es la mayor cantidad de colores reportados en un único mapeo para estos cuerpos. Los colores reportados son consistentes con los de otros satélites irregulares, fortaleciendo la perspectiva de que no existen satélites ultra rojos, lo que los separaría de los objetos transneptunianos (su supuesta población originaria). Para lograr estos resultados se diseñó un algoritmo para detectar fuentes débiles bajo significativo brillo de fondo y en campos muy poblados de otras fuentes.

Abstract

STUDY OF SURFACE PROPERTIES AS PROBES OF SOLAR SYSTEM DYNAMICAL EVOLUTION

From the characterization of millions of Main Belt asteroids until increasing number of transneptunian objects discovered, our knowledge of the Solar System has greatly increased the last years. Those "minor bodies" are vital to understand the evolution of the Solar System since they carry the scars of its evolution on their distributions and characteristics. Current models had fairly succeeded to explain much of the dynamical characteristics of the minor bodies, but they have not been well tested to explain the physical characteristics of those populations, like their composition and sizes (that are still unknown for many of them). In this work I show results obtained from studying Main Belt asteroids and Saturn's irregular satellites, measuring colors for both cases and sizes for the asteroids.

Asteroids were detected within the moving sources catalogs from the High Cadence Transient Survey (HiTS), which is a survey designed to discover Supernovae. Around 20,000 asteroid candidates (composed by three detections or more) were found by connecting sources through and between nights, succeeding to constrain the orbits for ∼9400 of them (mostly Main Belt asteroids). Most of the candidates (around 13,000) were found near the ecliptic and show a luminosity distribution similar as those found in the literature; the same for the size distribution for those asteroids with constrained orbits. Asteroids found farther than 5° from the ecliptic are much less numerous and show luminosity and size distributions much more steeper, which is assumed to be caused by the higher latitude observed. Colors were also obtained for the latter, without finding any evidence of a size–color relationship (for bodies with sizes between 1 and 10 km). But these colors are strongly affected by the asteroids rotation. It was found that to measure colors of asteroids, the observations in different bands should not be made more than 14 minutes apart.

Finally, to study their colors, Saturn Irregular Satellites were observed. Colors were measured for 21 satellites, among them, 4 previously unreported. This is the highest number of Saturn Irregular satellites reported in a single survey. The reported colors are consistent with other irregular satellites, reinforcing the observation that the lack of ultra red objects among the irregular satellites is a real feature that separates them from the trans–Neptunian objects (their posited source population). To accomplish these measurements a technique was designed to detect faint sources under significant background noise and in front of a severely crowded field.

Dedicado a todos quienes me acompañaron
a lo largo de estos años.

Agradecimientos

Ante todo, agradezco a mi familia. A mi padre y a mi madre, por su amor, guía, educación y apoyo que sin falta, siempre me han otorgado. Por ellos he llegado hasta acá. A mis hermanas, que siempre me apoyaron y me acompañaron.

Agradezco a todos los que forman parte del Cerro Calán, a sus docentes y funcionarios. Agradezco a mis compañeros que me acompañaron en mis estudios y que se convirtieron en mis amigos: a Jorge, Matías, Sebastián, Juan, Juanpi y Grecco. También a mis compañeros de oficina con quienes compartí la mayor parte del tiempo, con quienes estudié, debatí y jugué, quienes hacían del Cerro un lugar al que daban ganas ir, a pesar de la distancia: Dani, Bica, Pía, Pato, Nico Kurtovic, Max, Ricardo y Sudeep.

Agradezco a quienes me guiaron durante mis estudios. A Francisco Förster, quien me acompañó en mis primeros pasos y me mostró lo que significa hacer astronomía. Especialmente agradezco a Cesar Fuentes, mi profesor guía, quien haciendo honor a su título, me guió durante mi desarrollo como astrónomo. Guió mis trabajo para que lo desarrollara de la mejor manera. Me dio el espacio para formar mi pensamiento crítico. Incentivó el debate abierto y dinámico. Siempre estuvo dispuesto a ayudarme y apoyarme cuando lo necesité. Muchas gracias.

Para terminar, agradezco al Departamento de Astronomía de la Universidad de Chile, a Conicyt/Anid y a CATA, por darme el sostén educativo y económico que me permitió el privilegio de estudiar astronomía sin mayores preocupaciones.

Table of Content

List of Tables

List of Figures

Chapter 1

Introduction

Many advances have been made understanding the formation and evolution of planetary systems. From the theoretical perspective (Armitage 2020 and references there in), a disk of gas and matter around a star, due to gravitational self interaction and local turbulence, starts grouping into different bodies that get bigger by accreting mass. These theories are mainly based in the Solar System, but our knowledge of other planetary systems has greatly increased over time. The NASA Exoplanet Archive[1] reports that there are ∼5,000 confirmed exoplanets exhibiting masses and orbital parameters very different to the ones observed in our Solar System. Although this is probably an observational bias, it tell us about the different evolution paths that planetary systems can follow. This can also be observed in the high variety of protoplanetary disks, as can be seen in Andrews et al. (2018); Kurtovic et al. (2018); Bohn et al. (2022). The presence of a second star, the irruption of a foreign body, the early presence of protoplanets (one or many) in the protoplanetary disk, the size, mass and metallicity of the disk are some of the many variables than can define or change the evolution of a planetary system. As can be seen in observed protoplanetary disks, the evolution from a disk of gas and dust to a "Solar-System-like" system, where the gas and dust have dissipated leaving isolated planets and rocky bodies, is not linear; planets can form before the gas has dissipated; outer planets can keep accreting gas and dust while planets in inner regions, where the gas has been dissipated, do not have that chance; growing planetesimals can be disrupted in peaces by colliding with other bodies. From a dynamical point of view, planetary migration and planetary dynamical instability are some of most important factors of a planetary system evolution. Torque interchange and pressure with the disk can trigger planet migration. Orbital evolution of the disk and its planet(s) can lead to orbital instabilities that can greatly modify these bodies' orbits (Kley & Nelson, 2012).

When you observe the Solar System it is easy to note that most of its bodies orbit in roughly the same plane as Earth (called "ecliptic" plane), which is a direct consequence of this system being originated from a planetesimal disk. To infer its evolution we need to observe its current populations. Excluding the Sun, these populations can be separated in two major groups: *planets* and *minor bodies*. According to the International Astronomical

[1] `https://exoplanetarchive.ipac.caltech.edu/`
Consulted in 03/25/2022

Union[2] (IAU) a planet (in the context of the Solar System) is a body that orbits the Sun, it has enough mass to reach a nearly round shape and has cleared its orbit out of other bodies[3]. Planets can be separated in small bodies mainly composed by minerals (the innermost four and smallest planets, Mercury, Venus, Earth and Mars) and giant bodies mainly composed by gas or low density ices (the outermost four planets, Jupiter, Saturn, Uranus and Neptune) referred as *rocky* and *giant* planets respectively. On the other hand, for the purposes of this Thesis, a minor body is any body that is not a planet[4]. Minor bodies can be separated in many different groups, the most important being the *Main Belt*, the *Trans Neptunian Objects*, the *comets*, the *centaurs* and the *satellites* (or *Moons*). The Main Belt (MB) is a disk of bodies located between Mars and Jupiter with semi-major axis roughly between 1.5 and 4.2 au; their orbits are excited, with eccentricities mostly under 0.3, inclinations mostly under 20° and sizes under 10 km with the exception of a few dozens of bodies with sizes over 200 km, with Ceres, the biggest body, with ∼900 km (values from the Minor Planet Center[5] using an albedo[6] of 0.1); there are nearly one million known MB object (although only half of them have well defined orbits), although the entire mass of the MB is estimated to be only $\sim 4 \times 10^{-4} M_{\oplus}$ (Vladimirovna Pitjeva & Petrovich Pitjev, 2015; Folkner et al., 2014); analyzing their compositions (using their spectra and colors) there have been recognized several different types of asteroids (DeMeo & Carry, 2013, 2014), being the S-type (siliceous) and the C-type (carbonaceous) the most common; it has been observed that the MB dominated by S-type asteroids in its inner regions and by C-type bodies in the outer regions. Trans Neptunias Objects (TNOs) refer to those bodies with orbits beyond Neptune (semi-major axis >30.1 au) and can be separated in many types of bodies; some of those divisions distinguish a *classic* disk of bodies with low eccentricity (<0.24) that would be what remains of the original planetesimal disk and can be separated between *cold* (inclination lower than 5°) and *hot* (dynamically excited with inclinations higher than 5°); within and beyond those populations exist the *scattered* objects (bodies in unstable orbits that are, or have been, scattered under the action of the giant planets) and the *resonant* bodies (in resonance with a giant planet, generally Neptune); these definitions do not have well established boundaries and are under constant revision (Gladman et al., 2008; Lykawka & Mukai, 2007). Centaurs are equivalent to the scattered TNOs but with semi-major axis under the 30.1 au, generally living among the giant planets (Gladman et al., 2008). Comets are bodies generally with high eccentricity that spend most of their orbits far enough from the Sun to keep icy material while getting close enough to the Sun for part of this material to sublimate, which gives them their characteristic shape when observed from the Earth. Into the minor bodies I also include the planets' *satellites*, which in contrast with those named above, instead of orbiting the Sun, they orbit a planet; they can be separated in *regulars* (spheroidal bodies with nearly circular and co-planar orbits thought to be formed along their parent planet from the same part of the primordial disk) and *irregulars* (Irrs) (bodies generally not spheroidal with orbits wider than the regulars and high eccentricities and inclination, thought to be captured by the planets from the vicinity of the planetesimal disk, Kuiper 1956)

[2] `https://www.iau.org/`

[3] Accordingly to IAU Resolution B5 (2006)
`https://www.iau.org/static/resolutions/Resolution_GA26-5-6.pdf`

[4] In this definition I also include the planets natural satellites.

[5] `https://minorplanetcenter.net/`

[6] Fraction of light coming from the Sun that is reflected by the body.

Many clues of evolution of the Solar System can be found on their different populations: gas planets are found far from the Sun because its radiation blows away most of the gases of the protoplanetary disk on its vicinity; icy bodies are found far from the Sun because ice is sublimated by the solar radiation near the Sun; empty ranges in semi-major axis across the Main Belt (called *Kirkwood Gaps*) mark orbits that are resonant with the biggest planets orbits (mainly Jupiter), where the constant revolution of these planets through their lives has removed all small bodies; planet resonances not only "clean" orbits out of bodies, they can also lock bodies in specific orbits (such as the *Plutinos*) or keep populations "safe" from the influence of other bodies (such as the *Trojans*, bodies in a 1:1 stable resonance with a planet, around its lagrangian points, while bodies outside those points have been removed by the planet); cratering history on different bodies hint to diverse collisional processes among the Solar System, such us the *Late Heavy Bombardment* from the Moon's craters (Tera et al., 1974) or the collisional history of the Irregular Satellites of Saturn (Ashton et al., 2021). Simple models predict terrestrial planets with masses similar to Earth or Venus (Chambers, 2001; Raymond et al., 2006), but failed to replicate the mass ratios between Earth and Mercury (16:1) or Earth and Mars (9:1). Planet migration tend to lead planets inward, which leads in many cases to systems that end up in very compact configurations, as can be seen in Lissauer et al. (2011) (and in the Nasa Exoplanet Archive for an updated version with confirmed planets), where most systems have *all* their members in orbits in a range of 1 to 100 days of period[7], while in our Solar System only Mercury, the innermost planet, with its period of 88 days lives in the outer edge of that range; all the other planets and minor bodies are located in much wider orbits. It is generally accepted that during their migration inward, the giant planets reach an unstable orbital configuration that sends them outward to their current positions, disrupting the planetesimal disk in the process, scattering small bodies to inner and outer orbits (Gomes et al., 2004; Tsiganis et al., 2005; Gomes et al., 2005; Levison et al., 2011). That period of migration and instability of the giant planets would be the responsible of the architecture of the current Main Belt (Gomes, 1997; Minton & Malhotra, 2009; Morbidelli et al., 2010) and TNOs (Levison et al., 2008); it also would explain the origin of Jovian Trojans (Fleming & Hamilton, 2000; Morbidelli et al., 2005), Neptunian Trojans (Lykawka & Horner, 2010; Gomes & Nesvorný, 2016) and Irregular Satellites (Nesvorný et al., 2007, 2014). These set of models (generally referred as "Nice Model" as a whole), although successful in explaining many of the Solar System characteristics, are far from completely explaining all of the Solar System's complexities. For the inner Solar System it is difficult to reconcile the existence of the inner rocky planets with a giant planet's instability, since the former could be scattered out by the latter (Kaib & Chambers, 2016) and there is still no clarity on how the Main Belt was formed or from where its bodies originally came from so that the current color trend can be explained (see Raymond et al. 2020 for a full discussion on Solar System formation in the context of protoplanetary evolution, with focus on the planets and the Main Belt). For TNOs it is still a mystery how the cold population was preserved after the giant planets instability, which is necessary to explain the excited populations (Levison et al., 2008; Wolff et al., 2012) and is hard to match simulated populations with their actual numbers (Brasser & Morbidelli, 2013).

There have been many improvements in the models of the Solar System, but there are

[7]The fact that almost all of planetary systems have members with periods under the 100 days is most likely due an observational bias (as mentioned at the beginning of this chapter). As the planets are bigger and closer to their stars is easier to detect them.

still many questions to answer. Much of the evidences of the Solar System evolution can be observed in the population of minor bodies, but our knowledge of them is far from being complete. The Main Belt is the best characterized population of minor bodies, but there is still a lack of knowledge of their smallest members (sizes of 1 km or less) and their compositions. TNOs are thought to be directly related to other populations (such as Irrs or centaurs), so knowing them is critical to understand the Solar System evolution, but up to this day[8], there are only 4160 known TNOs (much less than the million known MB objects) and knowledge of their compositions for only a small fraction of them (over 500 bodies, as seen in Peixinho et al. 2015; Pike et al. 2017; Terai et al. 2018; Chen et al. 2018; Marsset et al. 2019; Thirouin & Sheppard 2019; Buchanan et al. 2022 and reference there in). Other populations are in similar situation, such as the Irrs, that have measured colors for only half of them (Sykes et al., 2000; Rettig et al., 2001; Grav et al., 2003; Grav & Holman, 2004; Grav et al., 2004, 2015; Bauer et al., 2006; Graykowski & Jewitt, 2018; Maris et al., 2018) and considering their distances and small sizes, many of them are probably still unknown.

In this Thesis I present results on two minor bodies populations: Main Belt objects and Irregular Satellites, mainly focused in color analysis, which gives us information on the bodies surface properties. In Chapter 2 I show the detection of asteroids (mainly from the MB) in the High Cadence Transient Survey (HiTS), campaign 2014; those results are compared with those of other surveys, remarking the characteristics that such surveys need to have in order to be useful for asteroids' studies. This chapter shows the results already published in Peña et al. (2018). In Chapter 3 I present size and color analysis of asteroids detected in HiTS (campaign 2014 and 2015) showing how asteroid detection can vary when observed at high ecliptic latitudes and setting an upper limit to the observational cadence to obtain good colors of MB asteroids. This chapter shows the results already published in Peña et al. (2020) and, in contrast with Chapter 2, it shows a modified version of the asteroids' linking algorithm more useful for sparser data. In Chapter 4 I show measured colors of Saturn Irregular Satellites in contrast of colors of other Irrs and TNOs found in the literature. The results shown in this chapter have been already accepted by the Astronomical Journey and it is expected to to be published in the next months. In Chapter 5 there are main conclusions for all results shown in this thesis. Different techniques where designed to measure and detect the different bodies studied, such as a new algorithm to link asteroids detected in different nights to improve their orbital parameter determination (Chapter 2), an open access algorithm to rapidly compute precise and accurate minor bodies ephemerides (Appendix Annexed D) and a technique to measure magnitudes and colors of faint objects near bright sources (Chapter 4)

[8] `https://ssd.jpl.nasa.gov/tools/sbdb_query.html`
Consulted in April 5^{th}, 2022

Chapter 2

Asteroids in the High cadence Transient Survey

2.1 Surveys and Asteroids

We are entering the age of wide-field surveys, where massive amounts of data are collected to gather information on as many sources as possible while monitoring how the sky changes over time. In this new era, data can be refurbished to be useful for a science case different from the one it was originally designed for. This is particularly true for "time domain" astronomy, where multiple observations of a region are obtained in hopes of finding differences between data taken in different epochs. For example this has been used in the past to search for moving objects in the Hubble Space Telescope's archive (Fuentes et al., 2010, 2011), where most of the objects were discovered in data obtained for SNe characterization. Other surveys not mainly focused in Solar System science, such as SDSS (York et al., 2000), WISE (Wright et al., 2010) or PS-1 (Chambers et al., 2016) had also been used for detection and study of Solar System's Minor Planets (see Table 2.1 for more examples).

Supernovae (SNe), Solar System (SS) objects, or transiting Exoplanets all need multi-epoch observations to be discovered. The timescale over which the observations must be carried out depends, however, on the particular object of study. Hence, while SN surveys usually observe a field over a couple of weeks, SS objects can be detected in a single night and confirmed a few days later, and exoplanets may need weeks of dense monitoring to detect the ephemeral transit. A survey's success is determined in part by an appropriate choice of cadence, which also determines its value for surveying other phenomena. This was one of the main aspects when planning one of the largest survey to come: The Large Synoptic Survey Telescope (LSST) project (LSST Science Collaboration et al., 2009). The LSST will marry different communities by devoting its operation to imaging the sky efficiently and consistently. In order to do so, a great deal of effort has being spent in selecting the best observing strategy to fulfill the science needs of all the groups involved.

This chapter presents the search of Solar System objects in the High cadence Transient Survey (HiTS), a high cadence survey designed to find young Supernovae using the Dark

Table 2.1: Surveys with Minor Planets Detections

Survey	Ω deg^2	lim. mag.*	$N_{\rm obj}$	Strategy
SDSS I/II[a]	∼10,000	$r^* \sim 22$	471,569 asteroids[b]	∼ 8 years survey. Each field in 5 bands (72s between bands). 28% of surveyed area is covered twice or more.[c]
CFEPS[d]	∼320	$m_g \sim 24$	169 TNOs	∼4 years for discovery + follow-up 2 years later. Cadence optimized for TNOs (few observations spanned on days to months).
WISE[e]	All the sky	$W1$ ∼15.3[f]	∼150,000[g]	∼1.5 years survey. All the sky is observed in ∼7 months, visiting the same area at least 8 times (on ∼10 days).
(i)PTF[h]	∼10,000	R∼20.5	∼1582[i]	∼8 years survey. Cadences vary from minutes (new bodies) to days. Known asteroids are extracted before linking. Discoveries are made via linking and streak-detections (for NEOs)
PS-1[j]	∼30,000	$r_{P1} \sim 22$ $w_{P1} \sim 22.5$	600,000 asteroids[g]	∼ 4 years survey. Different observing methods. Most of the surveyed area is observed 4 times a year. There are also observations at the ecliptic plane for NEOs and KBOs.
HiTS[k]	120	g_{50}=23.5-24.5	7,700	∼5 days survey. Each surveyed area is visited 4-5 times per night every 2 hours.
LSST[l]	∼25,000	r ∼24.5	> 5 millions (estimated)	∼10 years survey. 2 pairs of visits per field separated by ∼30 mins. covering the entire visible sky every 3-4 days (∼ 4,000 deg^2 [m]).

Notes

* Most surveys quote the limiting magnitude (LM) for individual detections. The LM for asteroids requires a control sample. In HiTS 2014 survey the LM was estimated with known asteroids ($g_{50} \sim 23.5$) as shown in Figure 2.3a and 2.3b

[a] Ivezić et al. (2001)

[b] `http://faculty.washington.edu/ivezic/sdssmoc/sdssmoc.html` ; Ivezic et al. (2010)

[c] The Sloan Digital Sky Survey Project Book (`http://www.astro.princeton.edu/PBOOK/`)

[d] Petit et al. (2011); Kavelaars et al. (2009)

[e] Mainzer et al. (2011); Wright et al. (2010)

[f] `http://wise2.ipac.caltech.edu/docs/release/prelim/expsup/sec2_2.html`

[g] Vereš et al. (2017)

[h] Law et al. (2009); Kulkarni (2013); Waszczak et al. (2013, 2015, 2017)

[i] `https://www.ptf.caltech.edu/page/asteroids_data`

[j] Chambers et al. (2016); Lin et al. (2016)

[k] Förster et al. (2016)

[l] Jones et al. (2016)

[m] Assuming 2 visits of 30 seconds per 10 hr night.

Energy Camera (DECam) at the 4m Blanco Telescope on Cerro Tololo Observatory (Förster et al., 2016). DECam has been hailed as a precursor of LSST for its large field of view, fast readout, and large 520 Mpix CCD camera (DePoy et al., 2008).

This chapter focuses in HiTS 2014 data, which contains several observations of the same area of the sky during consecutive nights. The expected discovery efficiency is tested against the known population of asteroids, while extending the sensitivity to smaller objects by at least one magnitude. Is shown that high cadence Supernovae surveys (or similar) in general are well suited to search and characterize the orbits of SS objects.

The HiTS data is described in section 2.2. In section 2.3 is shown the linking algorithm used to find asteroids and other SS objects. The results and their comparisons with known objects is presented in section 2.4. The results are discussed in section 2.5 and general conclusions can be found in Chapter 5.

2.2 Looking for asteroids in HiTS 2014

2.2.1 HiTS observations

HiTS was a survey aimed to discover and follow up transients, especially the earliest hours of supernova explosions. For this, it combined high cadence with a high limiting magnitude and a wide field of view. These characteristics offer the opportunity to do science in various topics other than supernovae (Förster et al., 2016, 2018) such as RR Lyrae (Medina et al., 2017, 2018), SS minor bodies (Peña et al. 2018, 2020, shown in this Thesis) and automatic classification of variable sources (Martínez-Palomera et al., 2018).

HiTS observations were obtained with the Dark Energy Camera (DECam) mounted at the prime focus of the Blanco 4m telescope at the Cerro-Tololo International Observatory. DECam covers a 3 square degree field of view with a mosaic of $\sim$ 60 ccd of 2Kx4K pixels, yielding a $0.27''$/pixel resolution (DePoy et al., 2008).

HiTS was run in three different campaigns: the 2013, 2014 and 2015. The 2013 campaign observed 40 DECam fields (120 deg^2) every 2 hours (exposures of 173 s) during 4 nights in u band. In 2014 we observed 40 DECam fields (120 deg^2) every 2 hours (exposures of 160 s) during 5 nights in g band. The 2015 campaign consisted of 6 consecutive nights surveying 50 DECam fields (150 deg^2) with a cadence of 1.6 hours (exposures of 87 s) in g band (with some observations in r and i bands). The details of HiTS can be found in Förster et al. (2016), along with a comparative table of its three campaigns. Since HiTS was not designed for asteroid observations, all asteroids observations were serendipitous. In 2014 the observations reached the ecliptic, while 2015 observations are at least 5° away from the ecliptic. The ecliptic distribution of the observations in both campaigns is shown in Figure 2.1. In this chapter are analyzed only data from the 2014 campaign, which is the deepest of the three mentioned above.

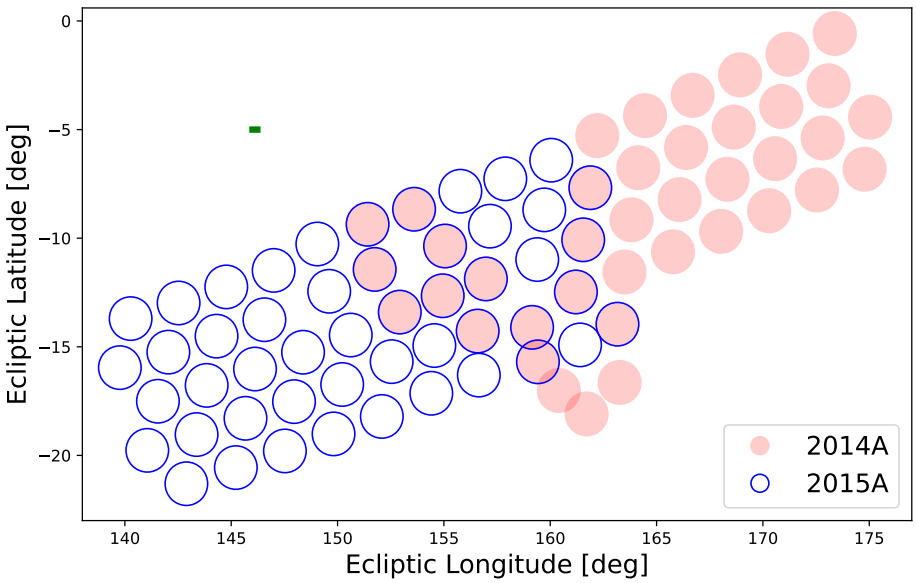

Figure 2.1: HiTS pointings for the 2014A and 2015A campaigns in geocentric ecliptic coordinates. The length of the thick green line is equal to one day's mean motion of the MB asteroids discovered in this chapter.

2.2.2 Data Processing

The HiTS survey runs a custom–made pipeline in real–time to detect fast transients. Given its cadence, with several observations per night, and the location of its fields, close to the Sun's opposition in 2014, it was ideally suited for the detection of asteroids as well, which are analyzed in this work.

The raw data was pre–processed with a local copy of the DECam Community Pipeline (DCP), which includes electronic bias calibrations, crosstalk corrections, saturation masking, bad pixel masking and interpolation, bias calibration, linearity correction, flat field gain calibration, fringe pattern subtraction, bleed trail and edge bleed masking, and interpolation (Förster et al., 2016).

Pre–processed data was template subtracted with the HiTS pipeline described in Förster et al. (2016) and Cabrera-Vives et al. (2017). Images are registered using a Lanczos 2 kernel and convolved using a variable pixel size kernel. After differencing, variable candidates are detected using the optimal photometry method (Naylor, 1998), and classified as real or bogus using a random forest classifier (RF), which retrieves a probability for each candidate of being real. The RF was previously trained using data from the 2013A campaign. The classification of sources requires the computation of the candidates' features, which absorbs most of the computational cost. Calculating the 56 features in a single 2.2 GHz processor takes ∼11 seconds for ∼5,000 candidates. Selecting only those candidates with probability higher than .5, the data is reduced by ∼80%, reducing the original 1.8 million candidates in HiTS to ∼360,000. The latter, delivered by the HiTS team, were the detections used in this work.

Since convolution forces the same calibration for the template and science images, this photometry is based on the absolute calibration of the template images. The photometric precision in the g band was estimated to be better than 0.02 mag. for objects brighter than

21 mag., deteriorating up to 0.2 mag. at 23 mag. (Martínez-Palomera et al., 2018).

2.2.3 Survey Efficiency

The known asteroid population from the Minor Planet Center [1] (MPC) was used as an unbiased sample to test the asteroid detection efficiency of the HiTS survey. By checking the number of times a known asteroid is detected as a variable source we get an accurate assessment of the maximum number of asteroids our linking algorithm can identify as a moving object.

The match between HiTS's detections and known asteroids for every epoch is shown in Figure 2.2a, showing their projected separation in the sky . Most asteroids ($\sim$95%) are identified with a detection lying within $\sim 7''$, while the position errors are larger along the ecliptic. Based on this plot a $7''$ tolerance in projected distance is considered to match detections between HiTS and MPC's positions of known asteroids. The typical sky density of our variable source list is $\sim 120\text{deg}^{-2}$, while the density of the MPC list of asteroids neighboring HiTS pointings is 40deg^{-2}. To calculate the probability P of getting one spurious match per square degree, we consider that the probability of a match is $p = \pi r^2/\Omega$, with $r = 7''$ and $\Omega = 1\text{deg}^2$. Then the probability of not matching a detection to any of the known bodies is $p_1 = (1-p)^{40}$ and the probability of not matching any HiTS detection to any of the known bodies is $P_0 = p_1^{120}$. Finally, we have that $P = 1 - P_0$, which brings the chances of getting one spurious match per square degree down to 6%. In consequence, this is the same probability of including one false detection on an otherwise fully correct track, per square degree (see section 2.3 for the definitions of *detection* and *track*). Because there can be several detections per square degree during the five days of this survey is not unusual to have trajectories that link real detections of asteroids with a few false detections. In this work this is called *track confusion*. Beside this, from simulations of one field (using the same characteristics of one of HiTS, but with randomly simulated detections) is found that the probability of linking an entire track with unrelated detections (a false track) is less than 2%[2], resulting in tracks that almost certainly would be rejected when doing the keplerian fit (see section 2.4.2).

There are $\sim 7,700$ different known asteroids near HiTS pointings. In Figure 2.2b is shown the number of times one of these known asteroids is matched with a detection in the HiTS variable source list (projected distance under $7''$). The sample is divided between those that are matched under three times (meaning that they can not be detected by the linking algorithm, in gray) and those that have enough detections to be linked (in blue). The detection efficiency does not improve significantly when using the entire 1.8 million candidates from HiTS (without the machine learning selection), losing 5% of the known asteroids' detections, which translates into a 2% drop in the number of known asteroids that we are able to recover and identify.

[1] Information provided via web page in `http://www.minorplanetcenter.net/cgi-bin/checkmp.cgi`

[2] Calculated comparing the number of tracks obtained from random detections versus the number of tracks obtained from HiTS detections, as shown in section 2.4

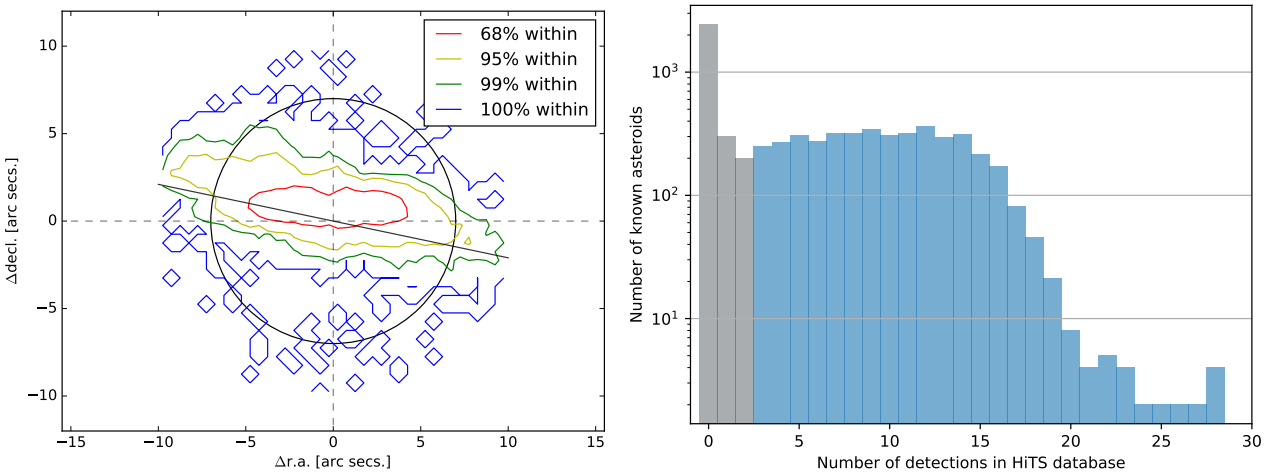

(a) **(b)**

Figure 2.2: *(a)* Contour plot for the difference between coordinates of MPC and HiTS data. Each contour surrounds a percentage of the matched data. Straight black line has the same slope as the ecliptic. Black circle has a 7″ radius. *(b)* Histogram of number of times an asteroid was imaged and analyzed as a variable candidate source by the HiTS survey. All known asteroids (from MPC) that were within 1.25 degrees of any DECam pointing in the HiTS survey during 2014 were considered in this analysis. Asteroids with less than three detections are shown in gray, those with three and more are colored blue.

2.3 Analysis

The data used for this work consists of catalogs of variable object candidates obtained via image subtraction as explained in section 2.2.2. The catalogs were filtered using a random forest classifier based on candidate image stamps (see Förster et al. 2016). Candidates with a probability larger than 0.5 of being real according to the classifier are called *detections* in this work. Detections are linked into trajectories using two different algorithms. The first one works as follows: we first linear segments of at least 5 detections are found by looking for clusters of relative velocities between detections. Then those linear segments are joined to form more complete curved trajectories. These trajectories are also processed to eliminate outliers or to add detections not found in the previous steps. Finally, trajectories with a high acceleration are removed and trajectories are forced to be disjoint sets. These trajectories are actually candidates for real trajectories, so they are just called *tracks*. The execution time of this algorithm scales as $\mathcal{O}(n^2)$. This means that without rejecting $\sim 80\%$ of the original data using Machine Learning, it would have taken 25 times longer to find our tracks. When comparing to the list of known asteroids this algorithm yields about a 30% efficiency. The second linking algorithm is similar to the one used in Trilling et al. (2017) and Valdes & DECam NEO Survey (2015), with an execution time that scales as $\mathcal{O}(n \log n)$. As this algorithm runs much faster than the first one, we considered three-detection tracks, improving the linking efficiency as shown in the next section. When considering tracks of at least 5 detection the efficiency is identical for both algorithms. Since there are at most 4 detections for the same object in a single night, requiring at least 5 detections leaves many

single-night tracks out. Looking for single-night tracks and then joining them yields better results (see Figure 2.3b).

2.4 Detected Asteroids

2.4.1 Magnitude Distribution

The second algorithm presented in the previous section yielded a total of 14,507 tracks. In Figure 2.3a we show all these tracks as a blue magnitude histogram, all known asteroids that are present in at least three detections in our data as an orange histogram, and all known asteroids that were also detected as tracks as a green histogram. To identify a track as a known asteroid is required that at least three detections in the track are closer than $7''$ to the same MPC object, which results in 3,812 tracks recognized as known asteroids. Thus, all objects in the green distribution are also in the blue and orange distributions of Figure 2.3a.

With this information is possible to calculate the efficiency per magnitude bin of the track finding algorithm, as the ratio between the number of recognized tracks and the number of known objects found with at least three detections in HiTS data. This efficiency is shown in Figure 2.3b, where the errors in efficiency are computed propagating Poisson errors. The total efficiency of the track finding algorithm, defined as the ratio between the total number of recognized tracks and the total number of known asteroids with at least three detections, was found to be 0.9. The total efficiency is shown with a red dotted line in Figure 2.3b. Although the sampled population (known objects) is in average brighter than HiTS detections, the apparent drop in detection efficiency in Figure 2.3b slightly beyond $g = 23$ is consistent with the drop in number of recognized tracks in blue (Figure 2.3a).

2.4.2 Orbital Fitting

A Keplerian orbit was fitted to each track using a modified version (better suited for asteroids) of the code by Bernstein & Khushalani (2000) to fit all the positions from each object into a sky trajectory. In order to reduce the number of spurious detections we fitted tracks which had 6 or more detections in total and with at least 2 detections in each night where they were found. All trajectories with unbound solutions or with maximum residuals at any detected time larger than 2 arc-seconds were also rejected.

This resulted in 7,700 bound trajectories[3] with a typical arc of 2.2 days, which are shown in Figure 2.4. Most of the asteroids found (6,687) belong to the Main Belt (in blue, perihelion $q > 1.3$ AU and semi-major axis $a < 4.2$ AU); there are 19 Near-Earth objects (NEOs, red, $q < 1.3$ AU); 14 Centaurs (in orange, $q > 5.2$ AU and $a < 30$ AU); and 15 TNOs (green, $a > 30$ AU). We use orbital parameter limits from the literature (Gladman et al., 2008; Parker et al., 2008; Jurić et al., 2002). Note that there are 708 unclassified objects (in gray) which are outside the regions of these other families. These are most likely Jupiter Trojans for which a ∼2–day arc is insufficient to constrain their orbital parameters precisely enough to be classified as such (note that the observed fields are near the L4 lagrangian point of Jupiter).

[3]Available in `http://www.das.uchile.cl/~jpena/HiTS_2014/`

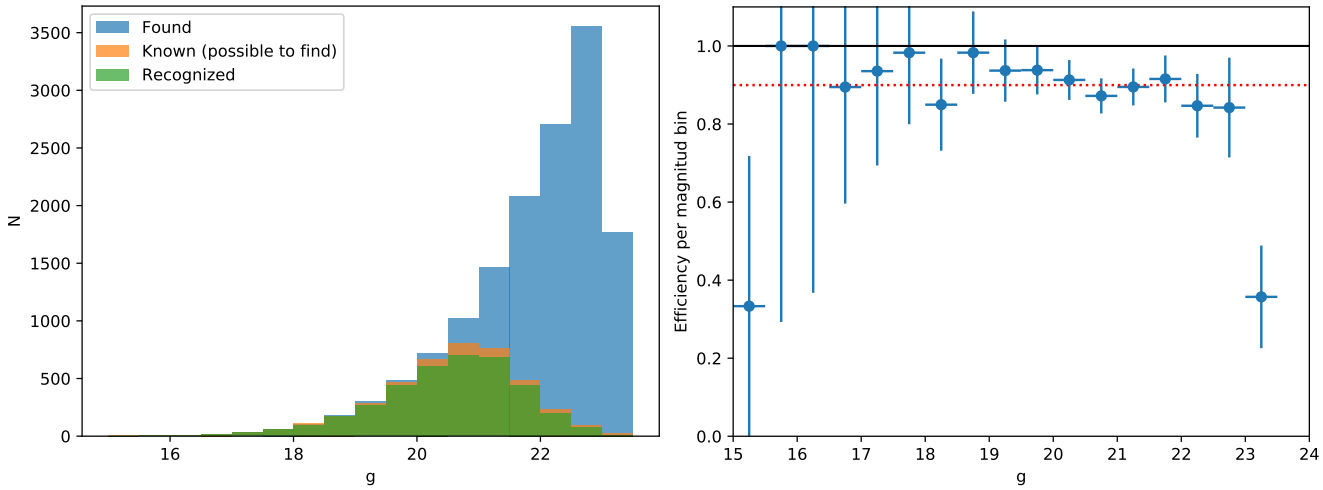

(a) **(b)**

Figure 2.3: *(a)* Histograms of number of asteroids per magnitude (g band). In orange, known asteroids (from MPC) that our linking process can find (have three matches with our data). In blue, tracks found in the HiTS data. In green, those tracks that were recognized as known objects. The drop in the blue histogram appears consistent with Figure 7 in Förster et al. (2016) once the effect of image subtraction is taken into account, which results in a loss of ∼0.4 mag. *(b)* Efficiency of recognized objects over the known objects per magnitude bin (see green and orange histograms in Figure 2.3a). Errors are propagated using Poisson errors for each measurement. The dotted red line represents the total efficiency (total number of recognized tracks over the total number of known objects), equal to 0.9.

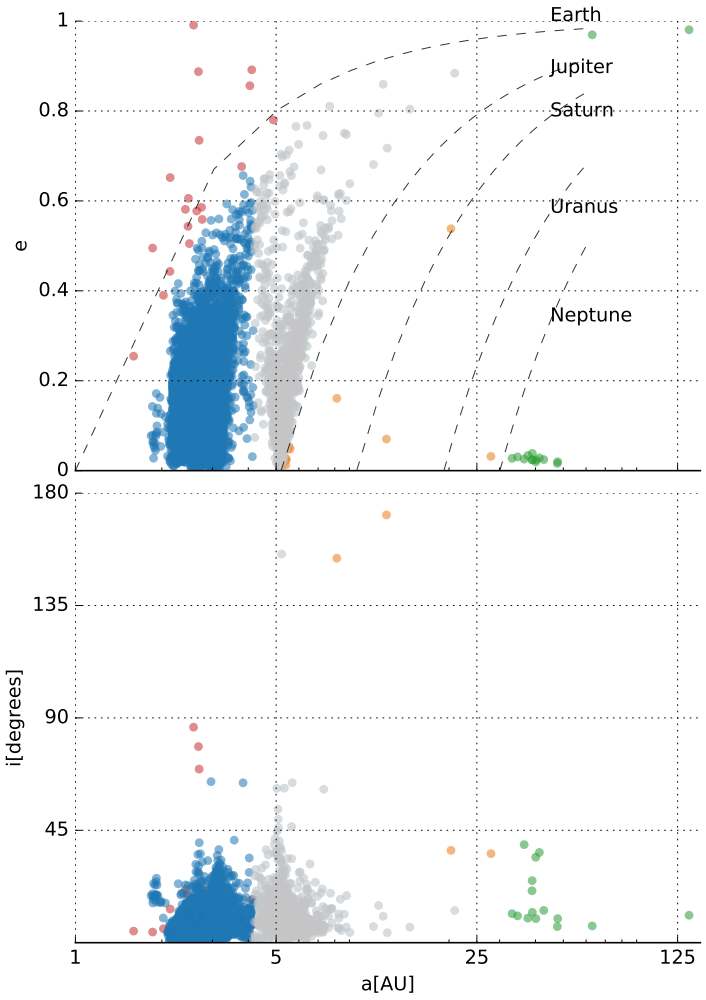

Figure 2.4: Orbital solution for all tracks that yield bound orbits and a maximum deviation of 2 arc-seconds from the model. There are 7,700 objects in 2014 that fulfill this criterion. The lines show the solutions that share their pericenter distance with the outer planets. Near Earth Objects are shown in red, Main Belt asteroids in blue, Centaurs in orange, trans-Neptunian objects in green and those that did not fit any of the other criteria in gray, most likely Jupiter Trojans for which the uncertainties on their orbits does not allow to tag them as such.

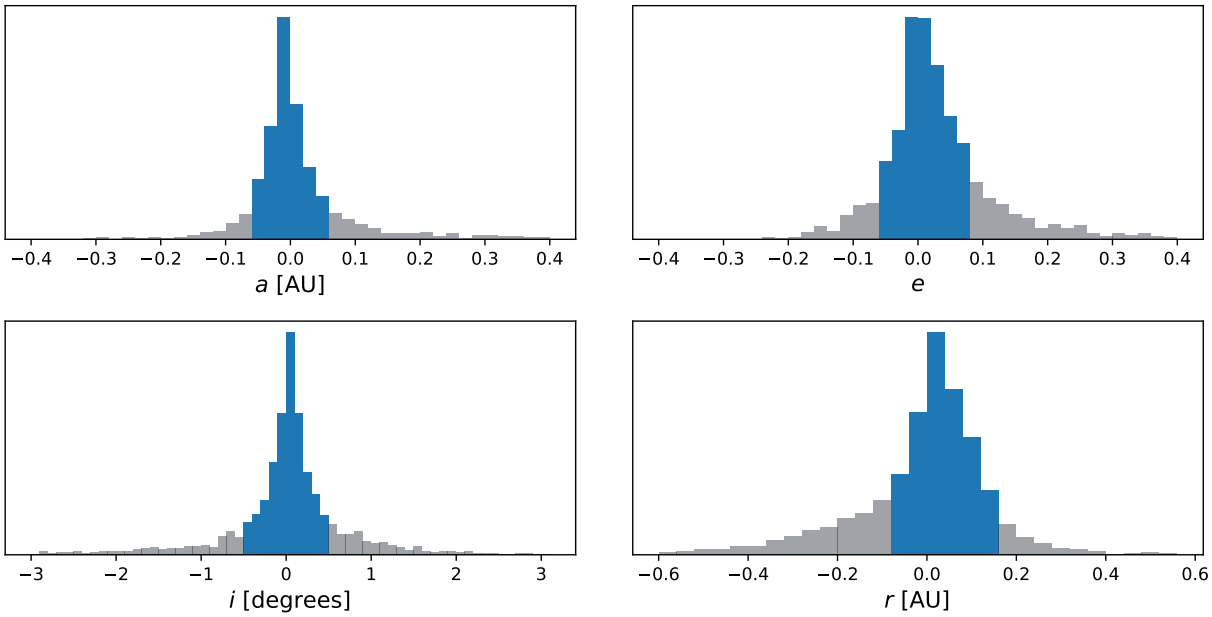

Figure 2.5: Errors for the estimated orbits of known asteroids. The $1-\sigma$ confidence region is highlighted. From left to right and top to bottom, the errors are shown for semi-major axis, eccentricity, inclination and heliocentric distante. The implied $1-\sigma$ confidence region for the orbital solutions are: $\sigma_a = [-0.08, 0.06]$ AU, $\sigma_{\rm e} = [-0.06, 0.08]$, $\sigma_{\rm i} = [-0.4, 0.6]$ degrees and $\sigma_r = [-0.08, 0.16]$ AU.

The uncertainty in the fitted orbital parameters is computed as the standard deviation of the errors between the orbital parameters derived from the Keplerian fit and those reported by the MPC (see Figure 2.5). This analysis does not consider objects observed only in a single night as their arc does not allow a reliable fit, leaving orbital parameters of 2,464 known asteroids to compare with. We report the $1-\sigma$ uncertainties as the interval that bounds 68% of the errors around the mode (as in the normal distribution) to be $\sigma_a \sim 0.07$ AU for the semi-major axis, $\sigma_{\rm e} \sim 0.07$ for the eccentricity, $\sigma_{\rm i} \sim 0.5$ deg for the inclination and $\sigma_r \sim 0.11$ AU for the heliocentric distance.

Most of the computed orbital parameters show errors that follow a normal distribution around the known value (See Figure 2.5). However, there is a tail of fitted orbits that fall far outside the range of that figure. These orbits correspond mostly to those consistent with Trojan orbits (in gray in Figure 2.4). The fraction of those poor orbit fits are 7%, 1% and 1% for a, e and i respectively.

2.4.3 Synthetic Color

Using HiTS g magnitudes with the V magnitudes provided by MPC, I calculated the colors of those objects considered in Figure 2.5 that could be fit into a Keplerian orbit and are consistent with Main Belt asteroids, as shown in Figure 2.6. Asteroids at the Inner Belt are redder than those in the Outer Belt, as seen in Figure 4 of Parker et al. (2008). This exercise shows how adding observations with another filter could allow us to extend the color-family relationships in the Main Belt (as seen in Parker et al. 2008) to much smaller objects.

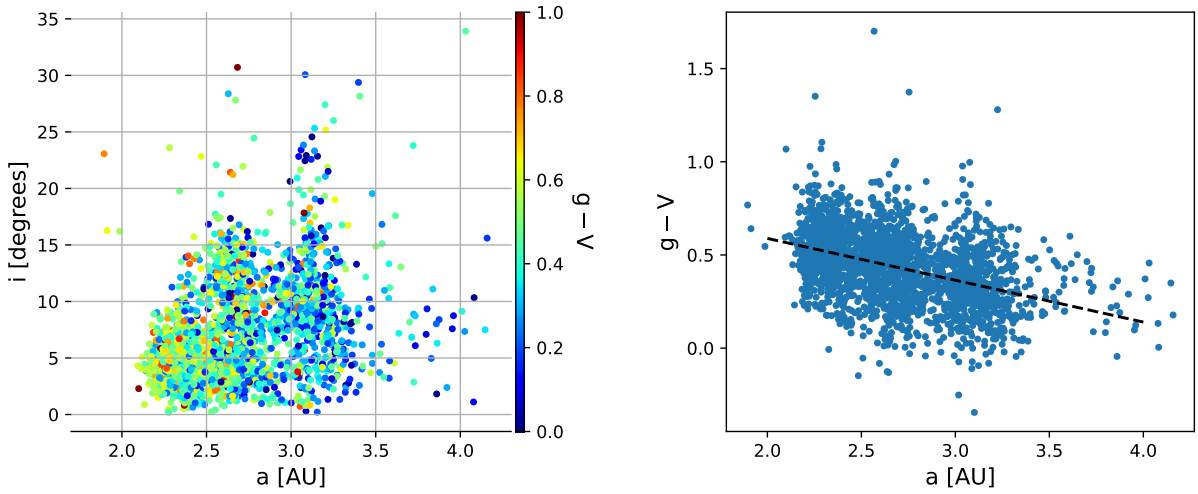

Figure 2.6: Left: Known Main Belt asteroids rediscovered in HiTS 2014 survey with arcs longer than one day are shown in this $g-V$ color vs. orbital parameters a and i, as inferred from our photometry and orbital fit. Right: $g-V$ color vs. semi-major axis (from our orbital fit), with the black line shows a linear fit between both parameters, showing how colors get bluer with semi-major axis.

2.5 Summary and Discussion

In this chapter is shown the search for asteroids and other Solar System populations imaged in the High cadence Transient Survey (HiTS), campaign 2014. This wide-field survey covered $\sim$ 120 square degrees over 6 nights looking for time variable phenomena, in particular Supernovae. This search took advantage of the readily available HiTS's pipeline's variable source catalog (Förster et al., 2016), already classified by machine learning, and performed two different linking algorithms for motion consistent with known small-body populations. 7,700 viable orbits were found, identifying 19 NEOs, 6,687 Main Belt asteroids (around 2,500 previously known), 14 Centaurs, and 15 TNOs as shown in Figure 2.4. It is important to notice that this characterization is based on relatively short arcs (mean arc $\sim$ 2.2 days). The computed orbits are precise enough to determine orbital parameters with precision for the longest arcs, but not enough to classify all reported objects (see Figure 2.5). I used the list of known objects from the MPC to check on the efficiency and orbital accuracy. Of those known orbits in these tracks (3,812), only those with arcs longer than one night (2,464) yielded bound orbits. There were 708 objects (gray dots in Figure 2.4) with orbits mostly consistent with Jupiter Trojans but with large orbital uncertainties.

These results serve as a good model for the asteroid discovery efficiency that can be expected from synoptic surveys like LSST, with one cadence optimized for several different science drivers (LSST Science Collaboration et al., 2009; Jones et al., 2016). Table 2.1 shows a comparison of this work with other past and future Solar System searches on wide-field surveys. It includes the total surveyed area, limiting magnitude, number of discoveries, and time span for data gathering as a basis of comparison. Cadences vary greatly between surveys and usually within the same survey. LSST's basic survey strategy of observing one field twice a night, covering the entire sky every 3-4 days is similar to HiTS' constant cadence returning to each field over 5 nights. This match between observing cadences yields a similar linking

problem, that requires finding tracklets within a few days to form a proper Solar System trajectory.

These results were enabled by the overwhelming rejection of spurious detections by the machine learning algorithm described in Cabrera-Vives et al. (2017) and Förster et al. (2016). This filtering process on raw detections not only reduces the execution time, but also reduces false discoveries and the number of trajectories contaminated with incorrect detections (which scales with the number density of detections). This "track confusion" increases the errors in orbital parameters and is an important problem when trying to extend one track into another night. LSST is expected to produce $\sim$10 million alerts per night (LSST Science Collaboration et al., 2009). It would take $\sim$6 hours in a single 2.2 GHz processor to compute Machine Learning features for all of these. This problem is readily parallelizable to substantially reduce the extra processing time.

Although this classification algorithm (Cabrera-Vives et al., 2017; Förster et al., 2016) is not tailored for tracked moving objects, only 5% of detections and 2% of real traceable objects were rejected. Future work is needed in describing sources that deviate from a point source to better account for this obvious source of confusion, as well as other special cases like binaries, comets, etc. Having a well-defined probability for each detection in the source list of any future survey will improve the accuracy of any linking algorithm, especially when dealing with track confusion. We can use the surveyed area to scale the computational cost of our search if applied to LSST assuming they use a vetting algorithm that rejects 80% of the alerts. The simple $\mathcal{O}(n^2)$ search algorithm with no major optimization would be able to link the area surveyed in one night to data obtained 3-4 nights before in 36 hrs (using 120 nodes of 20 2.2 GHz cores each). However the $\mathcal{O}(n \log n)$ algorithm would only take 2 hours in a single node of 20 cores. This vetting of detections would enable users to run their own linking algorithms to search for moving targets in the LSST's alert stream (the analogue of our transient candidates catalogue). Improving and optimizing the classification of raw non-vetted detections yields great benefits for the implementation of search algorithms in general. This work shows that using a similar ML classification scheme, LSST (or its brokers, such as ALeRCE, Förster et al. 2021) could provide better alerts with little extra overhead and that simple algorithms can then link moving objects with an arc of 3-4 days within hours. This arc is long enough to constrain the orbital parameters to a few percent for asteroids observed near opposition. Adding ML to the reduction process means that a fast-moving object could be discovered and followed up on the same night.

Chapter 3

Asteroids' Size Distribution and Colors from HiTS

3.1 Finding the Size Distribution of the Main Belt: Not a single answer

As discussed in Chapter 1, while planets grew and migrated in our SS past, thousands of planetesimals formed, grew bigger and broke into smaller pieces in a process that can still be studied in the stable reservoirs of minor bodies (MB, Jovian Trojans, Neptunian Trojans, and TNOs). This evolution has left its mark in the orbital distribution of the MB and in its size distribution (SD).

The SD provides a direct glimpse into the collisional history of minor bodies. Under collisional equilibrium the SD is described by a power law of the form $N(H) \propto 10^{\alpha H}$ and $N(D) \propto D^{-q}$ (H the absolute magnitude and D the body's diameter, with $q = 5\alpha + 1$) with $q = 3.5$ and $\alpha = 0.5$ (Dohnanyi, 1969). In Table 3.1 is provided a summary of SDs measured from different MB surveys, including sub-population and filter information. Having multiple filters provides asteroids' surface colors that might be related to composition and collisional history.

Ivezić et al. (2001) analyzed the Sloan Digital Sky Survey (SDSS) data (York et al., 2000) and separated the MB by color, finding $\alpha \sim 0.61 \pm 0.01$ for brighter bodies while they found $\alpha = 0.24 \pm 0.01$ for *"red"* bodies, $\alpha = 0.28 \pm 0.01$ for *"blue"* bodies and 0.25 ± 0.01 for *"blue"* and *"red"* combined (*"red"* and *"blue"* by their definition, associated to S-type and C-type respectively). For S-type and C-type asteroids, they found that both of their SDs have a break at $D \sim 5$ km, and attributed this feature to a color-size dependence for bodies smaller than 5 km. Parker et al. (2008), using a more updated data set (an early version of the 4th release of the SDSS Moving Object Catalog, Ivezic et al. 2010) divided the MB by semi-major axis a and analyzed the absolute magnitude H, finding similar slopes for bright bodies but steeper slopes for smaller objects ($\alpha \sim 0.42$). In both cases they found the SD gets flatter with a. Parker et al. (2008) also analyzed individual asteroid families, finding slopes α varying from 0.37 to 1.04 at the bright end and α from 0.1 to 0.62 at the faint end. Yoshida

et al. (2003) analyzed the size distribution for ~ 1000 small asteroids from SMBAS (Subaru Main Belt Asteroid Survey). Observations were only separated by $\sim$2 hours, affording only rough distance estimates. They report no break with a single power slope $q = 2.19 \pm 0.02$ ($\alpha = 0.24$) for the entire MB SD (for $D > 0.5$ km) which is similar to the one found by Ivezić et al. (2001) in SDSS. They also found that the SD gets flatter with a.

Yoshida & Nakamura (2007) using a new set of data from SMBAS measured $B - R$ and H, getting broken power laws for small bodies: $q = 2.29 \pm 0.02$ ($\alpha = 0.26$, similar to faint bodies from Ivezić et al. 2001) for small objects ($D < 1$ km) and $q = 2.75 \pm 0.02$ ($\alpha = 0.35$) for bright objects (between the values from Ivezić et al. 2001 and Parker et al. 2008); they also separated the bodies by color (based on a slight low density in their color histograms), finding that S-like (redder) bodies have $q = 2.29 \pm 0.02$ ($\alpha = 0.26$) at the faint end ($D < 1$ km) and $q = 3.44 \pm 0.09$ ($\alpha = 0.49$) at the bright end, while C-like (bluer) bodies could be characterized by a single slope of $q = 2.33 \pm 0.03$ ($\alpha = 0.27$). Lin et al. (2015) analyzed 150 asteroids finding an SD compatible with the slopes found by Yoshida & Nakamura (2007); they also found that S-like bodies are more common in the inner region of the MB while C-like bodies dominate the region beyond 2.82 au of the MB. Wiegert et al. (2007) analyzed 1525 MB bodies with an arc of $\leqslant 2$ days measured in g or in r with the Canada-France-Hawaii Telescope (CFHT); they found a very clear difference of slopes between g and r and a varying slope with distance, getting a steeper slope between $2.6 < a < 3.0$ au (parameter obtained assuming circular orbits); these results were discarded by August & Wiegert (2013) because they used data beyond the limiting magnitude. August & Wiegert (2013) used $\sim 17,000$ MB bodies from CFHT Legacy Survey (CFHTLS) with measurements in g and r, getting $\alpha = 0.39 \pm 0.01$ in g and r for all bodies without finding a color-size dependence, but they do recover a flatter slope at higher distance (all of this between $15 < H < 17$). August & Wiegert (2013) suggest this slope-distance dependence is produced by a difference in composition, in that the inner MB is dominated by S–type bodies and the outer MB by C–type, although they do mention that it is not clear how this differentiation affects the slope and they do not do a color analysis such as that of Ivezić et al. (2001) and Yoshida & Nakamura (2007). One year earlier, Gladman et al. (2009) analyzed ~ 1000 small bodies with time ranges of more than three nights (in the Sub-kilometer asteroid diameter survey, SKADS), allowing a good calculation of H, finding $\alpha = 0.38$ (in between the ones found by Ivezić et al. 2001 and Parker et al. 2008, but very similar to the one by August & Wiegert 2013). SKADS also has color measurements, but Gladman et al. (2009) did not find any bimodality as in SDSS (Ivezić et al., 2001) or as claimed in Yoshida & Nakamura (2007). Masiero et al. (2011) computed asteroid diameters from *Wide-field Infrared Survey Explorer* (WISE) data (Wright et al., 2010) and found that the SD follows a slope similar to the one find by Gladman et al. (2008) for small bodies. Ryan et al. (2015) analyzed $\lesssim 2000$ asteroids from *Spitzer*'s MIPSGAL and Taurus surveys (Carey et al., 2009; Rebull et al., 2010), obtaining $q = 3.34 \pm 0.05$ ($\alpha = 0.47 \pm 0.01$) for MB bodies between 2 and 25 km (which seems an in-between value from bright and faint slopes from previous surveys such as SDSS), and different slope values when separating by taxonomic type, although it seems they do not take into consideration their completeness limit (of 6.65 km or 15.75 in H according to them). In summary, there is a wide range of values for the α parameter, especially for faint bodies ($D \lesssim 5$ km). This is probably caused by differences in data reduction, orbital parameter determination and limiting magnitudes of each work. The most complete data set comes from SDSS (which uses known bodies for their orbital parameters), getting $\alpha \sim 0.61$

for bright bodies. For faint bodies, the values vary from 0.25 (Ivezić et al., 2001) to 0.38 by Gladman et al. (2009) (which is the largest survey published with good orbital parameter estimations) to ~ 0.42 by Parker et al. (2008) (again in SDSS). Many of these surveys have found that the SDs get flatter with a, while only some of these studies have found a slight color-size dependence.

In this chapter are shown the results finding asteroids in the 2015 campaign of the High cadence Transient Survey (HiTS). A fraction of our data ($\sim$1,700) have measured arcs of $\sim$24 hours, allowing acceptable orbital solution for H analysis. There are $g - r$ for $\sim$1,200 of them, allowing some color analysis. In section 3.2 is presented the HiTS data used. In section 3.3 is explained the detection linking algorithm used to get the different asteroids. In section 3.4 are shown the results: orbital parameters distribution, apparent and absolute magnitude distribution and color analysis (mainly for Main Belt objects). In section 3.5 are discussed the findings for the 2015 campaign putting them in contrast with results from 2014 campaign. General conclusions can be found in Chapter 5.

3.2 Data

This chapter focuses in data from the 2015 campaign of HiTS (see section 2.2.1 for a description of the survey) and expands the results from Chapter 2. The data from 2015 campaign is not as deep as 2014's but covers a wider area and increase the number of visits per night from 5 to 6. These 6 nights were followed by three nonconsecutive half nights 2, 5 and 20 nights after the end of the main run. Some of the DECam pointings during the 2015 campaign were observed in r and i bands, but not more than once per night (and only in a few nights).

3.2.1 Data Processing

The data used for this work were processed and reduced in the same way as done for the 2014 campaign (Förster et al. 2016; Cabrera-Vives et al. 2017, as seen in Chapter 2), meaning that we had astrometry and photometry of moving objects and a probability for each of them of being real or bogus obtained using deep learning.

An incongruity in the way reduced data from a few epochs for the 2015 campaign were stored produced some uncertainty in the actual observation time for detections in those epochs. To remedy this issue a new reduction was used (using another pipeline, see section 3 of Martínez-Palomera et al. 2018) that had the correct observation times but without their probability of being real or bogus. The old data was taken (with possible inconsistencies in their observation time) and their positions matched with detections of the new reduction; so if more than fifty percent of detections were within 2 pixels from the old data set to the new one for a given exposure, then the data from that exposure is considered to have the correct observation time stored and it keeps using the old detections, allowing to use their probability of being real. After this *quality control*, I decided not to use data from 4 entire fields and 13 exposures from different fields that showed too large distances between detections from the new and old databases or have not enough detections to compare. Two of those rejected fields were among the closest to the ecliptic. Finally I ended up with 154,444 detections of moving objects with a probability of being real higher than 0.5. This is less than half of detections from the 2014 campaign. Although for 2015 we had data of 7 more fields than

Table 3.1: Summary of SD slopes from different surveys

Survey	Date[a]	m_{lim}	Population	Criterion	N[b]	α[c]	Size Range
SDSS[d]	2001	$r* < 21.5$	MB	$1.5 \lesssim a \lesssim 4$ au	670,000	$0.61 \pm .01$	$D > 5$ km ($H \lesssim 15.7$)
						$0.25 \pm .01$	$D < 5$ km ($H \gtrsim 15.7$)
			"blue"	$a^* < 0$	467,000	$0.61 \pm .01$	$D > 5$ km
						$0.28 \pm .01$	$D < 5$ km
			"red"	$a^* > 0$	203,000	$0.61 \pm .01$	$D > 5$ km
						$0.24 \pm .01$	$D < 5$ km
SMBS[e]	2003	$R < 24.4$	MB	2<a<3.5 au	~ 500	$0.238 \pm .004$	$.5 < D < 1$ km ($18.3 < H_R < 19.8$)
			inner MB	2<a<2.6 au	~ 200[f]	$0.274 \pm .006$	$.23 < D < 1$ km ($18.3 < H_R < 21.4$)
			middle MB	2.6<a<3.0 au	~ 250[f]	$0.230 \pm .006$	$.34 < D < 1$ km ($18.3 < H_R < 20.6$)
			outer MB	$3.0 < a < 3.5$ au	~ 50[f]	$0.196 \pm .006$	$.49 < D < 1$ km ($18.3 < H_R < 19.8$)
SMBS[g]	2007	$R < 25$	MB	2<a<3.5 au	~ 800	$0.258 \pm .004$	$D < 1$ km ($17.8 < H < 20.2$)
					~ 200	$0.350 \pm .004$	$D > 1$ km ($14.6 < H < 17.4$)
			S–like	$B - R > 1.1$	–	$0.058 \pm .004$	$0.3 < D < 1$ km ($17.4 < H < 20.2$)
					–	$0.488 \pm .018$	$D > 1$ km ($15.4 < H < 17.0$)
			C–like	$B - R < 1.1$	–	$0.266 \pm .006$	$D > 0.6$ km ($14.6 < H < 20.2$)
CFHTLS[h]	2007	$g < 22.5$	MB	2.0<a<3.5 au	185	0.37 ± 0.01	0.6<D<10 km
			inner MB	2.0<a<2.6 au	77	0.316 ± 0.012	0.6<D<4 km
			middle MB	2.6<a<3.0 au	79	0.370 ± 0.012	0.8<D<6.3 km
			outer MB	3.0<a<3.5 au	29	0.320 ± 0.014	1<D<6.3 km
		$r < 21.75$	MB	2.0<a<3.5 au	423	0.488 ± 0.014	1<D<10 km
			inner MB	2.0<a<2.6 au	238	0.40 ± 0.01	1<D<7.9 km
			middle MB	2.6<a<3.0 au	143	0.478 ± 0.014	1.3<D<7.9 km
			outer MB	3.0<a<3.5 au	42	0.45 ± 0.016	1.6<D<6.3 km
SDSS[i]	2008	$r < 21.5$	inner MB	2.0<a<2.5 au	30,702	0.76	H<14 (D>7 km)*
						0.46	H>14
			middle MB	2.5<a<2.82 au	32,500	0.73	H<13.5 (D>9 km)*
						0.42	H>13.5
			outer MB	2.82<a<3.6 au	24,367	0.56	H<13.5
						0.4	H>13.5
SKADS[j]	2009	$R < 23.5$	MB	2.0<a<4.0 au	~ 1000	0.38	$14.8 < H_R < 17.4$ (1<D<5km)**
CFHTLS[k]	2013	$g \lesssim 23$	MB	2.0<a<4.0 au	7285	0.39 ± 0.01	$15 < H_g < 17.6$ (1<D<5km)
			inner MB	2.0<a<3.0 au	–	0.39 ± 0.02	$15 < H_g < 17.6$
			outer MB	3.0<a<4.0 au	–	0.35 ± 0.01	$15 < H_g < 17.6$
		$r < 22.5$	MB	2.0<a<4.0 au	9671	0.39 ± 0.01	$15 < H_g < 17.1$
			inner MB	2.0<a<3.0 au	–	0.39 ± 0.01	$15 < H_g < 17.1$
			outer MB	3.0<a<4.0 au	–	0.365 ± 0.004	$15 < H_g < 17.1$
Spitzer's[l]	2015	–	MB	2.06<a<3.65 au	1865	0.47 ± 0.01	2<D<25km
			C-Type	$p_V < 0.08$	~ 600	0.52 ± 0.01	5<D<25 km
			S-Type	$0.15 < p_V < 0.35$	~ 400	0.38 ± 0.02	5<D<25 km
HiTS 2014	this work	$g < 22.5$	MB	$1.3 < a < 4.2$ au	1,729	$0.68^{+0.17}_{-0.09}$	$11 < H_g < 14$ ($10 \lesssim D \lesssim 30$km)
						$0.34^{+0.04}_{-0.11}$	$14 < H_g < 17$ ($1 \lesssim D \lesssim 10$km)
HiTS 2015	this work	$g < 22$	MB	$1.3 < a < 4.2$ au	129	$0.88^{+0.09}_{-0.08}$	$14 < H_g < 16.5$ ($1 \lesssim D \lesssim 10$km)

Notes

[a] Publication date of the study.

[b] Number of bodies used in the analysis.

[c] Slope of the SD using H

[d] Ivezić et al. (2001)

[e] Yoshida et al. (2003)

[f] From Figure 11 in Yoshida et al. (2003)

[g] Yoshida & Nakamura (2007)

[h] Wiegert et al. (2007)

[i] Parker et al. (2008)

[j] Gladman et al. (2009)

[k] August & Wiegert (2013)

[l] Ryan et al. (2015)

[*] D calculated using albedo $p_V = 0.1$

[**] D calculated using albedo $p_V = 0.1$ and an average color of $V - R \simeq 0.4$ (see Figure 15 in Gladman et al. (2009)).

in 2014, the fewer data can be explained by the limiting magnitude of 0.5 to 1 magnitudes brighter (because of the smaller exposure time and bad weather) and because in 2015 the observations were at least ~ 6 degrees away from the ecliptic while 2014 data reached it.

3.2.2 Survey Efficiency

The asteroid detection efficiency of the HiTS 2015 survey was tested, as for the 2014 data, with the estimated position of known asteroids. An accurate assessment of the maximum number of asteroids that the linking algorithm can identify as a moving object is obtained by checking the number of times a known asteroid is detected as a variable source.

But first is necessary to define how far a detection can be from the estimated position of a known body to consider it as *"recognized."* At first, information from the Minor Planet Center[1] (MPC) was used to look for bodies within 1.25 degrees of any DECam pointing in HiTS 2015 (as in Chapter 2), but the necessity of having updated coordinates of these bodies led to use the Jet Propulsion Laboratory (JPL) web service[2] (which gives computational simplicity for big queries) to get the coordinates of those same asteroids. Using the coordinates of known bodies obtained this way allowed to compute the distance between JPL and HiTS detections, yielding the distribution shown in Figure 3.1a. Is remarkable that using data from JPL the difference was concentrated to a much smaller range, allowing to reduce the criteria for recognizing detections to a $4''$ distance (in comparison to the $7''$ in Chapter 2).

Using the recognized detections, we could see how many of the known bodies we found. In Figure 3.1b we show the number of asteroids as a function of the number of detections. In gray we show those that are found only in one or two detections and in blue those found three or more times. Since our linking algorithm required at least three detections per night (Section 3.3), we show in orange the subset of asteroids satisfying that condition.

3.3 Analysis

Since the detections with a probability of being real higher than 0.5 were more sparse than those in the 2014 campaign, linking detections for one night to another proved to be harder than in Chapter 2. To solve this, we first found *tracklets* (sets of at least three detections that assimilate a linear trajectory in *one* night) using the same linking algorithm used in Chapter 2 (at the end of section 2.3) but applied to each night separately. Three different algorithms were tested to link different tracklets between nights to finally obtain a collections of *tracks* (composed by 1 or more linked tracklets).

The first tested algorithm takes pairs of tracklets. If their estimated position in three different times (conveniently chosen for each pair to fall in the middle of them and near each tracklet) fell near each other, then those tracklets were joined. The positions were estimated using quadratic fitting of the tracklets. How far apart the estimated positions could be depended on how far they were from the tracklets (until a maximum distance of $\sim 20''$). This algorithm failed to link several known asteroids (such as the ones shown in Figure 3.2).

[1]Information provided via web page at `https://www.minorplanetcenter.net/cgi-bin/checkmp.cgi`
[2]JPL Horizons: `https://ssd.jpl.nasa.gov/horizons.cgi`

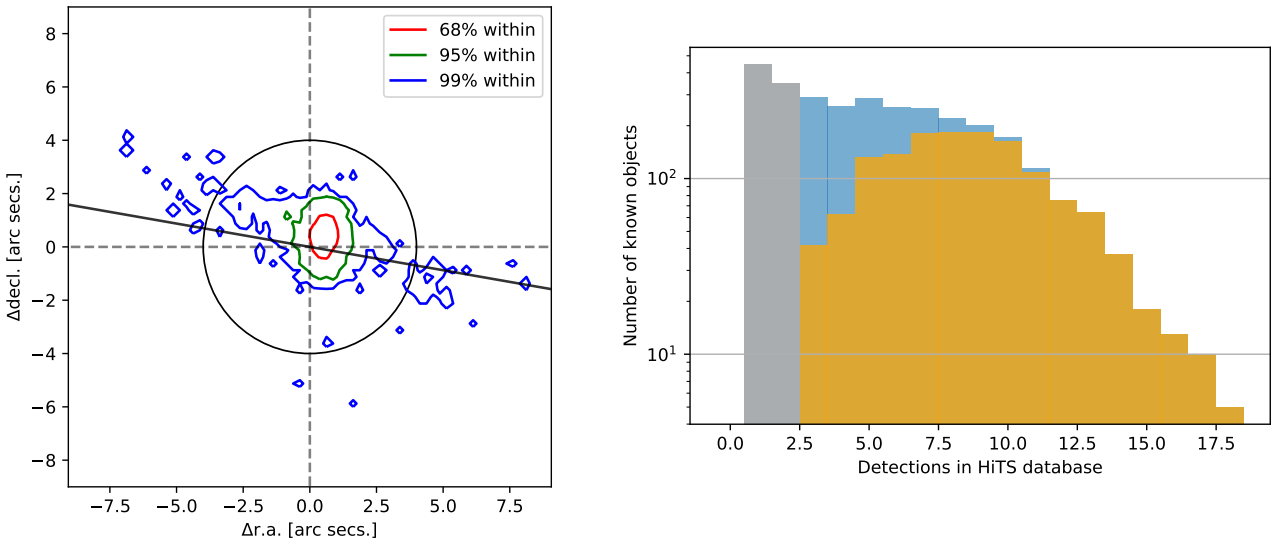

(a) **(b)**

Figure 3.1: *(a)* Contour plot for the difference between coordinates of JPL and HiTS data. Each contour surrounds a percentage of the matched data. The straight black line has the same slope as the ecliptic. The black circle has a 4″ radius. *(b)* Histogram of number of times a known asteroid was imaged and analyzed as a variable candidate source by the HiTS survey. All known asteroids (from MPC) that were within 1.25 degrees of any DECam pointing in the HiTS survey during 2015 were considered in this analysis (using coordinates delivered by JPL). Asteroids with fewer than three detections are shown in gray, those with three or more are colored blue and those with at least three detections in a single night are shown in orange.

Since tracks need to be in at least 2 nights to yield good orbital parameter estimation (see section 3.4.1) we realized we needed a better algorithm.

The second tested algorithm was HelioLink (Holman et al., 2018), which takes the method shown in Bernstein & Khushalani (2000) but moves the coordinates origin to the barycenter (or to the Sun) and assumes a distance and a velocity of the asteroid with respect to this origin. But the high density of tracklets in the (θ_x, θ_y) space (equation 1 in Holman et al. 2018) together with the clustering parameter (equation 11 in Holman et al. 2018) that encloses two distances in a single parameter caused many clusters to mix tracklets that did not belong together.

The third algorithm (and the one finally used in this chapter) uses a similar approach to that of HelioLink: assuming the same barycentric distance for all tracklets, clusters were made if the estimated barycentric ecliptic position coincided in two different times (the detailed algorithm is shown in Appendix Annexed A and Annexed B). Moving the coordinate reference to the solar system barycenter allowed to cluster tracklets estimating their positions using linear fitting, as seen in Figure 3.2, where curved trajectories as seen from Earth (left panels) are seen as straight lines (right panels). To cluster as many tracklets as possible it

was necessary to try different barycentric distances, although most of them were obtained assuming a distance of 2.5 au (roughly the middle of the Main Belt). This method found 1770 asteroids detected in more than 1 night (which highly increased the orbital parameters accuracy, see section 3.4.1) while first method only found $\lesssim$1100.

To prove that the clustering works properly, the total amount of clustered tracklets was compared with the amount of tracklets that could be obtained from the known asteroids. In Figure 3.3 there is the number of tracklets per cluster (upper panel) and the time arc per cluster (lower panel) for all found clusters, for all known clusters (tracklets identified as known bodies) and for known clusters as they were actually found by our algorithm (the *recognized* ones), in percentage in each case. Although $\sim 70\%$ of tracklets were not linked with any other (clusters of 1 tracklet), the same happened with the known clusters. This, together with the fact that almost all known clusters were linked without contamination (without wrongly joined tracklets), shows that this linking algorithm worked very well for this data.

3.4 Results

A total of 5740 tracks were produced after the clustering process. The efficiency of this process was checked with the 1422 known objects (Figure 3.1a) that our process could have linked (at least three recognized detections in one night, orange in Figure 3.1b). 1323 objects were found distributed in 1349 tracks. This means that the linking algorithm failed to join a minority of related tracklets, yielding a 93% detection efficiency.

3.4.1 Orbital Fitting

As in Chapter 2, a Keplerian orbit fit was applied to each track. Due to the degeneracy in distance and velocity for tracks that span only a few hours, only those that include observations in more than one night were considered. Then were rejected all trajectories that yield unbound solutions or that deflect more than $2''$ from an observation, leaving 1762 bound trajectories (or *good tracks* from now on). 1738 Main Belt asteroids were found, along with 6 Near Earth Objects (NEOs) and 4 TNOs, classified in the same way as in Chapter 2 (See Figure 3.4).

The orbital parameter uncertainties was estimated using the detection of the 397 known objects with *good tracks* recognized in our sample (see Figure 3.5). The $1-\sigma$ uncertainties (the interval that bounds 68% of the errors around the mode, as in the normal distribution) is reported to be $\sigma_a \sim 0.05$ au for the semi-major axis, $\sigma_{\rm e} \sim 0.06$ for the eccentricity, $\sigma_{\rm i} \sim 0.5$ deg for the inclination, $\sigma_{\rm r} \sim 0.12$ au for the body-barycenter distance and $\sigma_\Delta \sim 0.12$ au for the body-observer distance.

Figure 3.6a shows the distribution of the 1738 bodies identified as Main Belt objects divided in three groups: Inner Belt (from 1.3 to 2.5 au); Middle Belt (from 2.5 to 2.82 au) and Outer Belt (from 2.82 to 4.2 au). The limits between each group are in the most notorious Kirkwood gaps in Figure 3.6a and have been used to differentiate the MB in different works (such as Parker et al. 2008; Masiero et al. 2011 and DeMeo & Carry 2013, 2014). Each of these populations have 181, 566 and 991 found bodies respectively.

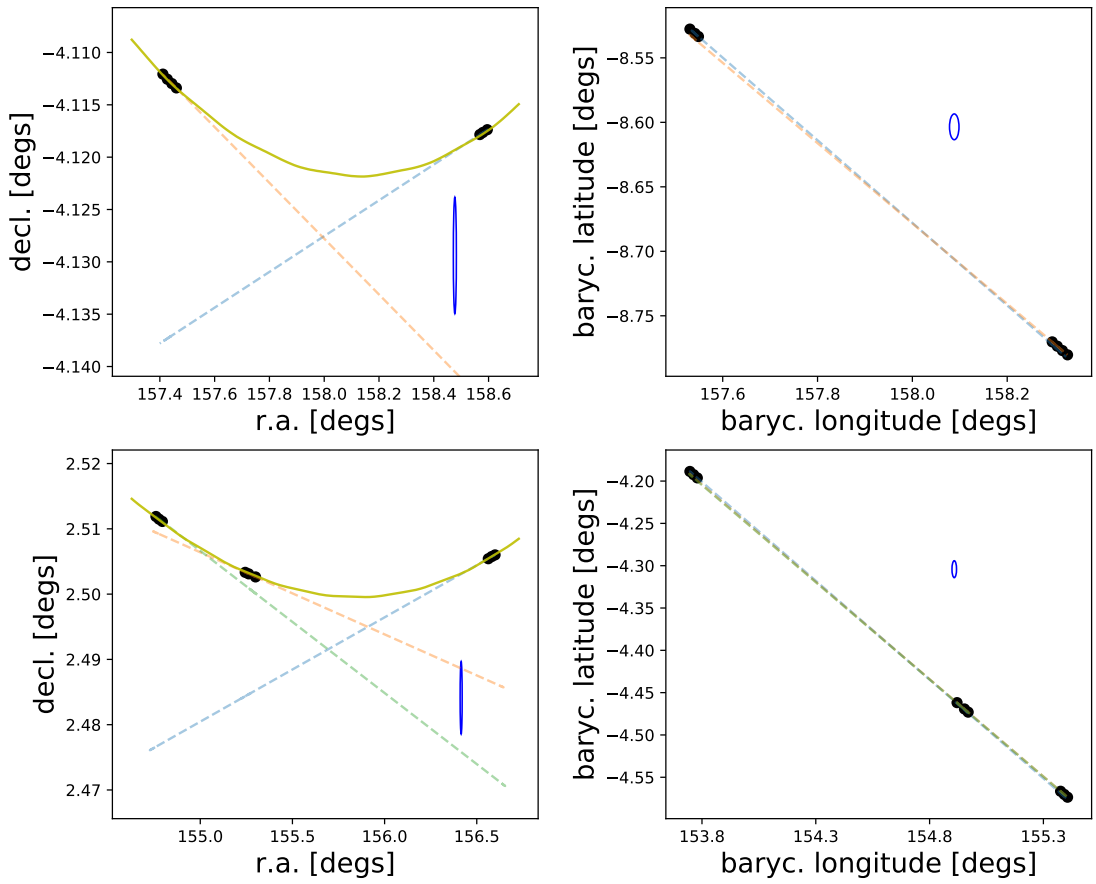

Figure 3.2: Known asteroids with difficult trajectories. The upper two panels show the asteroid 2009 CP21 and the lower two panels the asteroid 2017 SJ103. On the left, in equatorial coordinates, the HiTS detections (black dots) and the trajectory as estimated by JPL Horizons (yellow line) are shown. On the right, in black dots, are shown the barycentric coordinates as estimated assuming barycentric distances similar to the actual ones. Dashed lines show linear fittings for all tracklets and the blue circles show the maximum distance between estimated coordinates to join these tracklets into tracks (20″ for the first linking algorithm working in equatorial coordinates and 36″ for the last algorithm working in barycentric coordinates).

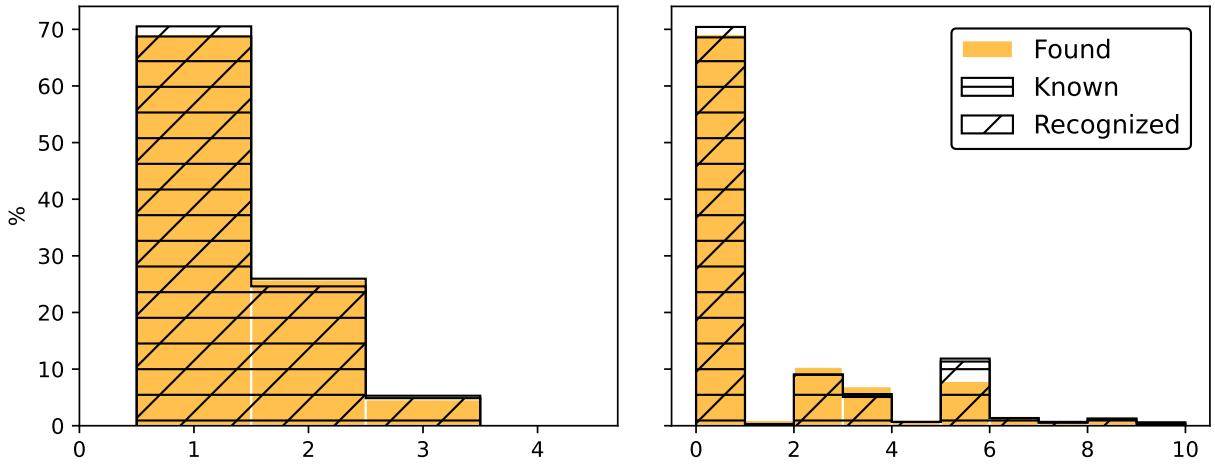

Figure 3.3: Left panel: percentage of clusters grouped by their number of tracklets. Right panel: percentage of clusters grouped by their time arc. In yellow all found clusters are shown, the known ones –if perfectly linked– are shown with horizontal lines, and as actually found with diagonal lines. In total there are 7945 tracklets grouped in 5674 clusters (yellow), 1324 known bodies among those tracklets (horizontal lines) that were found in 1403 clusters (diagonal lines).

3.4.2 Magnitude Distribution

For each track it was computed a mean magnitude g. Figure 3.6b shows the distribution for all tracks in blue, for those that were recognized as known bodies in green and for all known bodies in orange (regardless of whether they were linked or not).

In Figure 3.7 we show the luminosity function (LF) in the apparent g magnitudes for almost all tracks. We left out 37 that showed non-MB orbits considering a criterion similar to that in Yoshida et al. (2003) and Yoshida & Nakamura (2007) (namely, only tracks with MB-like ecliptic velocities of $< -0.15°\text{day}^{-1}$ were included[3]). We expect some contamination among those 5703 track from bodies outside the MB (specially from NEOs), but we do not expect it to be larger than 1%.

The LF exhibits a very clear break that was fit with the harmonic mean of two power laws or double power law (DPL, see equation 3.1) using the same method shown in Bernstein et al. (2004), Fuentes & Holman (2008) and Fuentes et al. (2009), based on the likelihood function derived by Schechter & Press (1976).

$$\begin{aligned} \sigma(m) &= (1+c)\sigma_{20}\left[10^{-\alpha_1(m-20)} + c10^{-\alpha_2(m-20)}\right]^{-1} \\ c &= 10^{(\alpha_2-\alpha_1)(m_{eq}-20)} \end{aligned} \tag{3.1}$$

The LF parameters in equation 3.1 were constrained using Python's package `emcee`[4] (Foreman-Mackey et al., 2013) which applies a Markov Chain Monte Carlo (MCMC) ensemble sampler with affine invariance (Goodman & Weare, 2010), returning an approximation

[3]Obtained by linearly fitting geocentric ecliptic coordinates using `Python`'s (`https://www.python.org/`) `astropy` package (`https://www.astropy.org/`).

[4]`https://emcee.readthedocs.io/`

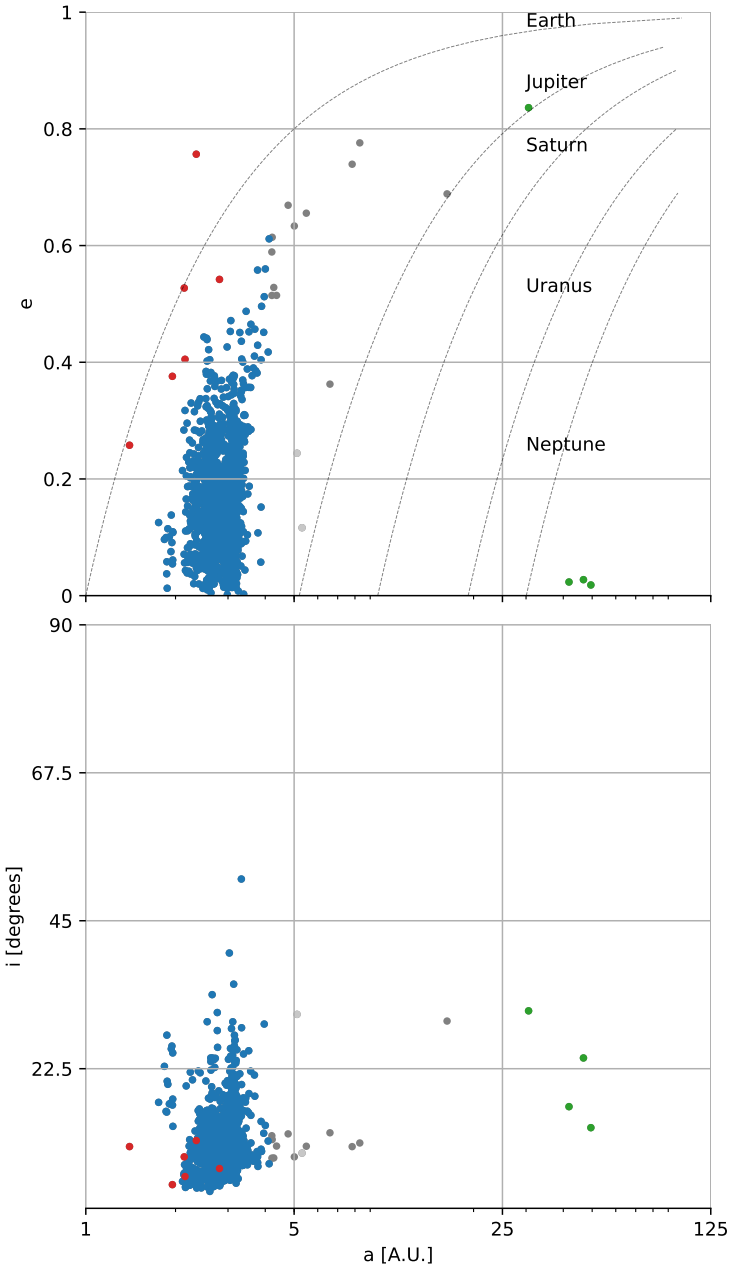

Figure 3.4: Orbital solution for all tracks detected in at least two nights that yield bound orbits and a maximum deviation of 2″ from the model. There are 1762 objects in 2015 that fulfill this criterion. The lines show the solutions that share their pericenter distance with the outer planets. We show Near Earth Objects in red, Main Belt asteroids in blue, Trans-Neptunian objects in green and others in gray. No Centaurs were found.

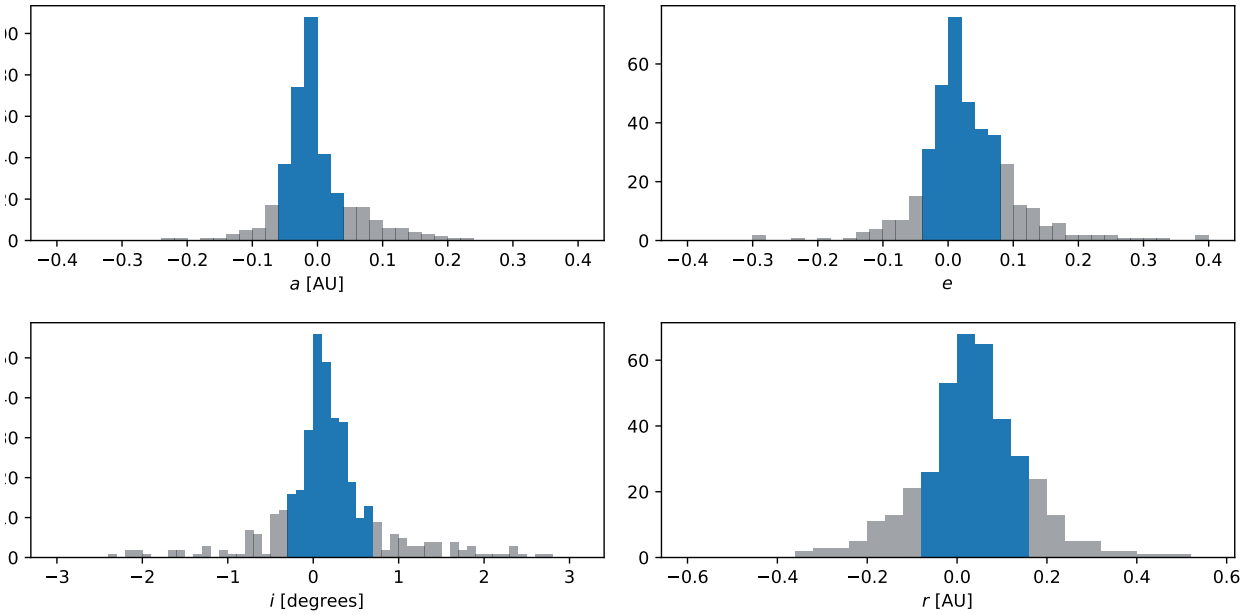

Figure 3.5: Errors for the estimated orbits of known asteroids detected in more than one night and with bound computed orbits with fitting errors of $\leq 2''$. We highlight the 1σ confidence region (in blue). From top to bottom we show errors in semi-major axis a, eccentricity e, inclination i, barycenter distance r and observer distance Δ. The implied 1σ confidence region for our orbital solutions is: $\sigma_a = [-0.06, 0.04]$ au, $\sigma_{\rm e} = [-0.04, 0.08]$, $\sigma_{\rm i} = [-0.3, 0.7]$ degrees and $\sigma_r = [-0.08, 0.16]$ au.

of the probability distribution of the models' parameters. This consider a total survey area $\Omega = 138\,\mathrm{deg}^2$ and detection efficiency $\eta(m)$ as in Förster et al. (2016) (equation 3.2, with erf the error function[5]). Taking into account image subtraction and multiple detections yields parameters $m_{50} = 23$ and $\Delta m_{50} = 1.1$ for the detection efficiency function of asteroids.

$$\eta(m) = \frac{1}{2}\left[1 + \mathrm{erf}\left(-\frac{m - m_{50}}{\Delta m_{50}}\right)\right] \tag{3.2}$$

Considering $\eta(m)$ and detections up to the limiting magnitude of our survey ($g \sim 23$), it limits the sample to 5119 objects. Each of the 200 walkers used for this algorithm started at a random position near the parameter value obtained using the common χ^2 minimization method. Using the mode with a $\pm 34\%$ confidence interval, we finally got $\alpha_1 = 2.94^{+0.48}_{-0.48}$, $\alpha_2 = 0.44^{+0.01}_{-0.01}$, $\sigma_{20} = 1.86^{+0.22}_{-0.15}$ and $m_{eq} = 19.78^{+0.06}_{-0.06}$.

This LF is very similar to that found by Gladman et al. (2009), with a break at $R \sim 19$, consistent with our $m_{\rm eq} \sim 19.78$ (our mean color $g - r \sim 0.77$, see Table 3.3). They got flatter slopes, especially at the bright end: $\alpha = 0.61$ compared to our much steeper $\alpha_1 \sim 3.1$; while at the faint end they got $\alpha = 0.27$ against our $\alpha_2 = 0.44$. The expected number of bodies is also lower for our survey: Gladman et al. (2009) found ~ 90 bodies per square degree brighter than $R \sim 22$, while we only found ~ 30 bodies brighter than $g \sim 22.7$. This is accounted by the fact that they pointed directly at the ecliptic while in this work the area closest to the ecliptic is at $\sim 8°$ with the bulk of our data being at $\sim 15°$. This is consistent

[5] $\mathrm{erf}(x) = \frac{2}{\pi}\int_0^x \mathrm{e}^{-t^2}\mathrm{d}t$

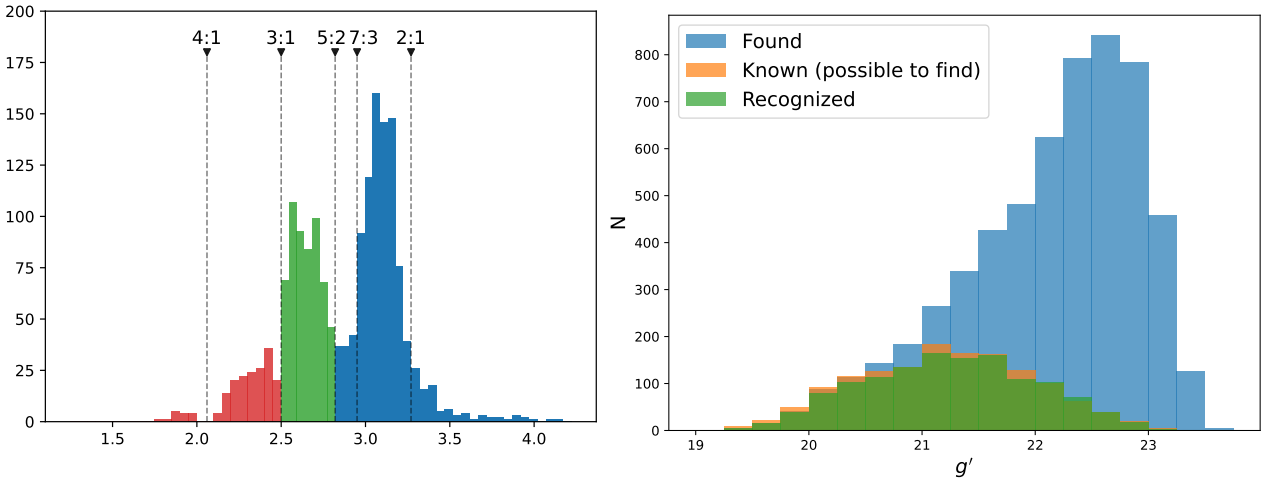

(a) **(b)**

Figure 3.6: *(a)* Main Belt distribution as a function of semi-major axis for the 1,738 bodies with *good* orbital solutions (see Figures 3.5 and 3.4). Important Kirkwood gaps for resonances 4:1, 3:1, 5:2, 7:3 and 2:1 with Jupiter are plotted in dashed lines, defining the Inner Belt (red), the Intermediate Belt (green) and the Outer Belt (blue), each one with 181, 566 and 991 bodies, respectively. *(b)* Histograms of the number of asteroids per magnitude (g band). In orange, known asteroids (from JPL) that the linking process can find (wich have at least three detections in any night). In blue, tracks found in the HiTS data. In green, those tracks that were recognized as known objects (at least three detections within $4''$ of a JPL detection). The drop in the blue histogram appears consistent with Figure 7 in Förster et al. (2016) once the effect of image subtraction is taken into account, which results in a loss of $\sim$0.4 mag.

with the results by Ryan et al. (2009), who showed that the number of detected asteroids decreases with ecliptic latitude by 50% and 20% at 10° and 15° with respect to 0°.

3.4.3 Absolute Magnitude Distribution

Absolute magnitudes H were computed for all *good tracks*. In equation 3.3 r is the body-barycenter distance, Δ is the body-observer distance, α is the phase (Sun-body-observer angle), and $\phi(\alpha)$ is the phase function (see Waszczak et al. 2015 for several definitions of ϕ). The (H, G) model was used for ϕ (Bowell et al., 1989), using the typical value of $G = 0.15$ (as in the ephemeris data delivered by MPC and JPL). Since this data has detections mainly in g and some in r, the absolute magnitudes for each filter, H_g and H_r was computed. The average absolute magnitude for a track is reported.

$$H = V - 5\log_{10}(r\Delta) + 2.5\log_{10}[\phi(\alpha)] \tag{3.3}$$

Since H can be related with the body's size by the equation $D = 10^{-H/5}1329/\sqrt{p_V}$, where D is the diameter in km and p_V the geometric albedo, we sought for a possible color–size relation in the MB using H as a proxy for the size (assuming a common p_V for all bodies). Figure 3.8 shows the cumulative *size* distribution (CSD) for the 1182 MB bodies measured

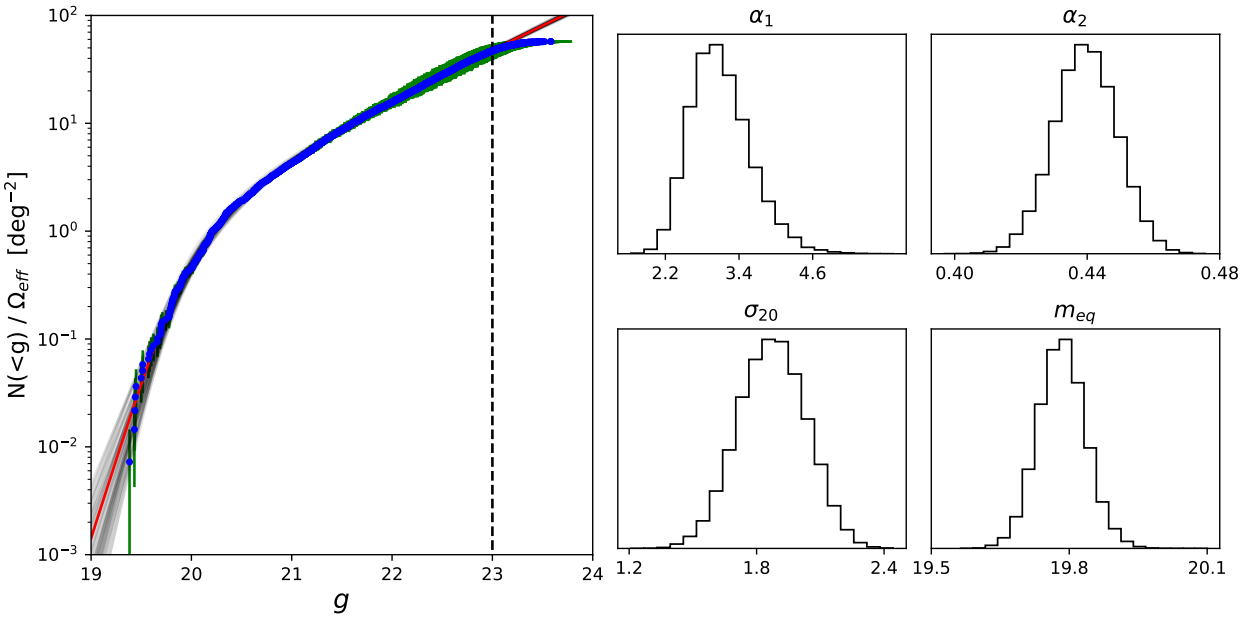

Figure 3.7: Cumulative distribution of magnitude g for the 5703 tracks with MB-like velocities (see section 3.4.2). A DPL (equation 3.1) was fitted using MCMC to the 5119 bodies brighter than 23 g (marked with a dashed line). The small panels show the DPL parameters distribution. Using the mode with a $\pm 34\%$ confidence interval it gets $\alpha_1 = 2.94^{+0.48}_{-0.48}$, $\alpha_2 = 0.44^{+0.01}_{-0.01}$, $\sigma_{20} = 1.86^{+0.22}_{-0.15}$ and $m_{eq} = 19.78^{+0.06}_{-0.06}$. The red line shows the DPL given by the median values and the gray lines show 50 random models from the MCMC procedure.

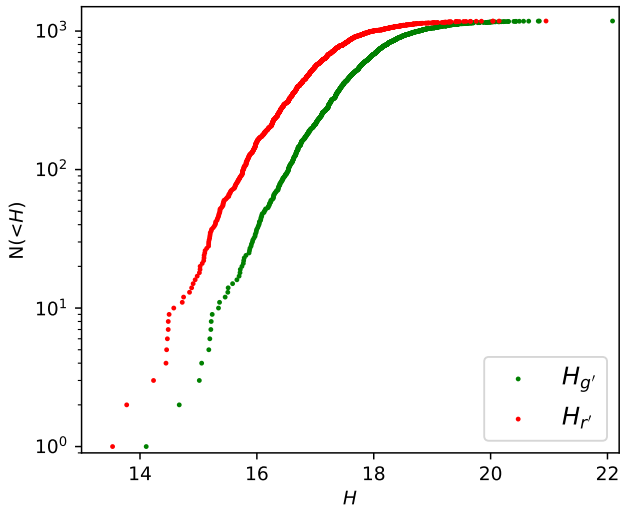

Figure 3.8: Cumulative distribution of H_g and H_r for the 1182 MB bodies with *good* orbital solution and measurements in g and r bands.

in g and r bands. Both H_g and H_r distributions are well represented by a single power law (SPL) with the same slope (~ 0.88), showing no evidence for any color–size relationship in our data. This result was unchanged even when we considered each MB zone separately (Inner, Middle and Outer).

The following analysis only considers H_g since all tracks were observed in g. Following the process described in section 3.4.2, we fit an SPL distribution $\sigma = \alpha \ln(10) 10^{\alpha(mag - H_0)}$ using only bodies brighter than our limiting magnitude ($g \sim 23$). The SDs are shown in Figure 3.9 and the most likely parameters are summarized in Table 3.2. The MB as a whole or by subregion exhibits slopes much steeper than measured by other studies, only comparable to the ones measured by Parker et al. (2008) for brighter objects.

Since DECam has similar filters to those in SDSS (Schlafly et al., 2018), Lupton (2005)[6] was used to transform H_g to H (g to V). Lupton found that $V \sim g - 0.58(g - r)$ (similar to the results found by Fukugita et al. 1996 and Krisciunas et al. 1998). Assuming all bodies have the same color and albedo, $g - r \sim 0.76$ (see section 3.4.4), and $p_V = 0.1$ (roughly the mean albedo from Polishook et al. 2012), sizes range between $1 < D < 10$ km for objects between $14 < H_g < 18$.

3.4.4 Color

The 2015 HiTS campaign observed in both g and r, but most revisits were in g, enabling to detect tracks in both filters and produce colors for some of our tracks. In this section are reported $g - r$ colors from $H_g - H_r$ (section 3.4.3) for the 1203 *good tracks* measured in both bands. Figure 3.10 shows these colors for the 1182 located in the region of the Main Belt as a function of their orbital parameters and in Figure 3.11 the $g - r$ distribution in the entire Main Belt is shown separated by class: Inner, Intermediate and Outer Belt. In both figures is observed that asteroids are mainly red, with a mean color of $g - r \sim 0.756 \pm 0.008$ for all

[6] `http://classic.sdss.org/dr7/algorithms/sdssUBVRITransform.html`

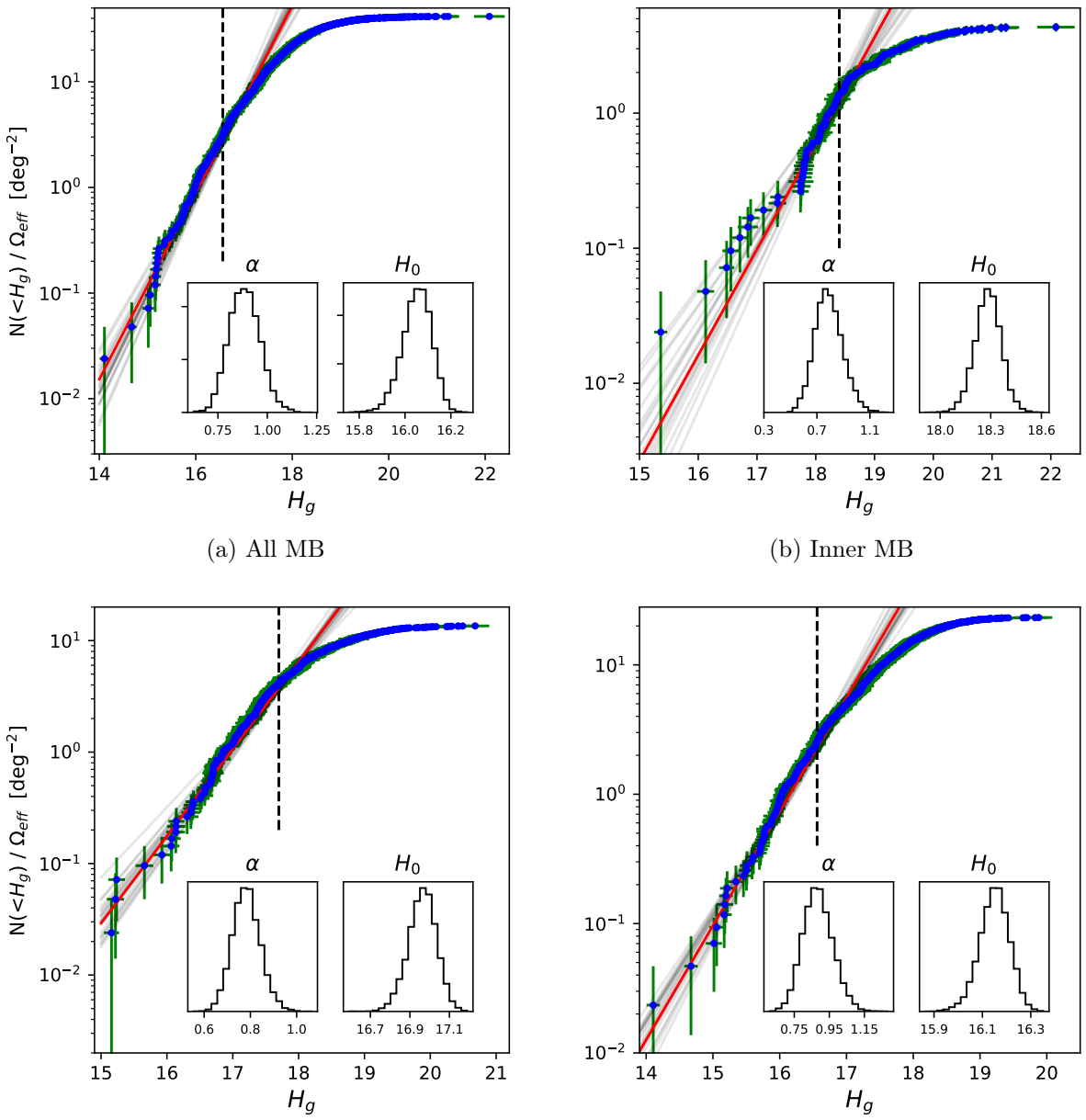

(a) All MB

(b) Inner MB

(c) Intermediate MB

(d) Outer MB

Figure 3.9: Cumulative H distribution of bodies with good orbital solutions for different MB groups. A single power–law distribution was fit ($\sigma(H_g) = \alpha \ln(10) 10^{\alpha(H_g - H_0)}$), with the two smaller panels showing the parameter distribution. In red is shown the model given by the median values and in gray models given by 20 random values from the parameter distributions. Dashed lines mark the limiting magnitude (only brighter bodies are considered for the fit). A summary of the fitting results is in Table 3.2.

Table 3.2: Main Belt SPL fitting

Population[a]	H_{lim}^{b}	N[c]	α^{d}	H_0^{d}
Main Belt	16.56	129	$0.88^{+0.09}_{-0.08}$	$16.04^{+0.09}_{-0.05}$
Inner Belt	18.4	57	$0.76^{+0.13}_{-0.10}$	$18.28^{+0.09}_{-0.09}$
Intermediate Belt	17.7	173	$0.79^{+0.06}_{-0.06}$	$16.96^{+0.1}_{-0.07}$
Outer Belt	16.56	108	$0.86^{+0.12}_{-0.08}$	$16.14^{+0.09}_{-0.06}$

Notes

[a] As defined in Section 3.4.1.

[b] Limiting H_g magnitude for fitting.

[c] Number of bodies brighter than H_{lim}.

[d] Values are the median with a confidence interval of ±34% from the distribution.

of them. Although it could not be recognized any color–size dependency (section 3.4.3), I recovered the known color-distance relationship (Yoshida & Nakamura, 2007; Gladman et al., 2009), as seen in Figure 3.11. The mean colors shown in Figure 3.11 are summarized in Table 3.3, reflecting how MB asteroids are bluer farther from the Sun. This dependency is usually explained as an asteroid type dependency: the outer belt would be dominated by C-type asteroids (bluer) and the inner belt would be dominated by S-type (redder); (as seen in many color plots; e.g., Ivezić et al. 2001; Yoshida & Nakamura 2007; Gladman et al. 2009). Using Ivezić et al. (2001) as a reference, the $g - r$ limit between C– and S–types would be around ~ 0.55, meaning that the vast majority of these asteroids would be S-type in the three MB divisions. However, it was not possible to recognize any clear bimodality as in Ivezić et al. (2001) to distinguish between types.

The lack of the expected bimodality in color can be explained by taking into account the asteroids' intrinsic lightcurves due to rotation. Most asteroids exhibit some variation with periods that range from ∼2 hours to ∼2.5 days (remember our 1.6 hour cadence), changing their brightness by 0.1 to 1.2 magnitudes (Polishook et al., 2012; Waszczak et al., 2015). Another posible contaminating source in our sample are NEOs, which exhibit similar rotational periods (Vaduvescu et al., 2017). The reported colors were measured as the average H_g (several values) minus the average H_r, the latter generally being only one value measured at ∼1.6 hours from the nearest g measure. This means that colors reported in this work have a big uncertainty due to asteroid's rotation. In comparison, SDSS colors are measured within ~ 5 minutes (Ivezić et al., 2001). WISE, for example, observed in 4 bands simultaneously (Wright et al., 2010) allowing the measurement of p_V for bodies with accurate orbital parameters and obtaining a strong bimodality associated with composition (Masiero et al., 2011).

Outside the Main Belt, colors were obtained for 12 known objects: 5 NEOs, 3 TNOs and 4 Jupiter family comets (JFCs). Colors for these bodies can be seen in Table 3.4. NEOs have colors somewhat bluer than the MB's average color, which is consistent with Dandy et al. (2003), who claim the MB as a possible source, finding NEOs bluer than expected. The 4 JFCs are redder than the mean color of the MB, but inside the MB color range as seen in Solontoi et al. (2012) (in $g - r$, with Ivezić et al. 2001 and this work for comparison) or in Lamy & Toth (2009) and Jewitt (2015) (in $B - R$, with Yoshida & Nakamura 2007 for comparison). For the TNOs, following the classification algorithm defined by Gladman et al.

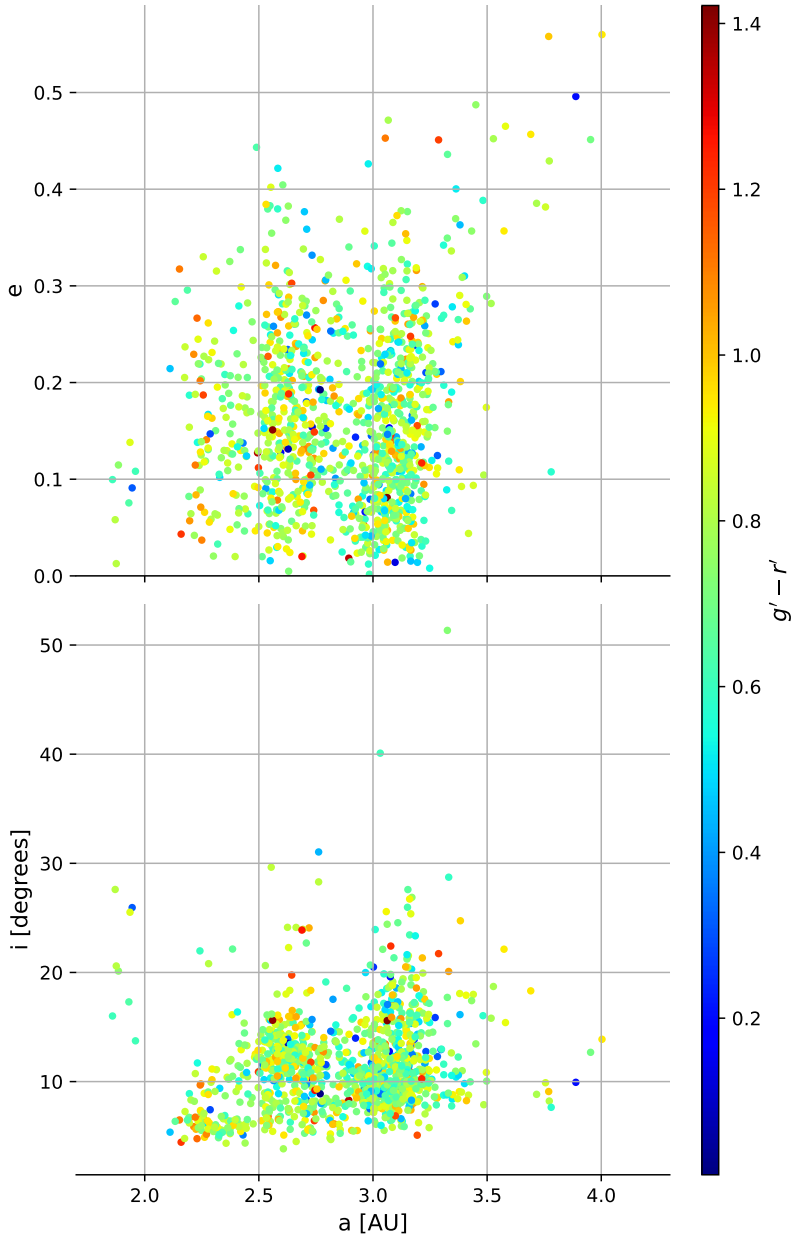

Figure 3.10: Same as Figure 3.4 but for Main Belt objects only that were also measured in r with their respective $g - r$ color (measured from their H_g and H_r values).

Table 3.3: $g - r$ colors for the Main Belt

Population[a]	N[b]	Mean	Stand. Dev.
Main Belt	1182	$0.756 \pm .008$	$0.181 \pm .008$
Inner Belt	133	$0.797 \pm .031$	$0.175 \pm .033$
Intermediate Belt	369	$0.776 \pm .015$	$0.186 \pm .015$
Outer Belt	680	$0.737 \pm .010$	$0.177 \pm .010$

Notes

[a] As defined in Section 3.4.1.

[b] Number of bodies in each population.

Comments

The errors in the last two columns are computed taking into account the magnitudes errors and the confidence intervals shown in Section 3.4.1 (Figure 3.5).

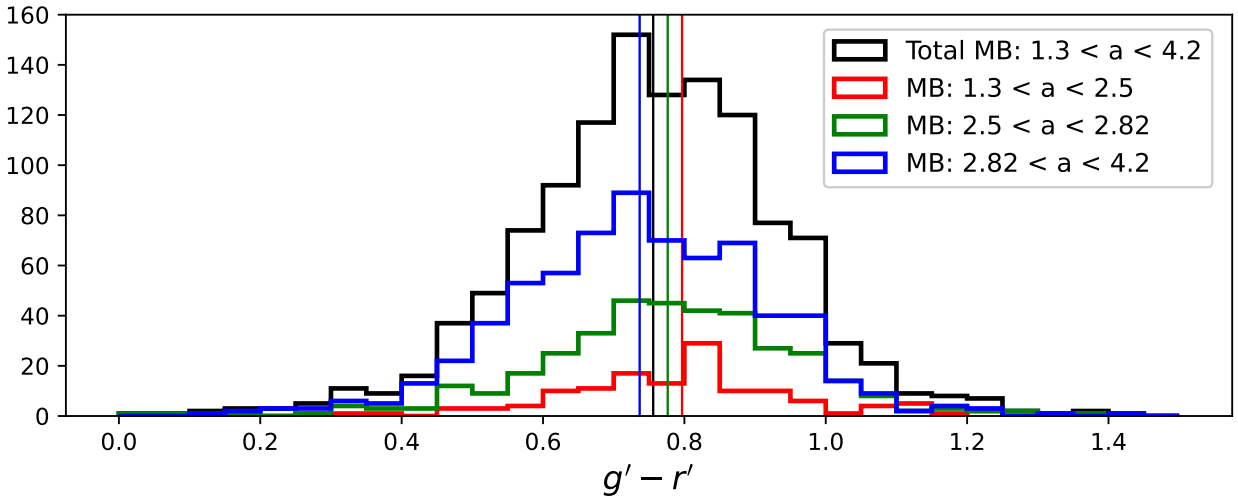

Figure 3.11: Histograms of the color of Main Belt asteroids. In black: all Main Belt asteroids; in red: Inner Belt; in green: Intermediate Belt; and in blue: Outer Main asteroids. Vertical lines mark the mean color for each population (see Table 3.3). Notice that the average $g - r$ colors for C and S asteroids (based in Ivezić et al. 2001) are 0.45 and 0.65 respectively.

Table 3.4: $g - r$ colors for Non Main Belt known bodies

Name[a]	Type[b]	$g - r$[c]	H_g
2003 HU42	NEO	0.67 ± 0.20	18.00 ± 0.01
2008 VU4	NEO	0.75 ± 0.18	18.04 ± 0.05
2003 SS214	NEO	0.60 ± 0.16	20.14 ± 0.06
2014 WL368	NEO	0.85 ± 0.05	20.19 ± 0.04
2017 JB	NEO	0.47 ± 0.12	23.66 ± 0.08
C/2015 D2	JFC	0.80 ± 0.04	13.29 ± 0.02
P/2011 U2	JFC	1.064 ± 0.030	13.96 ± 0.01
C/2014 A5	JFC	0.87 ± 0.10	15.43 ± 0.04
317P/WISE	JFC	0.79 ± 0.08	18.93 ± 0.07
2013 FZ27	TNO	0.92 ± 0.05	4.72 ± 0.02
2012 BA155	TNO	1.17 ± 0.15	6.57 ± 0.10
2014 XW40	TNO	1.25 ± 0.13	6.79 ± 0.07

Notes

[a] As identified by the MPC and JPL.

[b] NEO: Near Earth Object; JFC: Jupiter Family Comet (as identified by the JPL Small-Body Database Browser); TNO: Trans-Neptunian Object.

[c] Colors computed as the difference of the averaged H_g and H_r. The errors only consider magnitude uncertainty. To calculate H we use orbital data (r and Δ) from JPL Horizons.

(2008) and using the limit for scattered objects by Lykawka & Mukai (2007), (531017) 2012 BA_{155} is a 2:5 resonant body, 2014 XW_{40} is a scattered TNO and (523671) 2013 FZ_{27} is in the limit between scattered and hot, outer classical TNO (and is also near the detached TNO zone). These 3 TNOs have red colors compatible with their respective families (Sheppard, 2010; Jewitt, 2015; Pike et al., 2017; Terai et al., 2018).

3.5 Summary and Discussion

Using data from the HiTS 2015 campaign, 5740 SS minor bodies were found. Considering only bodies with an observation arc longer than one night it was possible to identify 1738 MB asteroids (397 of them were known bodies), getting color information for 1182 of them.

The luminosity function for all bodies with apparent motions compatible with MB bodies (5703 in total) is well fit by a DPL, similar to the one found by Gladman et al. (2009), with a break in a similar magnitude but with much steeper slopes.

The size distribution for the MB population was found to be compatible with a SPL for the entire population as well as for the Inner, Intermediate and Outer MB separately.

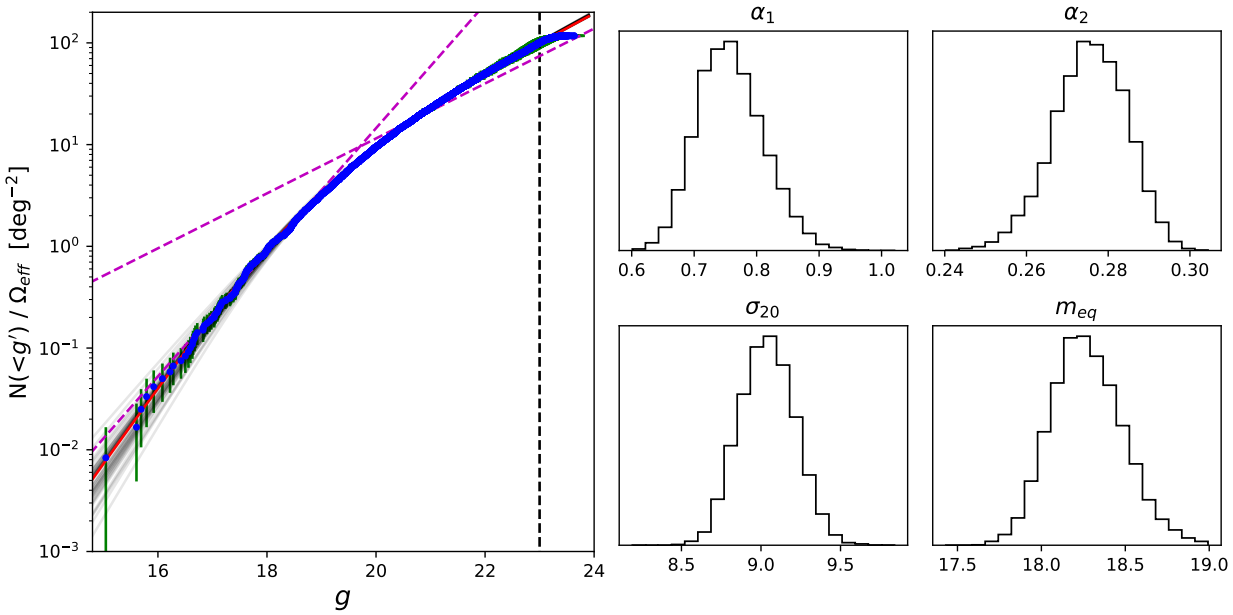

Figure 3.12: Cumulative distribution of magnitude g for the 12,928 tracks with MB-like velocities from the 2014 HiTS campaign (see section 3.5). A DPL was fit using MCMC to the 11,419 bodies brighter than 23 g (marked with a black dashed line). The small panels show the DPL parameter distributions. Using the mode with a $\pm 34\%$ confidence interval, it yields $\alpha_1 = 0.76^{+0.05}_{-0.06}$, $\alpha_2 = 0.28^{+0.01}_{-0.01}$, $\sigma_{20} = 9.03^{+0.18}_{-0.18}$ and $m_{eq} = 18.16^{+0.33}_{-0.11}$. The red line shows the DPL given by the mode values and the gray lines show 50 random models from the MCMC procedure. In magenta dashed lines there is a proxy of the distribution by Gladman et al. (2009), considering they found ~ 100 bodies at $R \sim 19.1$ at the bright end (slope of 0.61), ~ 1000 bodies at $R \sim 23$ at the faint end (slope of 0.27), $\Omega = 8.4\text{deg}^2$ and approximating $g - R \sim 0.76$ (from Section 3.4.4).

3.5.1 Size Distribution and Ecliptic Latitude

The slopes computed in the size distributions are much steeper than in any other survey, only comparable to the ones found by Parker et al. (2008) for bright bodies. The lower surface density of detections in HiTS 2015 is consistent with Gladman et al. (2009) taking into consideration the amount of asteroids by ecliptic latitude found by Ryan et al. (2009), so the steep values found in here would be caused by a lack of bright bodies (less numerous but able to flatten the distribution). The apparent lack of bright bodies could be an effect of the ecliptic latitudinal distribution of asteroids on the observed luminosity function or it could be an effect of the analysis of HiTS moving objects. The *deep learning* analysis that distinguishes between real and bogus detections was designed for static (not elongated) transients and not specifically for moving objects, but there is no reason to believe it would discriminate bright bodies worst than faint bodies.

The latitudinal dependence was explored by analyzing the SD of asteroids from the HiTS 2014 campaign (Chapter 2). Those asteroids were found mainly between ecliptic latitudes 0° and 15°. Using bodies with an apparent ecliptic latitude velocity compatible with the MB (less than $-0.16°\text{day}^{-1}$ instead of less than $-0.15°\text{day}^{-1}$ as for the 2015 data because in 2014 campaign we have Jupiter trojans around $-0.15°\text{day}^{-1}$) and following the same procedure

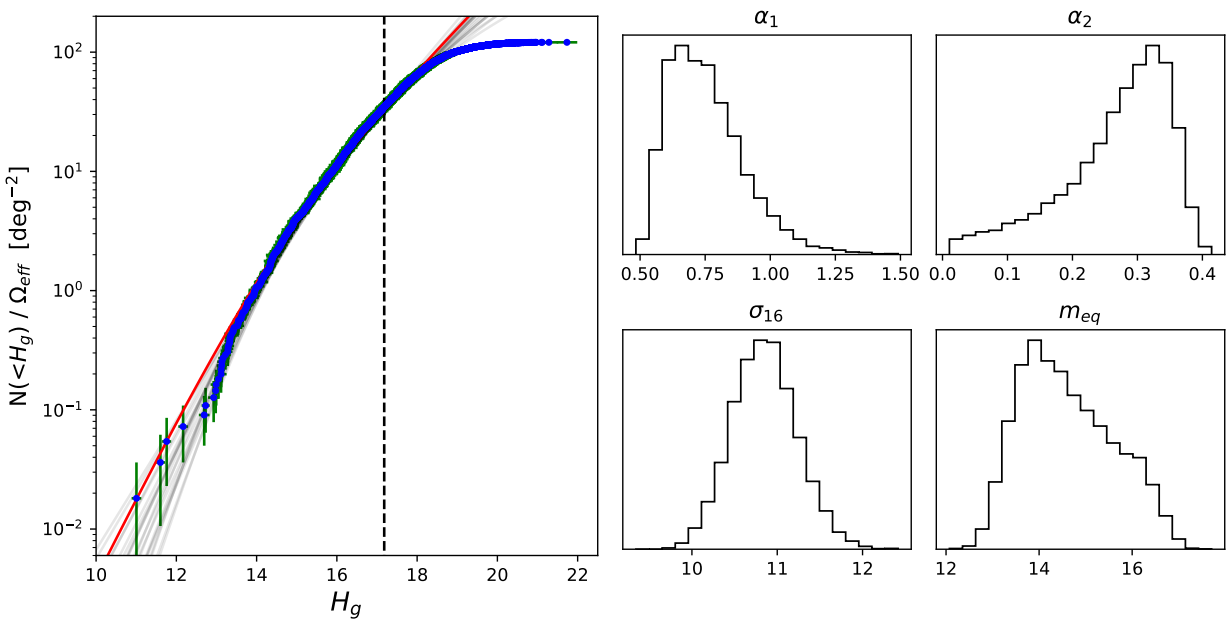

Figure 3.13: Cumulative H distribution for all 6679 MB bodies with good orbital solutions from the 2014 HiTS campaign (following the same criteria as for the 2015 HiTS campaign). A DPL (see text) was fit using MCMC to the 1729 bodies brighter than $H_g = 17.06$ (marked with a dashed line). The small panels show the DPL parameter distributions. Using the mode with a $\pm 34\%$ confidence interval, it yields $\alpha_1 = 0.68^{+0.17}_{-0.09}$, $\alpha_2 = 0.34^{+0.04}_{-0.11}$, $\sigma_{16} = 10.85^{+0.40}_{-0.40}$ and $m_{eq} = 13.82^{+1.63}_{-0.51}$. The red line shows the DPL given by the mode values and the gray lines show 20 random models from the MCMC procedure.

as in Section 3.4.2 (using $m_{50} = 23.6$ and Δm_{50}=1.1 for η in equation 3.2 and $\Omega = 120\text{deg}^2$ for the surveyed area), the distribution shown in Figure 3.12 was obtained, which exhibits a slope of ~ 0.76 for the bright end and a slope of $\sim .28$ for the faint end. These values are very similar to (although somewhat steeper than) the values found by Gladman et al. 2009 (see dashed lines from Figure 3.12). Continuing the analysis of the 2014 data, the SD for all "*good*" tracks was computed (using the same criteria from Section 3.4.1) and fitted a DPL to it (an SPL was not enough to fit the data). This DPL has the same form as equation 3.1, but instead of using magnitude 20 as reference, we used magnitude 16[7]. The result is shown in Figure 3.13, where the DPL was fitted using data up to a limiting magnitude $H_g = 17.18$ (using a limiting magnitude of $g = 22.5$ for 90% completeness and a phase angle of less than 9.2°). The resulting slopes are $0.68^{+0.17}_{-0.09}$ at the bright end and $0.34^{+0.04}_{-0.11}$ at the faint end, which is consistent with previous results such as Ivezić et al. (2001) and Gladman et al. (2009). This supports the hypothesis that the steeper slopes for the 2015 campaign are due to a lack of bright sources at higher latitudes.

3.5.2 Colors and Asteroids Rotation

The colors reported are mostly similar to S-type bodies in the MB. They do not exhibit bimodality in color. In order to explain this I simulated an intrinsic bimodal population like the one by Ivezić et al. (2001) (left panel of Figure 3.14). To measure how asteroids'

[7]The reference magnitude was changed to allow the `emcee` algorithm to properly converge.

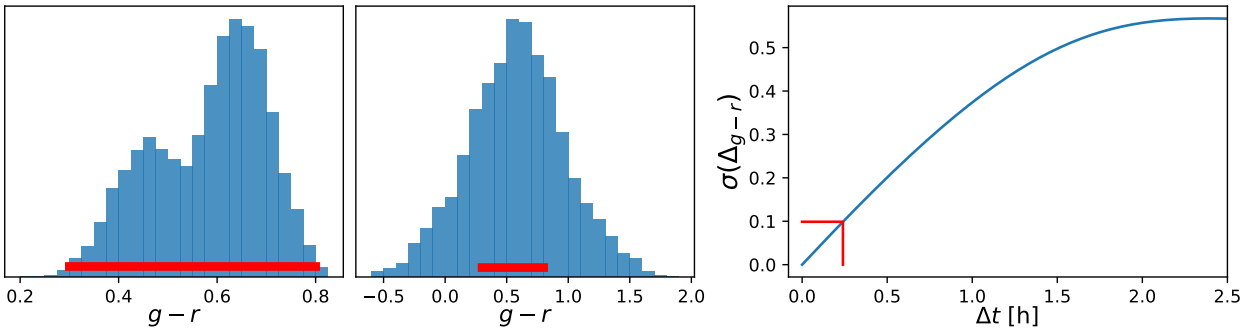

Figure 3.14: Left panel: simulated color bimodality resembling the one seen in Ivezić et al. (2001). Middle panel: apparent color due asteroids' rotation (see text). In both, left and middle panels, the red line covers the same range, showing how the apparent color distribution gets wider because asteroids' rotation. Right panel: Standard deviation of the errors in color using consecutive measurements $\sigma(\Delta_{g-r})$ of the simulated population (left panel) vs. time between observations Δt. In red we indicate the time separation $\Delta t = 0.24$hr that yields an uncertainty $\sigma(\Delta_{g-r}) = 0.1$ small enough to detect bimodality in the color distribution (see text).

rotation affects the measured color, their magnitudes were modeled as $m = m_0 + A\sin(2\pi(\phi + f\Delta t))$ with m the measured value, m_0 the mean magnitude (pseudo-randomly generated with equation 3.1 as a probability distribution), A the magnitude variation (obtained from a pseudo-random triangular distribution between 0 and 1.2 magnitudes with the mode at 0.2), f the rotation's frequency (obtained from a pseudo-random triangular distribution between 0.5 and 10 days^{-1} with the mode at 0.5), ϕ the phase of the first observation (obtained from a pseudo-random flat distribution) and Δt the time between one observation and another ($\Delta t = 0$ for the simulated first observation and $\Delta t = 1.6$ hours for the second observation in the HiTS 2015 case). The A and f distributions are based on Waszczak et al. (2015). Finally, the computed apparent color $g - r$ (with g obtained as m_0 and r as $m(\Delta t = 1.6h)$) is shown in the middle panel of Figure 3.14, where the color distribution has broadened and lost any bimodality. Then I estimated the effect of a time lag between filters on colors due to an asteroid's rotation. In Figure 3.14, right panel, is shown the standard deviation of the errors between consecutive measurements of the simulated population ($\sigma(\Delta_{g-r})$) as a function of the time between those observations; since the two modes of the *"true"* color distribution (left panel in Figure 3.14) are 0.2 magnitudes apart, a rough $\sigma(\Delta_{g-r})$ limit of at most 0.1 to detect the bimodality was set. This value is found at $\Delta t = 0.24$ hours or ~ 14 minutes (red lines in the right panel of Figure 3.14). This is an important constraint for future surveys to account for when measuring colors of asteroids.

Chapter 4

Colors of Irregular Satellites of Saturn with DECam

4.1 Irregular Satellites Origin

Irregular satellites (Irrs) are minor bodies characterized by large orbits with high inclinations and/or high eccentricities, many of them retrograde, in contrast with the nearly circular, co-planar and compact orbits of regular satellites. They have been found orbiting the giant planets and because of their extreme orbits it is assumed that this is a population captured at some point during the Solar System evolution (Kuiper, 1956). As discussed in Chapter 1, as many other small bodies, Irrs are thought to be captured during the migration and orbital instability of the giant planets. Simulations run by Nesvorný et al. (2007, 2014) showed that they could have been captured from nearby bodies in the planetesimal disk during planet migration, yielding similar numbers and size distributions (Sheppard et al., 2006) as those observed today.

Trans–Neptunian Objects (TNOs) are the least evolved remnants of the planetesimal disk, in part because a relatively lower solar irradiation that has not affected their surface properties as other closer population. Since Irrs are expected to be captured TNOs during the early history of the giant planet dynamical evolution, it is expected that the color properties of TNOs and Irrs should be similar. It has been found that TNOs show a high diversity of sizes and colors, from red ($B - R \sim 1.3 \pm 0.3$ or $g - r \sim 0.6 \pm 0.2$) to ultra red bodies ($B - R \sim 1.8 \pm 0.2$ or $g - r \sim 1 \pm 0.2$) (Sheppard, 2010, 2012; Peixinho et al., 2015; Pike et al., 2017; Terai et al., 2018; Chen et al., 2018; Thirouin & Sheppard, 2019). At the same time, colors of many Irrs have been measured (around half of their known populations), especially those from Jupiter (JIrrs) and Saturn (SIrrs) (Sykes et al., 2000; Rettig et al., 2001; Grav et al., 2003; Grav & Holman, 2004; Grav et al., 2004; Bauer et al., 2006; Grav & Bauer, 2007; Grav et al., 2015; Graykowski & Jewitt, 2018; Maris et al., 2018), finding that there are no ultra-red bodies among the Irrs as among the TNOs, raising questions about their actual origin and their evolution. Hence the necessity of gathering more data about these bodies to have a more complete perspective and see if current models are still valid or new ones are necessary.

In this chapter I present observations pointing at known SIrrs aiming to detect sources until magnitude $\sim R = 25$ (namely, almost all SIrrs known until then, July, 2019) Avoiding SIrrs to move a distance bigger than one PSF in one image force exposure to be not longer than two minutes, leaving these sources beyond the magnitude limit. To detect such faint objects is necessary to use the "pencil-beam" or "shift and stack" method (Gladman et al., 1998; Holman et al., 2004; Kavelaars et al., 2004; Fuentes et al., 2009). Observation were done in gri in order to obtain $g-r$ and $r-$i colors, aiming to obtain clues about their parent family using color comparisons. Despite observing against crowded fields and having non-photometric nights, in this chapter is reported the highest number of SIrrs colors obtained in one single survey so far (21 SIrrs with $r-$i and 16 with $g-r$). In section 4.2.1 is explained the observing plan and the resulting data; in section 4.3 is explained the data processing used to obtain SIrrs photometry; in section 4.4 are shown the color results for the detected SIrrs; in section 4.5 are compared these results with colors from other works and discuss about their sources of error. General conclusions are in Chapter 5, where are summarize the main findings, putting them in the context of other populations and current SS evolution models, as well as laying out lessons for future surveys that aim at obtaining pencil-beam photometry.

4.2 Data

4.2.1 Survey Strategy

This observations were made with the Dark Energy Camera (DECam). As indicated in previous chapters, DECam is mounted at the prime focus of the Blanco 4 meters telescope at the Cerro-Tololo International Observatory (CTIO[1]). DECam covers a 3 square degree field of view with a mosaic of ~ 60 ccd of 2Kx4K pixels, yielding a $0.27''$/pixel resolution (DePoy et al., 2008). These characteristics allowed to cover almost all SIrrs using only two different pointings.

The observations pointed at the region surrounding Saturn during 4 nights between the 2nd and the 5th of July, 2019. Two different pointings were used every night to account for Saturn's motion These two areas are referred as *"Field 1"* and *"Field 2"*. These fields were designed to image as many satellites as possible while keeping Saturn off the field. These change every night to account for parallax and targets falling in between ccds. The bright planet's proximity imposed important background gradients in our images. Additionally, Saturn was in the vicinity of the galactic plane, increasing the chance of the targets to be observed near field stars. A careful data reduction was fairly successful in accounting for these features (see section 4.3.1)

Most SIrrs are too faint to be detected in a single exposure without trailing, so many short exposures were taken to be "integrated" later, accounting for the target's sky motion (more details of this "stacking" process in section 4.3.3). The fields were imaged in g, r and i bands with 120 second exposures to prevent trailing. A handful of short exposures (15 and 30 seconds) in g, r, i and z bands where also taken every night. Table 4.1 shows the detailed observational plan.

[1] `https://noirlab.edu/public/programs/ctio/`

Since the goal was to detect irregular satellites brighter than $r \sim 25$ on each filter each night, and taking into account that they are known to be red bodies, the survey was designed to observe them $\gtrsim$1 hour in r and i and $\gtrsim$2 hours in g. As seen in Table 4.1, the observations were divided in single filter blocks. Both fields were observed in r and i, but constrained by the night's duration, we could observed only one field in g (causing that each field was observed only 2 nights in g). Short observations were designed to take gri bands in between blocks.

4.2.2 Satellites' Localization

Locating known SIrrs was done using the ephemeris provided by the Jet Propulsion Laboratory (JPL) web service[2], obtained via `astroquery`[3] (Ginsburg et al., 2019), which is a coordinated package of `astropy`[4] (Astropy Collaboration et al., 2013, 2018), both packages built in `Python`[5]. It was observed that the bodies' phase angle, the heliocentric distance and the geocentric distance barely change through the four nights, as shown in Table 4.2.

Because of their brightness it as possible to detect Hyperion and Phoebe in the short exposure images (Hyperion and Iapetus were the two regular satellites visible, but the latter was saturated). For all other SIrss, "stacked" magnitudes were measured (see section 4.3.3).

4.3 Image Analysis

4.3.1 Image Processing

All image processing was done using the methods implemented in `photutils`[6] (Bradley et al., 2020), which is an affiliated package of `astropy`. First, I computed the images' two-dimensional "background" and its root mean square (called for now on "background-RMS" or just "RMS")[7]. Both "background" and "background-RMS" are calculated and used in a similar way to `SExtractor`[8] (Bertin & Arnouts, 1996), separating the image in a grid of cells, estimating the mode[9] (as the background) and the standard deviation (as the root mean square) on each cell to form a "low resolution map" of both "background" and "background-rms". A median filter is performed in both "low resolution maps" to finally interpolate them to the size of the original image (using spline interpolation of order 3). Using visual inspection, I explored the resulting backgrounds trying different sizes for cells (30-300 pixels) and median filters (1-11 pixels). A cell size of 62x62 pixels was chosen, which is small enough to distinguish between the background from the many stars that occupy these crowded fields and to account for the diversity of background gradients and patterns caused by the proximity of Saturn.

[2] JPL Horizons: `https://ssd.jpl.nasa.gov/horizons/`

[3] `https://astroquery.readthedocs.io/en/latest/`

[4] `https://www.astropy.org/`

[5] `https://www.python.org/`

[6] `https://photutils.readthedocs.io/en/stable/`

[7] Using `Photutils`' function `Background2D`

[8] `https://www.astromatic.net/software/sextractor/` `https://sextractor.readthedocs.io/`

[9] The mode estimator is equal to $2.5\text{median} - 1.5\text{mean}$ (or the median if $(\text{mean} - \text{median})/\text{std} > 0.3$) where the median, mean and standard deviation (std) are calculated over the "sigma-clipped" pixels (rejecting values farther than 3 standard deviations from the median) for each cell in the grid.

Table 4.1: Survey Chronology

Night[a]	Field[b]	R.A.[c]	Decl.[c]	Filter[d]	Exp. Time[e]	N[f]	Start[g]
1	1	19h11m13s	287d48m14s	*griz**	15	1	2019-07-03 01:09:46
				r	120	35	2019-07-03 02:41:01
				i	120	34	2019-07-03 04:09:36
	2	19h19m26s	289d51m27s	*griz**	15	1	2019-07-03 04:12:05
				i	120	35	2019-07-03 05:39:58
				r	120	35	2019-07-03 07:08:39
	1	19h11m13s	287d48m14s	*griz**	15	1	2019-07-03 07:11:07
				g	120	60	2019-07-03 09:41:44
				*griz**	15	1	2019-07-03 09:44:13
				g	120	10	2019-07-03 10:09:20
2	2	19h19m09s	289d47m20s	*griz**	30	1	2019-07-04 01:01:28
				r	120	35	2019-07-04 02:32:40
				i	120	35	2019-07-04 04:03:15
	1	19h10m52s	287d42m54s	*griz**	30	1	2019-07-04 04:05:45
				r	120	35	2019-07-04 05:39:53
				i	120	32	2019-07-04 07:09:05
	2	19h19m09s	289d47m20s	*griz**	30	1	2019-07-04 07:11:33
				g	120	30	2019-07-04 08:30:48
				*griz**	30	1	2019-07-04 08:33:16
				g	120	30	2019-07-04 09:53:00
3	1	19h09m51s	287d27m52s	*griz**	30	1	2019-07-04 09:55:29
				r	120	35	2019-07-05 02:35:19
				i	120	35	2019-07-05 04:04:59
	2	19h18m56s	289d44m04s	*griz**	30	1	2019-07-05 04:08:48
				r	120	35	2019-07-05 05:42:44
				i	120	34	2019-07-05 07:13:36
	1	19h09m51s	287d27m52s	*griz**	30	1	2019-07-05 07:16:04
				g	120	53	2019-07-05 09:34:08
4	2	19h18m37s	289d39m15s	*griz**	30	1	2019-07-05 09:36:36
				r	120	30	2019-07-06 02:20:30
				i	120	30	2019-07-06 03:41:06
	1	19h09m31s	287d22m49s	*griz**	30	1	2019-07-06 03:43:33
				r	120	30	2019-07-06 05:11:08
				i	120	30	2019-07-06 06:26:54
	2	19h18m37s	289d39m15s	*gri**	30	1	2019-07-06 06:29:22
				g	120	60	2019-07-06 09:05:11
				*gri**	30	1	2019-07-06 09:07:40
				g	120	11	2019-07-06 09:37:31

[a] Number of the night.

[b] Number of the Field (1 or 2).

[c] Central coordinates of the field observed (note that they change each night).

[d] Filter used in the observations.

[e] Duration of a single exposure (in seconds).

[f] Number of observations taken on the specified filter.

[g] Time when the observations started (in UTC).

* When exposures are short (15 or 30 seconds), one exposure on each filter was taken consecutively.

Table 4.2: Observation Geometry

	Param.[a]	mean	min.	max.
All[b]	α	0.527	0.232	0.818
	r	10.067	9.889	10.271
	Δ	9.054	8.874	9.261
Saturn[c]	α	0.529	0.352	0.698
	r	10.050	10.050	10.050
	Δ	9.037	9.035	9.040
Satellites[d]	α		0.339	0.351
	r		0.000	0.010
	Δ		0.001	0.014

Notes

[a] Orbital Parameters: Phase (Sun-Object-Earth) angle (α, in degrees), heliocentric distance (r in au) and geocentric distance (Δ, in au).

[b] Values for all bodies (Saturn and its satellites) at observed times.

[c] Values for Saturn at observed times.

[d] Minimum and maximum **variation** of each parameter for each satellite at observed times.

Yet, this cell size tends to overestimate the background near bright stars. To compensate for that effect, the size of the median filter for the "low resolution map" was set to 9 pixels (instead of 3, which is the size the algorithm recommends by default). This led to to underestimate the fluxes of bright stars ($r \leq 15.5$) but it did not affect the result for most sources. Once the background and the background-rms were calculated, it was possible to do photometry to the static sources in the background-subtracted images, using the uncertainties obtained from the background and the background-rms as weight maps (as explained in section 4.3.2).

Prior to doing photometry on SIrrs (which are transient sources with the risk of falling on top or nearby stars) I visually inspected around their expected positions and check for contamination by nearby sources. A "Sky" image was constructed for each CCD with all transient objects (like asteroids and satellites) removed. This "Sky" with only static sources is then subtracted from each image, allowing to further clean the images from most of the contribution of sources nearby the satellites. I begun by taking the background-subtracted images and moved them to a common frame (corresponding to the image closest to the mean coordinate of those taken in the same night and the same band) using "spline interpolation". To move an image to match the frame of another it was considered the rotation and translation that best matched representative positions between their WCS[10] as computed by the DECam repository. The Sky was produced as the median (in each pixel) of all interpolated images. Simply using the images median works fine for all satellites but the brightest, for which a trail of their trajectory is left. Using Phoebe as reference (the SIrr that leaves the brightest trail) I realize that excluding the 20 pixels closest to the Irr on each image was

[10] "World Coordinate System", transforming from pixel values to "sky" coordinates (namely, right ascension α and declination δ) or vice versa. For this it was used `astropy.wcs`.

enough to get rid of that trail. Another way of doing the same was implementing a "sigma-clipping" process through each pixel to reject outlier values (when a satellite or other moving object is crossing that pixel). I selected which technique worked best for each satellite by visually inspecting the final result. The satellites that left a trail in the Sky image and required this processing were Phoebe, Albiorix, Siarnaq, Paaliaq, Ymir and Kiviuq. Finally, we simply subtract the Sky from each single exposure image.

4.3.2 Photometry

In order to find a transformation for the Irrs' fluxes to magnitudes, first a forced photometry on known sources was performed. This photometry consists in fitting a two-dimensional Gaussian profile on the stamp of the source (a small piece of the background subtracted image centered at the source). This Gaussian profile is defined in equation 4.1, where $f(x, y)$ is the fitted flux at the pixel coordinate (x, y) of the stamp and the total flux is $2\pi F_0 \sigma_x \sigma_y$.

$$f(x,y) = F_0 \exp\left(-\frac{(x-x_0)^2}{2\sigma_x^2} - \frac{(y-y_0)^2}{2\sigma_y^2}\right) \tag{4.1}$$

The inverse square of an "error-map" in that stamp was used as the weights of the fitting process. This error-map, similarly to the one computed by `SExtractor`, accounts for the background error (the RMS) and the Poisson error in each pixel[11]. To fit these Gaussian profiles to the sources the Levenberg-Marquardt algorithm[12] was used (Levenberg, 1944; Marquardt, 1963). Considering that the images have FWHM between 3 and 9 pixels, as reported by the DECam repository, the results we tested using stamps of 19x19 and 11x11 pixels, giving both similarly good results (reflected by our errors when calculating the magnitudes, as explained in section 4.3.4). Since most of our fields are relatively crowded, we chose 11x11pix stamps to reduce contamination from nearby sources.

First, `SExtractor` was used to detect the sources on the original images, configured to calculate the background and its RMS as described in section 4.3.1 and to detect sources with brightness of al least twice the RMS. `SExtractor` was chosen due to its ability to deblend sources and to judge their probability of being stars[13]. `SExtractor` is able to do all of this rapidly and with low computational cost. To fit the profiles of these sources, only those that are farther than 150 pixels away from CCD edges were used (avoiding "empty" pixels left over from shifting images to a common frame, as explained at the end of section 4.3.1), that have positive fluxes and a probability of being stars higher than 0.7, as computed by `SExtractor` (since sources that did not satisfy that requirement were found to be extended, blended or spurious).

Having fit all sources, the "sigma" that characterized the width of the profile of all sources (σ from equation 4.1) was calculated. To do that, only sources that are at least 11 pixels

[11] Implemented with the `calc_total_error` function of `photutils`, where the error in each pixes is equal to $\sqrt{\sigma_{bkg}^2 + F/g_{eff}}$, with σ_{bkg}^2 and F the RMS and the flux in that pixel and g_{eff} the effective gain (namely, the number of electrons per flux count).

[12] Implemented with the `LevMarLSQFitter` method of `astropy`.

[13] The old `SExtractor`'s neural network classifier was used, which gives a probability of being a star (in contrast of being a galaxy). For this it requires the seeing of the image, which we provided using the FWHM reported in the DECam repository images.

away from the closest source were select. Then all sources too bright or faint were rejected (clipping at 2-sigma in brightness) to then reject all sources with a standard deviation in the fitted residual (the stamp minus the fitted profile) larger than twice the median RMS in that stamp. Finally, with the remaining sources, the "sigma" of the profile was calculated as the mean between $\overline{\sigma_x}$ and $\overline{\sigma_y}$ (the median of the individual profile "sigmas" in the CCD's x and y coordinates respectively, after performing a final "sigma-clipping" over the profile's "sigma"). All the rejections above were aimed to remove any artifact, blended, saturated, and poorly fit source. Once having the characteristic "sigma" across each CCD, the sources were re-fit with a fixed point spread function to get the fluxes reported in this work. This is done independently for each epoch and CCD, delivering all the information necessary to transform the SIrrs fluxes to magnitudes (see section 4.3.4).

It is worth to mention that several methods were tried before settling on the one above. I started by using the aperture photometry from `SExtractor`, but the high background variability created very noisy detections. Then I used the `photutils` version of `DAOPHOT` (Stetson, 1987), but its method to fit overlapping sources simultaneously produced very inaccurate results and took a long time to execute. Finally I implemented the algorithm explained above, which uses a simple PSF model that does not need to detect sources (since we only use known sources detected by `SExtractor`) nor fit several sources simultaneously (since we focus in isolated bodies).

4.3.3 Stacked Images

To determine the colors of Saturn satellites is necessary to "stack" the images (namely, integrate a series of images to increase the signal-to-noise ration of the target source until it is detectable, as in Gladman et al. 1998; Holman et al. 2004; Kavelaars et al. 2004; Fuentes et al. 2009) to account for most of them being too faint to be detected in single exposure images. Sky-subtracted stamps of 11x11 pixels centered on the expected satellites' positions were considered to stack them. For each night and band a different stack was produced. The main difference between this method and the one presented in Gladman et al. (1998) is that the former does not scale the fluxes of the images to equalize them to a reference, not to create the Sky image nor for the stack. Instead, it uses visual inspection on each single exposure stamp to ensure only stamps not contaminated by bright stars halos or other features, such as cosmic rays or detector artifacts, are included in the stack. The advantages of not scaling fluxes are that it does not add uncertainty to the observations (such as from imperfect scaling factors or PSF-matching) and it does not increase the noise contribution of certain images, in particular those that suffer more extinction and are usually noisier.

The source's flux on each stacked stamp was measure as explained in section 4.3.2. A two-dimensional Gaussian profile is fitted, but this time the pixels are weighted using the inverse square of the standard deviation calculated in the vicinity of the source. Previously to fit the Gaussian profile of the satellite is necessary to have the "sigma" of the profile of a stacked source, so all images that contribute to the satellite's stacked stamp are also stacked but without removing the Sky to finally get that "sigma" from the stacked stars, using the same technique explained in section 4.3.2 (namely, fitting individually the "sigma" of the profiles of the sources detected using `SExtractor` and getting the general "sigma" as the median of the individual values after removing outliers). Finally, all measurements with low

(<3) signal-to-noise are rejected, calculated as the amplitude of the fitted Gaussian profile divided by the root mean square of the residual stamp. (the stamp minus the fitted profile).

4.3.4 Obtaining Magnitudes

Once all fluxes were obtained (see section 4.3.2), their transformation to magnitudes was computed. The PanSTARRS photometry was used as reference (Chambers et al., 2016). All stars from PanSTARRS on the CCDs that contain our target satellites[14] were matched to our sources (using their sky coordinates, right ascension α and declination δ). Only stars closer than $1''$ to each source were considered (since the cross-match distances were mostly on that range). PanSTARRS provide "Mean" and "Stack" photometries (computed over single exposure images and stacked images respectively), having "PSF" and "Aperture" magnitudes in both cases. We used the "Mean PSF" photometry (and astrometry) since it showed more proximity with our data (consistent with the photometry and astrometry performance shown in Chambers et al. 2016). To improve the photometry I used a similar subset of stars as the ones used to obtained the "sigma" of our sources' profile, namely, stars farther than 150 pixels from the CCD borders and at $5''$ (around 20 pixels) farther from the closest source. Then, I also rejected sources with PanSTARRS magnitudes ("`*MeanPSFMag`") brighter than 16 (which were typically saturated), and magnitude uncertainties ("`*MeanPSFMagErr`") and standard deviations ("`*MeanPSFMagStd`") above 0.05 and 0.1 respectively.

Equation 4.2 was used to transform fluxes to magnitudes, where n and t are the identifier of the source and the time they were observed. For each CCD and time it was calculated $m^0 = 2.5\log_{10}(Q)$, where Q is the "sigma-clipped" mean of $F_{n,t}/F_n$, with $F_{n,t}$ the measured flux of the source n at time t and F_n the flux of that source according to PanSTARRS (namely, $F_n = 10^{-0.4 m_{PS1,n}}$, with m_{PS1} equal to "`*MeanPSFMag`"). This gives one m^0 for all sources in one CCD at one time. Having $m_{n,t}$, $F_{n,t}$ and $m^0_{n,t}$ known for all selected PanSTARRS sources (with $m_{n,t} = m_{PS1,n}$), the parameters A were obtained by solving equation 4.2 in matrix form including all values of known PanSTARRS sources (where $(g-r)_n$, $(r-\mathrm{i})_n$ and $(r-\mathrm{i})_n$ are the colors of the source n and $X_{n,t}$ is equal to the airmass proxy $\sec(z_{n,t})$ with z the zenith angle of the source at time t). Here A_3, A_4 and A_5 account for color corrections, A_1 for the airmass extinction and A_2 accounts for a general extinction that affects all sources at a given time. All A parameters are calculated (and used) separately for each night, band and field.

$$\begin{aligned} m_{n,t} = &- 2.5\log_{10}(F_{n,t}) + m^0_{n,t} + X_{n,t}A_1 + A_{2,t} \\ &+ A_3(g-r)_n + A_4(g-\mathrm{i})_n + A_5(r-\mathrm{i})_n \end{aligned} \tag{4.2}$$

Given the nature of this work, I was interested in doing photometry in stacked sources. Since a stacked flux $\langle F \rangle$ is computed on the mean of a series of stamps ($\mathrm{i} = 1, ..., N$), it is observed that $\langle F \rangle = \frac{1}{N}\sum F_\mathrm{i}$, where $F_\mathrm{i} = 10^{-0.4(m-f_\mathrm{i})}$ (obtained by expressing equation 4.2 as $m = -2.5\log_{10} F_\mathrm{i} + f_\mathrm{i}$). This yields equation 4.3, which gives the magnitude corresponding to the stacked source (using all the m^0_i and A parameters obtained when solving equation 4.2 to calculate f_i).

[14] Obtained via `astroquery.mast`, querying for Data Release 2 values

$$\langle m \rangle = -2.5 \log_{10} \langle F \rangle + \langle m \rangle_0$$
$$\langle m \rangle_0 = 2.5 \log_{10} \left(\frac{\sum_{\mathrm{i}}^{N} 10^{0.4 f_{\mathrm{i}}}}{N} \right) \tag{4.3}$$

For each exposure i two sources of error can be considered, one from the measured flux and other from the standard deviation of the errors of the known sources when solving equation 4.2. The later is taken as the error of f_{i} (namely, $\sigma_{f_{\mathrm{i}}}$). Propagating those errors to obtain $\sigma_{\langle m \rangle_0}$ (the error of $\langle m \rangle_0$) using a Taylor's expansion yield equation 4.4. However, this underestimates $\sigma_{\langle m \rangle_0}$ for each SIrr so we report the root mean square of the errors on the stacked known sources instead.

$$\sigma^2_{\langle m \rangle_0} = \frac{\sum_{\mathrm{i}}^{N} \left(\sigma_{f_{\mathrm{i}}} 10^{0.4 f_{\mathrm{i}}} \right)}{\left(\sum_{\mathrm{i}}^{N} 10^{0.4 f_{\mathrm{i}}} \right)^2} \tag{4.4}$$

To get f_{i} in each case is necessary to know the source's colors, which are unknown at the beginning. An iterative procedure is used assuming no color correction at first and then using the resulting magnitudes in each band to start correcting the colors until the magnitudes vary less than $\sigma_{f_{\mathrm{i}}}/2$.

4.4 Results

From the short exposure images it was measured Hyperion (the only regular satellite observed that was not saturated) and Phoebe (the brightest SIrr). Since these observations visited one field using each band consecutively, their magnitudes were derived assuming one set of colors per visit (remember that, as explained in section 4.3.4 the magnitudes needed to be refine by iterating) The result is shown in Table 4.3. Note that there are observations in z band, since color terms relative to that band when solving equation 4.2 were also included.

Magnitudes and colors from stacked sources are also reported. In the case of stacked images, the average between stacked measurements was calculated in order to obtain an equivalent to the mean magnitude through the different SIrr's rotational phases. The colors reported in table 4.4 (and used when solving equation 4.2) were obtained using those mean magnitudes. These colors are shown in Figure 4.1, with Hyrrokkin and Kari in red, since their colors are reported for the first time in this work. In Appendix Annexed C are listed all magnitudes used to compute these colors.

4.5 Discussion

In this work are reported $r - \mathrm{i}$ colors for 21 Saturn Irregular satellites (16 of them with $g - r$ colors). Four of them were measured for the first time (Skoll, Hyrrokkin, Kari and Loge). In Figure 4.2 are shown the result from comparing these colors with those from other works.

Table 4.3: Magnitudes and Colors of Hyperion and Phoebe

Name	Night	UTC[a]	r	$g-r$	$r-\mathrm{i}$	$\mathrm{i}-z$
Hyperion	2	2019-07-04 01:04:17.760	14.25 ± 0.03	0.51 ± 0.05	0.23 ± 0.04	0.01 ± 0.05
		2019-07-04 04:07:41.664	14.32 ± 0.03	0.48 ± 0.05	0.17 ± 0.04	0.05 ± 0.05
		2019-07-04 07:13:29.856	14.26 ± 0.03	0.51 ± 0.05	0.16 ± 0.04	0.08 ± 0.05
		2019-07-04 08:35:11.328	14.26 ± 0.03	0.53 ± 0.05	0.16 ± 0.04	0.04 ± 0.05
		2019-07-04 09:57:28.224	14.28 ± 0.03	0.42 ± 0.05	0.15 ± 0.04	0.16 ± 0.05
	4	2019-07-06 03:45:31.104	14.07 ± 0.03	0.47 ± 0.04	0.22 ± 0.04	0.07 ± 0.04
Phoebe	1	2019-07-03 04:13:30.720	16.52 ± 0.03	0.34 ± 0.04	0.13 ± 0.04	-0.02 ± 0.04
		2019-07-03 09:45:38.880	16.39 ± 0.03	0.36 ± 0.04	0.14 ± 0.04	-0.06 ± 0.04
	3	2019-07-05 01:05:13.056	16.47 ± 0.02	0.37 ± 0.03	0.11 ± 0.03	-0.02 ± 0.03
		2019-07-05 04:10:48.288	16.49 ± 0.02	0.34 ± 0.03	0.14 ± 0.03	-0.04 ± 0.03
		2019-07-05 07:19:31.008	16.34 ± 0.02	0.33 ± 0.03	0.14 ± 0.03	-0.04 ± 0.03
		2019-07-05 09:38:33.792	16.44 ± 0.02	0.36 ± 0.03	0.11 ± 0.03	-0.01 ± 0.03

Notes

[a] Start of the r band observation.

Table 4.4: Satellites magnitudes and colors

Name	r^a	$g-r^b$	$r-\mathrm{i}^b$
Phoebe	16.49 ± 0.06	0.27 ± 0.07	0.06 ± 0.08
Siarnaq	20.47 ± 0.05	0.53 ± 0.07	0.24 ± 0.09
Albiorix	21.07 ± 0.09	0.46 ± 0.10	0.31 ± 0.11
Ymir	22.25 ± 0.11	0.50 ± 0.12	0.25 ± 0.14
Tarvos	22.88 ± 0.05	0.52 ± 0.07	0.30 ± 0.07
Kiviuq	22.49 ± 0.06	0.51 ± 0.07	0.28 ± 0.09
Paaliaq	21.51 ± 0.04		0.25 ± 0.05
Ijiraq	23.18 ± 0.05	0.70 ± 0.05	0.20 ± 0.06
Skathi	24.26 ± 0.04	0.24 ± 0.06	-0.005 ± 0.093
Bebhionn	24.66 ± 0.05		0.24 ± 0.09
Erriapus	23.69 ± 0.05	0.20 ± 0.09	0.42 ± 0.08
Skoll	25.02 ± 0.05		0.36 ± 0.08
Hyrrokkin	24.08 ± 0.06	0.50 ± 0.08	0.34 ± 0.09
Mundilfari	24.36 ± 0.05	0.38 ± 0.06	0.03 ± 0.08
Narvi	24.48 ± 0.06	0.24 ± 0.07	0.42 ± 0.09
Suttungr	24.32 ± 0.06	0.40 ± 0.07	0.17 ± 0.08
Bestla	24.64 ± 0.04	0.72 ± 0.07	0.38 ± 0.07
Thrymr	24.08 ± 0.05	0.40 ± 0.06	0.15 ± 0.08
Kari	24.65 ± 0.06	0.31 ± 0.07	0.53 ± 0.09
Loge	24.80 ± 0.05		0.15 ± 0.08
Fornjot	24.93 ± 0.06		0.20 ± 0.09

Notes

[a] Magnitude mean observed each night.

[b] Colors obtained from the mean magnitudes observed each night.

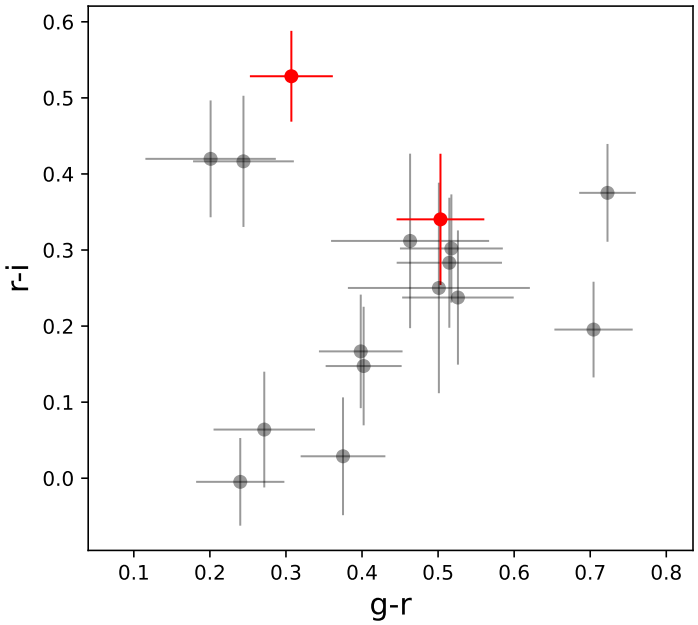

Figure 4.1: Color-color plot for values from table 4.4. In red are Hyrrokkin and Kari, bodies whose colors had never been measure before (note that Skoll and Loge had not been measured before either, but they were measure in r and i only). The error bars were obtained by propagating the individual errors when computing the mean magnitudes and the colors.

Notice that all results are reported in the BVR bands, with the exception of Buratti et al. (2005) which does so in gri filters. To transform BVR to gri it was used the equations from Jester et al. (2005). Is notorious a high dispersion between our results and those of other works.

The main problem with these measurements is the "time blocks" system chosen to observe in different bands (see section 4.2.1), with each of the stacked measurements on each band made in different parts of the SIrrs rotational phases. All observations on each filter are averaged to get a proxy of the mean magnitude through the SIrr' rotations. Sadly, this does not guarantee that any important part of the SIrrs' phase curve is not missed. Denk & Mottola (2019) show the lightcurves of many SIrrs at different solar phase angles, showing that these bodies can vary their brightness as much as half a magnitude at low solar phase angle. Although the observation presented here were made solar phase angles of $\sim$0.5°, much lower than in Denk & Mottola (2019), the variations showed in that work at low phase angles are similar to other brightness variations observed in ground facilities, as seen in Bauer et al. (2004) and Buratti et al. (2005) for Phoebe and Siarnaq[15] respectively. In Chapter 3 I explore the color deviations derived from measuring minor bodies at different faces of their rotations. In the worst case scenario (and assuming constant colors through the SIrrs rotations), that variation is the possible error for the color if observed at opposite peaks of the rotational curve. In these case I can not have observations exactly at opposite peaks since observations are stacked in time ranges of a couple of hours, which "smooths out" magnitudes variations. Besides of that, most of the detected SIrrs have averaged four stacked measurements in r and i bands that are likely to span different parts of the SIrrs, which should also decrease

[15]In Buratti et al. (2005) where "S/2000 S3" is referred to as Tarvos instead of Siarnaq

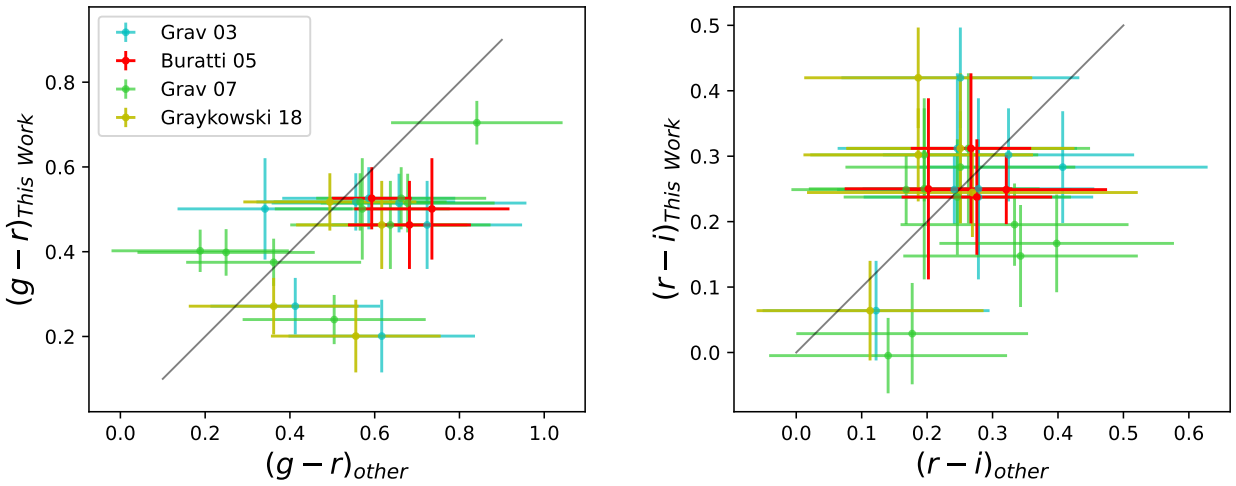

Figure 4.2: Our colors compared to colors from other works. In light blue, colors from Grav et al. (2003), in red from Buratti et al. (2005), in green from Grav & Bauer (2007) and in yellow from Graykowski & Jewitt (2018). In black is the one-to-one line.

the color error from the "worst case scenario" of ∼0.5 to this work's error, which is around 0.2 or 0.3, as seen in Figure 4.2, where although the difference between observations is high, the "error zero" line (in black) pass through most of the error ranges. The situation is a bit worse for the $g-r$ colors where the difference between observations gets higher, which can be explained by the less number of "time blocks" in g that makes more likely to miss important part of the rotational phase in that band, making our magnitudes more likely to deviate from their actual mean. A good example of this is Phoebe, for which there are stacked colors (from table 4.4) and "instantaneous" colors (from table 4.3), where it is possible to see that the stacked colors are barely within the errors of the instantaneous measurements (which should be considered as the "actual" colors of those sources). Another source of error can be color variations. In the analysis above we assumed that the colors are constant, but in table 4.3 is possible to see that they can vary as much as 0.36 (in the case of Hyperion in $g-r$). This color variations could also explain the dispersion in measurements in Figure 4.2. These sources of uncertainty do not only affect the stacked measurements, but also previous surveys, as is shown in Figure 4.3, where there is a comparison between past works against Grav & Bauer (2007) (BVR colors are shown for Buratti et al. 2005 using the equations from Jester et al. 2005). A better observational plan to observe SIrrs (or any other Irr) would be to measure consecutively in each filter (for example, in a *ggr*i order) to get observations spanning the same rotational phases. Stacking those observations would increase the signal-to-noise ratio (reducing the errors from observing these faint sources with only one exposure) while enabling a better approximation to a "mean color" of the Irrs (at least at the observed rotational phases). Regardless all the color uncertainties already discussed, from Figure 4.2 it can be seen that the SIrrs colors reported here as a whole are consistent with those from past works.

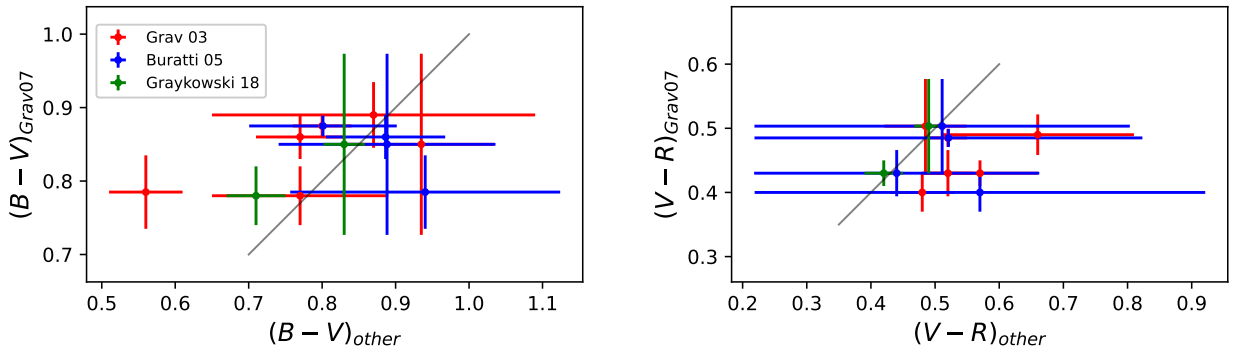

Figure 4.3: Same as Figure 4.2 but comparing data from Grav & Bauer (2007) (which contains the greatest number of SIrrs colors in past works) against Grav et al. (2003) (in red), Buratti et al. (2005) (in blue) and Graykowski & Jewitt (2018) (in green).

Chapter 5

Summary and Conclusions

5.1 About Minor Bodies in Synoptic Surveys

In chapters 2 and 3 I report on the search for asteroids and other Solar System populations imaged by HiTS, which covers more that 120 deg^2 in two diferent campaigns looking for time variable phenomena, in particular Supernovae. There was found more than 9,000 minor bodies with orbital parameters well constrained, identifying 25 NEOs, more than 8,000 Main Belt asteroids (around 2,900 previously known) and 23 TNOs.

These results serve as a good model for the ability of future surveys with multiple science drives (like LSST LSST Science Collaboration et al. 2009; Jones et al. 2016) to discover Solar System minor bodies and some of the science products that they can be produced.

One key element for these results was the machine learning classification algorithm (Cabrera-Vives et al., 2017; Martínez-Palomera et al., 2018) that allowed to select sources with a high probability of being asteroids. This classification process not only reduces the execution time, but also reduces false discoveries and the number of trajectories contaminated with incorrect detections. This "track confusion" (as called in chapters 2 and 3) increases the errors in orbital parameters and is an important problem when trying link asteroids' observations through multiple nights.

The necessity for this kind of classification algorithms to classify sources can be seen in the great effort that resulted in the construction of the Automatic Learning for the Rapid Classification of Events (ALeRCE[1]) broker (Förster et al., 2021), an astronomical broker for the rapid classification of multiple types of detections coming from large surveys such as ZTF (Bellm et al., 2019) and LSST in the future[2]. Since the classification algorithm used in this Thesis is not tailored for moving objects, future work would be needed in describing these, and other kind sources such as asteroid binaries, comets, etc, that deviate from a point source. For these algorithms to work they need to be trained in real (or well simulated) data of the objects they will classify. Considering the great number of data expected from LSST, actual

[1] `http://alerce.science/`

[2] As it can be seen in `https://www.lsst.org/scientists/alert-brokers`

detections of known moving objects can be use as training data. Recognizing those known bodies rapidly and accurately is a problem by itself. Astronomers generally rely on online or third party recognition algorithms, but in the time frame of this Thesis I also developed an open `Python` package that delivers accurate and precise ephemerides of minor bodies rapidly (see Appendix Annexed D). For each detection ALeRCE provides its probability of being an asteroid (or other type of body, such as Super Novae, bogus, etc., Carrasco-Davis et al. 2021), which is key to improve the accuracy of any linking algorithm and reduce track confusion.

To study minor bodies is important to compute their orbital parameters, which allows to study their sizes, their dynamics, recognize what kind of body they are and to perform following. It can seen in chapters 2 and 3 that to obtain moderately accurate orbital parameters, asteroids need to be observed for at least two days. If an asteroid is observed several times in consecutive days, a simple linking algorithm that joins observations trough nights if their projected positions in an intermediate time are close is enough to extend observe trajectiories between nights (Chapter 2), but if the observations are sparse, as in Chapter 3, that simple technique fails to link many bodies, especially those with "complex" observed trajectories as those shown in Figure 3.2. I designed an algorithm in Chapter 3 to link detected asteroids in single nights by moving the coordinate frame from the observer's to the Sun's, allowing to better extend observations through many nights and improving their computed orbital parameters.

Finally, as wide-field surveys get deeper, understanding how to detect and characterize them, as with the techniques elaborated for this Thesis, will allow to increase our knowledge of already known bodies and to extend this knowledge to new faint bodies that will be discover by LSST and any other survey to come.

5.2 About Asteroids' Sizes and Colors

In order to study the size distribution of the MB, in Chapter 3 their absolute magnitude H is used as a proxy of the size. Assuming a constant albedo of 0.1, our measured H_g span from 14 to 18, which translates to bodies of sizes between 1 to 10 km. Is found that the size distribution for asteroids from HiTS 2014 is consistent with a Double Power Law with slopes consistent with those found in Ivezić et al. (2001) (which is the study with the highest number of asteroids analyzed). It is also consistent with the slope at the faint end found in Gladman et al. (2009) (which shows asteroids observed in a survey with similar characteristics as HiTS). On the other hand, the MB size distribution obtained from HiTS 2015 is compatible with a SPL for the entire population as well as for the Inner, Intermediate and Outer MB separately. On any of these populations it exhibits steeper slope parameters than those reported in previous surveys, only comparable with values found by Parker et al. (2008) at the bright end of the distribution. As discussed in Chapter 3, these steep slopes are likely to be caused by the latitudinal distribution of HiTS 2015 observations around the ecliptic. While HiTS 2014 observed very near the ecliptic, yielding results similar to those from other surveys dominated by asteroids near the ecliptic, data from HiTS 2015 was obtained farther from the ecliptic, finding an inferior fraction of bright (bigger) bodies (since bigger asteroids are less numerous they are harder to observe far from the ecliptic where they scarce). A similar result was found by Bhattacharya et al. (2010), where bodies at latitude $\sim 5^\circ$ have fluxes 30% fainter than those at latitude $\sim 0^\circ$.

The luminosity functions of MB bodies obtained in Chapter 3 (Figures 3.7 and 3.12) are well fitted by a Double Power Law, as observed in Gladman et al. (2009). Comparing both luminosity functions it can see that, although in both cases there is a clear break around $g \sim 20.5$, slopes at both sides of the break are very different between the asteroids observed in the 2014 and 2015 HiTS campaigns. While for 2014 the slopes are consistent with those obtained by Gladman et al. (2009), in 2015 they are much steeper. The great similarity between the luminosity function observed in HiTS 2014 and that from Gladman et al. (2009), as it can be seen in Figure 3.12, in contrast with the one obtained from HiTS 2015, reinforce the hypothesis that the steeper slopes are due the observational bias of observing at higher latitudes (which is the main difference between 2014 and 2015 campaigns relative to the populations they can observe).

The colors of MB bodies reported in Chapter 3 are similar to S-type bodies and it can be seen that they become redder with semi-major axis (as seen in Figure 3.11). This is consistent with the scenario of the Outer MB (the most populous region of the MB, as it can be seen in Figure 3.6a) is dominated by S-type asteroids. Those colors can only be analyzed as a whole, since individually they are greatly affected by magnitude variations caused by the bodies rotations during the observations in different bands, which completely hides the color bimodality observed in other surveys such as Ivezić et al. (2001). It was found that, in order to be able to distinguish the color bimodality among asteroids, is necessary that the observations in different bands are not taken more than 14 minutes apart. This is an important constraint for future surveys, such as LSST, that plans to visit one sky field twice a night, taking two images per visit (Ivezić et al., 2019). Since visits can be a few hours apart, ideally the two images per visit should be in different filters to retrieve good colors. Although LSST will deliver large light-curves for many asteroids allowing to measure colors even if the two images per visit were in the same filter, this will be possible only for asteroids well tracked through many nights for a long time, while if the color is measured per visit we would be able to have colors for nightly tracklets even for those cases when the body is detected only once (generally the case for small bodies at the limiting magnitude).

Finally, it was not find any color–size dependence between $14 < H_g < 18$ ($1 < D < 10$ km), as suggested by Ivezić et al. (2001), although taking into consideration the color uncertainty discuss above, that we only have colors from HiTS 2015, which have a scarce number of asteroids with a very distinctive size distribution, and that we could not observe bodies smaller than $\sim$1 km, this result is not strong enough to reject a possible color–size relation among asteroids.

5.3 About Irregular Satellites

In Chapter 4 are reported $r - \mathrm{i}$ color measurements for 21 Saturn Irregular satellites (16 of them with $g - r$ colors), the highest number reported in one single survey for these bodies. (Graykowski & Jewitt 2018 reported colors for 13 SIrrs in $B-R$ with only 5 of them in $B-V$ and $V - R$, while Grav & Bauer 2007 reported colors for 12 SIrrs in $B - V$ and $V - R$). Colors of four of them were measured for the first time (Skoll, Hyrrokkin, Kari and Loge).

I managed to obtain these faint sources even through Saturn's brightness and only partially photometric skies by carefully accounting and removing the background brightness from the

observations before selectively stacking them and improving their signal-to-noise.

Despite known sources of uncertainty affecting the measurements, as discussed in section 4.5, these results are good enough to analyze the SIrrs' population as a whole and compare it with other populations. There is no significant difference between our results and those of previous works, as shown in Figure 4.2, where the found colors occupy the same region in color-color space. This is also true for Skoll, Hyrrokkin, Kari and Loge, bodies whose colors had not been measured before. Following the terminology used in Thirouin & Sheppard (2019), these colors can be described as "neutral" and "moderately red" (with a few near the "very red" region). Although Irrs and TNOs are expected to be related (since both would be heirs of the primordial planetesimal disk), there is an obvious lack of "ultra-red" bodies among the SIrrs in comparison to the TNOs (as it can be seen by comparing Figure 6 and 8 of Graykowski & Jewitt 2018 with Figure 2 of Jewitt 2018 in BVR bands, or, for gri colors, comparing Buratti et al. 2005 and our results with TNOs' colors from Pike et al. 2017, Terai et al. 2018 and Thirouin & Sheppard 2019). The same is true for other populations that are thought to be related to the TNOs, such as the Irrs of the other giant planets (Graykowski & Jewitt, 2018) or Jupiter and Neptunian Trojans (Jewitt, 2018; Lin et al., 2019). Jewitt (2002) shows how outgassing of volatile materials (due to solar irradiation) within short-period comets produces resurfacing of bluer inner material, arguing that this could explain how bodies originated in the Kuiper Belt would become bluer if scattered closer to the Sun. While for the cases of JIrrs, SIrrs and JTs can be argued that there are no ultra-red bodies because those that once were ultra-red got bluer due to their proximity to the Sun, as explained in Jewitt (2002, 2018), similarly to what happens to centaurs, which get bluer as their perihelion decreases (Jewitt, 2015), that does not explains neutral and moderately red colors of the other populations, as made clear by Jewitt (2018) for the case of the Trojans. Another explanation is proposed in Nesvorný et al. (2020), where is argued that current TNOs colors can be explained if there were no ultra-red material in the primordial planetesimal disk at heliocentric distances below 30 or 40 AU, indicating that current TNOs could have received their moderately red populations from scattered inner bodies when the giant planets migrated and solving why there are no ultra-red bodies among Irrs and Trojans (because there were never ultra-red bodies in their parent populations, at < 30AU from the Sun). And yet, if the latter were true, we would expect to find more "neutral" colors among the TNOs. This lack of neutral bodies for the TNOs could be explained by the continuous thermal effect of the Sun (as explained in Jewitt 2002) and by an evolutionary history marked by collisions (Nesvorný et al., 2003; Bottke et al., 2013, 2010; Wong et al., 2021; Ashton et al., 2021) that could have blued originally moderately red Irrs. Ashton et al. (2021) report a high number of small SIrrs (possibly consequence of a recent impact) evidencing a history richer in impacts than the JIrrs', which could explain the high number of "neutral" bodies among the SIrrs, population that appears as blue as the JIrrs population (as seen in Graykowski & Jewitt 2018) despite the latter is much closer to the Sun and its radiation.

Finally, I remark the importance of the stacking method presented in Chapter 4 which allows to get low photometric errors in non-photometric conditions and near a bright source (such as Saturn). By carefully removing the background brightness and selecting images where the targets are not contaminated with stars or any other apparent feature, without having to scale fluxes or matching PSF kernels between images, nor having to point at typical standard stars, but using those in the observed fields with low photometric error and low

variability. This should be taken into account for future surveys of similar populations, in particular deep stares around crowded fields as is the plan for part of the Vera Rubin Survey. The same holds for the filter cadence when planning stacking observations.

5.4 About this and future work

The understanding of the evolution of the Solar System had greatly improved the last decade with new models of planets formation, migration and dynamical instabilities. Although these models have fairly succeeded explaining the dynamical distribution of many minor bodies populations, they have not been thoroughly tested against physical properties, as colors or sizes.

In this work I present results from studying asteroids and Saturn Irregular Satellites. For asteroids I looked for their size distribution, finding similar results as past works for those bodies near the ecliptic, but finding that the observe distribution can vary greatly if you observe at higher latitudes. I also looked but did not find a color–size relation among asteroids, but is important to remark that the measured colors were greatly affected by the fact that the different bands were observed at different phases of the asteroids rotations. That lead me to constrain the maximum time between different band observations that a survey should have in order to measure colors of asteroids. In the case of the Irregular satellites I looked for evidence of ultra red matter that could link this population with TNOs, without finding any ultra red body.

In the process of finding these results I developed many techniques that can be very useful for astronomers in future work. I developed an algorithm to link asteroids through different night of observations (Chapter 3), which is very important to constrain their orbital parameters in order to being able to known their absolute brightness and to perform follow up. I wrote an open access algorithm to obtain ephemerides of minor bodies (Appendix Annexed D), which is expected to help astronomers to plan and to detect known bodies in their observations. In order to observe bodies fainter than the single exposure limiting magnitude under the effects of much brighter sources in very crowded fields, I designed a technique to clean and avoid much of the surrounding brightness contamination to obtain magnitudes of the targeted sources and hinting the best way to obtain their colors (Chapter 4). The latter, although designed for Irregular satellites should be useful to measure magnitudes and colors of other kinds of faint bodies. By the time being I expect to use this technique to obtain irregular satellites colors of the other giant planets.

Bibliography

Andrews, S. M., Huang, J., Pérez, L. M., et al. 2018, ApJL, 869, L41

Armitage, P. J. 2020, Astrophysics of Planet Formation, 2nd edn. (Cambridge University Press), doi:10.1017/9781108344227

Ashton, E., Gladman, B., & Beaudoin, M. 2021, PSJ, 2, 158

Astropy Collaboration, Robitaille, T. P., Tollerud, E. J., et al. 2013, A&A, 558, A33

Astropy Collaboration, Price-Whelan, A. M., Sipőcz, B. M., et al. 2018, AJ, 156, 123

August, T. M., & Wiegert, P. A. 2013, AJ, 145, 152

Bauer, J. M., Buratti, B. J., Simonelli, D. P., & Owen, William M., J. 2004, ApJL, 610, L57

Bauer, J. M., Grav, T., Buratti, B. J., & Hicks, M. D. 2006, Icarus, 184, 181

Bellm, E. C., Kulkarni, S. R., Graham, M. J., et al. 2019, PASP, 131, 018002

Bernstein, G., & Khushalani, B. 2000, AJ, 120, 3323

Bernstein, G. M., Trilling, D. E., Allen, R. L., et al. 2004, AJ, 128, 1364

Berthier, J., Vachier, F., Thuillot, W., et al. 2006, in Astronomical Society of the Pacific Conference Series, Vol. 351, Astronomical Data Analysis Software and Systems XV, ed. C. Gabriel, C. Arviset, D. Ponz, & S. Enrique, 367

Bertin, E., & Arnouts, S. 1996, A&AS, 117, 393

Bhattacharya, B., Noriega-Crespo, A., Penprase, B. E., et al. 2010, ApJ, 720, 114

Bohn, A. J., Benisty, M., Perraut, K., et al. 2022, A&A, 658, A183

Bottke, W. F., Nesvorný, D., Vokrouhlický, D., & Morbidelli, A. 2010, AJ, 139, 994

Bottke, W. F., Vokrouhlický, D., Nesvorný, D., & Moore, J. M. 2013, Icarus, 223, 775

Bowell, E., Hapke, B., Domingue, D., et al. 1989, in Asteroids II, ed. R. P. Binzel, T. Gehrels, & M. S. Matthews, 524–556

Bradley, L., Sipőcz, B., Robitaille, T., et al. 2020, astropy/photutils: 1.0.1, v1.0.1, Zenodo, doi:10.5281/zenodo.4049061. https://doi.org/10.5281/zenodo.4049061

Brasser, R., & Morbidelli, A. 2013, Icarus, 225, 40

Buchanan, L. E., Schwamb, M. E., Fraser, W. C., et al. 2022, PSJ, 3, 9

Buratti, B. J., Hicks, M. D., & Davies, A. 2005, Icarus, 175, 490

Cabrera-Vives, G., Reyes, I., Förster, F., Estévez, P. A., & Maureira, J.-C. 2017, ApJ, 836, 97

Carey, S. J., Noriega-Crespo, A., Mizuno, D. R., et al. 2009, PASP, 121, 76

Carrasco-Davis, R., Reyes, E., Valenzuela, C., et al. 2021, AJ, 162, 231

Chambers, J. E. 2001, Icarus, 152, 205

Chambers, K. C., Magnier, E. A., Metcalfe, N., et al. 2016, arXiv e-prints, arXiv:1612.05560

Chen, Y.-T., Lin, H.-W., Alexandersen, M., et al. 2018, PASJ, 70, S38

Dandy, C. L., Fitzsimmons, A., & Collander-Brown, S. J. 2003, Icarus, 163, 363

DeMeo, F. E., & Carry, B. 2013, Icarus, 226, 723

—. 2014, Nature, 505, 629

Denk, T., & Mottola, S. 2019, Icarus, 322, 80

DePoy, D. L., Abbott, T., Annis, J., et al. 2008, in Society of Photo-Optical Instrumentation Engineers (SPIE) Conference Series, Vol. 7014, Ground-based and Airborne Instrumentation for Astronomy II, ed. I. S. McLean & M. M. Casali, 70140E

Dohnanyi, J. S. 1969, J. Geophys. Res., 74, 2531

Everhart, E. 1985, in Astrophysics and Space Science Library, Vol. 115, IAU Colloq. 83: Dynamics of Comets: Their Origin and Evolution, ed. A. Carusi & G. B. Valsecchi, 185

Fleming, H. J., & Hamilton, D. P. 2000, Icarus, 148, 479

Folkner, W. M., Williams, J. G., Boggs, D. H., Park, R. S., & Kuchynka, P. 2014, Interplanetary Network Progress Report, 42-196, 1

Foreman-Mackey, D., Hogg, D. W., Lang, D., & Goodman, J. 2013, PASP, 125, 306

Förster, F., Maureira, J. C., San Martín, J., et al. 2016, ApJ, 832, 155

Förster, F., Moriya, T. J., Maureira, J. C., et al. 2018, Nature Astronomy, 2, 808

Förster, F., Cabrera-Vives, G., Castillo-Navarrete, E., et al. 2021, AJ, 161, 242

Fuentes, C. I., George, M. R., & Holman, M. J. 2009, ApJ, 696, 91

Fuentes, C. I., & Holman, M. J. 2008, AJ, 136, 83

Fuentes, C. I., Holman, M. J., Trilling, D. E., & Protopapas, P. 2010, ApJ, 722, 1290

Fuentes, C. I., Trilling, D. E., & Holman, M. J. 2011, ApJ, 742, 118

Fukugita, M., Ichikawa, T., Gunn, J. E., et al. 1996, AJ, 111, 1748

Ginsburg, A., Sipőcz, B. M., Brasseur, C. E., et al. 2019, AJ, 157, 98

Gladman, B., Kavelaars, J. J., Nicholson, P. D., Loredo, T. J., & Burns, J. A. 1998, AJ, 116, 2042

Gladman, B., Marsden, B. G., & Vanlaerhoven, C. 2008, in The Solar System Beyond Neptune, ed. M. A. Barucci, H. Boehnhardt, D. P. Cruikshank, A. Morbidelli, & R. Dotson, 43

Gladman, B. J., Davis, D. R., Neese, C., et al. 2009, Icarus, 202, 104

Gomes, R., Levison, H. F., Tsiganis, K., & Morbidelli, A. 2005, Nature, 435, 466

Gomes, R., & Nesvorný, D. 2016, A&A, 592, A146

Gomes, R. S. 1997, AJ, 114, 396

Gomes, R. S., Morbidelli, A., & Levison, H. F. 2004, Icarus, 170, 492

Goodman, J., & Weare, J. 2010, Communications in Applied Mathematics and Computational Science, 5, 65

Grav, T., & Bauer, J. 2007, Icarus, 191, 267

Grav, T., Bauer, J. M., Mainzer, A. K., et al. 2015, ApJ, 809, 3

Grav, T., & Holman, M. J. 2004, ApJL, 605, L141

Grav, T., Holman, M. J., & Fraser, W. C. 2004, ApJL, 613, L77

Grav, T., Holman, M. J., Gladman, B. J., & Aksnes, K. 2003, Icarus, 166, 33

Graykowski, A., & Jewitt, D. 2018, AJ, 155, 184

Holman, M. J., Payne, M. J., Blankley, P., Janssen, R., & Kuindersma, S. 2018, AJ, 156, 135

Holman, M. J., Kavelaars, J. J., Grav, T., et al. 2004, Nature, 430, 865

Ivezic, Z., Juric, M., Lupton, R. H., et al. 2010, NASA Planetary Data System, EAR

Ivezić, Ž., Tabachnik, S., Rafikov, R., et al. 2001, AJ, 122, 2749

Ivezić, Ž., Kahn, S. M., Tyson, J. A., et al. 2019, ApJ, 873, 111

Jester, S., Schneider, D. P., Richards, G. T., et al. 2005, AJ, 130, 873

Jewitt, D. 2015, AJ, 150, 201

—. 2018, AJ, 155, 56

Jewitt, D. C. 2002, AJ, 123, 1039

Jones, R. L., Jurić, M., & Ivezić, Ž. 2016, in Asteroids: New Observations, New Models, ed. S. R. Chesley, A. Morbidelli, R. Jedicke, & D. Farnocchia, Vol. 318, 282–292

Jurić, M., Ivezić, Ž., Lupton, R. H., et al. 2002, AJ, 124, 1776

Kaib, N. A., & Chambers, J. E. 2016, MNRAS, 455, 3561

Kavelaars, J. J., Holman, M. J., Grav, T., et al. 2004, Icarus, 169, 474

Kavelaars, J. J., Jones, R. L., Gladman, B. J., et al. 2009, AJ, 137, 4917

Kley, W., & Nelson, R. P. 2012, ARA&A, 50, 211

Krisciunas, K., Margon, B., & Szkody, P. 1998, PASP, 110, 1342

Kuiper, G. P. 1956, Vistas in Astronomy, 2, 1631

Kulkarni, S. R. 2013, The Astronomer's Telegram, 4807, 1

Kurtovic, N. T., Pérez, L. M., Benisty, M., et al. 2018, ApJL, 869, L44

Lamy, P., & Toth, I. 2009, Icarus, 201, 674

Law, N. M., Kulkarni, S. R., Dekany, R. G., et al. 2009, PASP, 121, 1395

Levenberg, K. 1944, Quart. Appl. Math, 2, 164

Levison, H. F., Morbidelli, A., Tsiganis, K., Nesvorný, D., & Gomes, R. 2011, AJ, 142, 152

Levison, H. F., Morbidelli, A., Van Laerhoven, C., Gomes, R., & Tsiganis, K. 2008, Icarus, 196, 258

Lin, H. W., Yoshida, F., Chen, Y. T., Ip, W. H., & Chang, C. K. 2015, Icarus, 254, 202

Lin, H. W., Chen, Y.-T., Holman, M. J., et al. 2016, AJ, 152, 147

Lin, H. W., Gerdes, D. W., Hamilton, S. J., et al. 2019, Icarus, 321, 426

Lissauer, J. J., Ragozzine, D., Fabrycky, D. C., et al. 2011, ApJS, 197, 8

LSST Science Collaboration, Abell, P. A., Allison, J., et al. 2009, arXiv e-prints, arXiv:0912.0201

Lykawka, P. S., & Horner, J. 2010, MNRAS, 405, 1375

Lykawka, P. S., & Mukai, T. 2007, Icarus, 189, 213

Mainzer, A., Bauer, J., Grav, T., et al. 2011, ApJ, 731, 53

Maris, M., Carraro, G., Melita, M., & Parisi, G. 2018, Research Notes of the American Astronomical Society, 2, 42

Marquardt, D. W. 1963, Journal of the Society for Industrial and Applied Mathematics, 11, 431

Marsset, M., Fraser, W. C., Pike, R. E., et al. 2019, AJ, 157, 94

Martínez-Palomera, J., Förster, F., Protopapas, P., et al. 2018, AJ, 156, 186

Masiero, J. R., Mainzer, A. K., Grav, T., et al. 2011, ApJ, 741, 68

Medina, G. E., Muñoz, R. R., Vivas, A. K., et al. 2017, ApJL, 845, L10

—. 2018, ApJ, 855, 43

Minton, D. A., & Malhotra, R. 2009, Nature, 457, 1109

Morbidelli, A., Brasser, R., Gomes, R., Levison, H. F., & Tsiganis, K. 2010, AJ, 140, 1391

Morbidelli, A., Levison, H. F., Tsiganis, K., & Gomes, R. 2005, Nature, 435, 462

Naylor, T. 1998, MNRAS, 296, 339

Nesvorný, D., Alvarellos, J. L. A., Dones, L., & Levison, H. F. 2003, AJ, 126, 398

Nesvorný, D., Vokrouhlický, D., & Deienno, R. 2014, ApJ, 784, 22

Nesvorný, D., Vokrouhlický, D., & Morbidelli, A. 2007, AJ, 133, 1962

Nesvorný, D., Vokrouhlický, D., Alexandersen, M., et al. 2020, AJ, 160, 46

Parker, A., Ivezić, Ž., Jurić, M., et al. 2008, Icarus, 198, 138

Peña, J., Fuentes, C., Förster, F., et al. 2018, AJ, 155, 135

—. 2020, AJ, 159, 148

Peixinho, N., Delsanti, A., & Doressoundiram, A. 2015, A&A, 577, A35

Petit, J. M., Kavelaars, J. J., Gladman, B. J., et al. 2011, AJ, 142, 131

Pike, R. E., Fraser, W. C., Schwamb, M. E., et al. 2017, AJ, 154, 101

Polishook, D., Ofek, E. O., Waszczak, A., et al. 2012, MNRAS, 421, 2094

Raymond, S. N., Izidoro, A., & Morbidelli, A. 2020, in Planetary Astrobiology, ed. V. S. Meadows, G. N. Arney, B. E. Schmidt, & D. J. Des Marais, 287

Raymond, S. N., Quinn, T., & Lunine, J. I. 2006, Icarus, 183, 265

Rebull, L. M., Padgett, D. L., McCabe, C. E., et al. 2010, ApJS, 186, 259

Rein, H., & Liu, S. F. 2012, A&A, 537, A128

Rein, H., & Spiegel, D. S. 2015, MNRAS, 446, 1424

Rettig, T. W., Walsh, K., & Consolmagno, G. 2001, Icarus, 154, 313

Ryan, E. L., Mizuno, D. R., Shenoy, S. S., et al. 2015, A&A, 578, A42

Ryan, E. L., Woodward, C. E., Dipaolo, A., et al. 2009, AJ, 137, 5134

Schechter, P., & Press, W. H. 1976, ApJ, 203, 557

Schlafly, E. F., Green, G. M., Lang, D., et al. 2018, ApJS, 234, 39

Sheppard, S. S. 2010, AJ, 139, 1394

—. 2012, AJ, 144, 169

Sheppard, S. S., Jewitt, D., & Kleyna, J. 2006, AJ, 132, 171

Solontoi, M., Ivezić, Ž., Jurić, M., et al. 2012, Icarus, 218, 571

Stetson, P. B. 1987, PASP, 99, 191

Sykes, M. V., Nelson, B., Cutri, R. M., et al. 2000, Icarus, 143, 371

Tera, F., Papanastassiou, D. A., & Wasserburg, G. J. 1974, Earth and Planetary Science Letters, 22, 1

Terai, T., Yoshida, F., Ohtsuki, K., et al. 2018, PASJ, 70, S40

Thirouin, A., & Sheppard, S. S. 2019, AJ, 158, 53

Trilling, D. E., Valdes, F., Allen, L., et al. 2017, AJ, 154, 170

Tsiganis, K., Gomes, R., Morbidelli, A., & Levison, H. F. 2005, Nature, 435, 459

Vaduvescu, O., Macias, A. A., Tudor, V., et al. 2017, Earth Moon and Planets, 120, 41

Valdes, F., & DECam NEO Survey. 2015, in Astronomical Society of the Pacific Conference

Series, Vol. 495, Astronomical Data Analysis Software an Systems XXIV (ADASS XXIV), ed. A. R. Taylor & E. Rosolowsky, 95

Vereš, P., Farnocchia, D., Chesley, S. R., & Chamberlin, A. B. 2017, Icarus, 296, 139

Vladimirovna Pitjeva, E., & Petrovich Pitjev, N. 2015, in IAU General Assembly, Vol. 29, 2256597

Waszczak, A., Ofek, E. O., Aharonson, O., et al. 2013, MNRAS, 433, 3115

Waszczak, A., Chang, C.-K., Ofek, E. O., et al. 2015, AJ, 150, 75

Waszczak, A., Prince, T. A., Laher, R., et al. 2017, PASP, 129, 034402

Wiegert, P., Balam, D., Moss, A., et al. 2007, AJ, 133, 1609

Wolff, S., Dawson, R. I., & Murray-Clay, R. A. 2012, ApJ, 746, 171

Wong, E. W., Brasser, R., & Werner, S. C. 2021, Icarus, 358, 114184

Wright, E. L., Eisenhardt, P. R. M., Mainzer, A. K., et al. 2010, AJ, 140, 1868

York, D. G., Adelman, J., Anderson, John E., J., et al. 2000, AJ, 120, 1579

Yoshida, F., & Nakamura, T. 2007, Planet. Space Sci., 55, 1113

Yoshida, F., Nakamura, T., Watanabe, J.-I., et al. 2003, PASJ, 55, 701

Annexes

Annexed A Transforming Observer's Coordinates to Barycentric Coordinates

Making *tracklets* (collections of detections that resemble a linear trajectory) is easy if you consider detections of only one night, but to link detections from one night to another proves to be challenging (linear fitting does not work all the times and we do not always find a body every night). To solve this, the coordinate reference was changed to the barycenter of our solar system, where the coordinates of the tracklets should resemble straight lines and linear extrapolation to join different bodies would easily work. The problem is that to do this is necessary to know the distance of these bodies to the observer's position or to the barycenter. This meant that you had to assume different distances to look for linear trajectories in the barycentric frame.

Assuming that all detections are at distance r to the barycenter, is necessary to know the position of the Earth in the barycentric frame ($\mathbf{r_E}$) to solve all the geometry. The transformations from the observer's frame to the barycentric frame were done using the module `SkyCoord` from the `astropy` package (Astropy Collaboration et al., 2013, 2018) of `Python`. Once having the equatorial coordinates of the bodies as seen by the observer together with the observer's position, is necessary to measure the distance Δ between the observer and the bodies. Using trigonometry, it is easy to see that Δ is given by equation A2 (solving the quadratic equation given by Equation A1[3]), where ϕ is the elongation (angle between the body and the barycenter)[4].

$$r^2 = r_E^2 + \Delta^2 - 2 r_E \Delta \cos\phi \tag{A1}$$

$$\Delta = r_E \cos\phi + \sqrt{r_E^2 \cos^2\phi - r_E^2 + r^2} \tag{A2}$$

Having the equatorial coordinates from the observer, the observer's position $\mathbf{r_E}$ and the

[3]You could be tempted to replace $r_E^2 \cos^2\phi - r_E^2$ by $r_E^2 \sin^2\phi$ but if you are using `Python`'s `numpy` it will give you large errors for Δ.

[4]`astropy` easily allows us to know the Sun's position seen by the observer, which is corrected by the light's travel time. That is *not* the position you want, but the actual one at observing time. I managed to get this last one by using the observer's position delivered by `astropy.coordinates.EarthLocation` ($\mathbf{r_E}$) transformed to the barycentric frame and then inverting the sign of their cartesian values to get the Sun's position in the observer's frame.

distance from the observer to the body Δ, it is possible to move the origin of the body's coordinates to the barycenter. An example of the kind of equations you need for this are in Bernstein & Khushalani (2000). To make this transformation, we used the simple interface facilitated by `python`'s `astropy.SkyCoord` (along with other `astropy`'s functionality such as "`time`", "`units`", etc). The frame we used is that of the barycentric ecliptic coordinates.

Annexed B Night–to–Night Linking Algorithm

Once having the barycentric ecliptic coordinates for all tracklets (assuming a body-observer distance r), their position were estimated at two different times using a linear fitting on their coordinates. This fit used the corrected time t' approximated by $t' = t - 1/c$, where t is the observed time for each coordinate and c the speed of light.

For each of the estimated times, a neighbor finding routine was performed using a k-d tree algorithm[5] on their estimated coordinates to associate a tracklet to others if their estimated positions were close enough. To cluster one tracklet tr_j to other tracklets ($\{tr_{\mathrm{i}}\}_{\mathrm{i}\neq j}$) it was taken care that in $\{tr_{\mathrm{i}}\}_{\mathrm{i}\neq j}$ there were no tracklets from the same night as tr_j. This did not stop $\{tr_{\mathrm{i}}\}_{\mathrm{i}\neq j}$ from having tracklets in the same night. To manage this problem, the cluster $\{tr_j \cup \{tr_{\mathrm{i}}\}_{\mathrm{i}\neq j}\}$ was divided into as many clusters as necessary so there were no repeated nights in any of the final clusters. Having done this clustering in both times independently, we crossed both sets of clusters to end with a collection where every clustered tracklets must have been clustered in both estimated times. We called any of this final clusters *tracks*.

The times for the estimated positions were chosen to fall at roughly one and three quarters of the total arc of HiTS 2015 survey (57,073 and 57,077 in modified Julian dates). The radius to make the clustering was based on the necessary radius to cluster most of the known bodies that were found among the tracklets without joining tracklets that did not correspond to the known asteroids. The radius that optimized both criteria was found to be 0.01 degrees. Using other radii (namely, getting more tracks in only one night or mixing tracklets that were not the same body) increased the error when estimating orbital parameters (see section 3.4.1).

Since clusters were split so they all were from different nights we could end up with tracklets repeated in more than one cluster. For these cases, we repeated the coordinate estimation process but used estimation times falling at 1/4 and 3/4 of the time arc of the cluster and we measured the maximum distance between estimated positions of the tracklets in the cluster (namely, the *cluster error*). Finally we left the repeated tracklet in the cluster that had the smallest *cluster error* and we removed it from the other clusters it belonged to.

[5]Implemented in `Python` using the `scikit-learn` package (`https://scikit-learn.org/`).

Annexed C Satellite Magnitudes

SIrrs magnitudes were measured for every night they were detected, in each band. Note that in tables C1 and 4.4 are satellites with no observations in g. In those cases the equation 4.2 was solve without the term associated to $g - r$ to transform their fluxes to magnitudes.

Table C1: Satellites' nightly magnitudes

Name	Night	g^a	r^a	i^a	N_g	N_r	N_i
Phoebe	1	16.77 ± 0.03	16.52 ± 0.03	16.47 ± 0.03	70	30	34
	2		16.45 ± 0.03	16.43 ± 0.03	0	34	31
	3	16.76 ± 0.03	16.52 ± 0.02	16.39 ± 0.02	53	27	35
	4		16.47 ± 0.03	16.42 ± 0.03	0	21	27
Siarnaq	1		20.47 ± 0.03	20.26 ± 0.05	0	23	29
	2	21.01 ± 0.04	20.47 ± 0.03	20.19 ± 0.02	41	34	35
	3		20.47 ± 0.03	20.26 ± 0.04	0	26	34
	4	20.99 ± 0.03	20.48 ± 0.02	20.22 ± 0.02	38	18	30
Albiorix	1		21.05 ± 0.04	20.76 ± 0.04	0	13	6
	2	21.66 ± 0.05	21.13 ± 0.05	20.77 ± 0.04	7	34	35
	3		21.07 ± 0.04	20.77 ± 0.04	0	29	18
	4	21.41 ± 0.03	21.03 ± 0.04	20.73 ± 0.04	25	29	11
Ymir	1	22.65 ± 0.03	22.16 ± 0.04	22.09 ± 0.04	49	9	22
	2		22.34 ± 0.07	21.88 ± 0.06	0	14	18
	3	22.85 ± 0.04	22.11 ± 0.05	22.11 ± 0.04	47	35	12
	4		22.38 ± 0.05	21.91 ± 0.03	0	21	20
Tarvos	1	23.37 ± 0.03	22.87 ± 0.02	22.59 ± 0.02	46	22	21
	2		22.90 ± 0.03	22.57 ± 0.02	0	6	9
	3	23.43 ± 0.04	22.81 ± 0.02	22.57 ± 0.02	28	22	23
	4		22.95 ± 0.03	22.58 ± 0.03	0	17	25
Kiviuq	1	23.16 ± 0.03	22.31 ± 0.03	22.12 ± 0.03	50	28	18
	2		22.70 ± 0.03	22.32 ± 0.03	0	10	9
	3	22.85 ± 0.03	22.55 ± 0.03	22.36 ± 0.03	27	12	17
	4		22.40 ± 0.03	22.03 ± 0.03	0	15	15
Paaliaq	1		21.55 ± 0.03	21.26 ± 0.03	0	22	24
	4		21.47 ± 0.03	21.27 ± 0.02	0	27	9
Ijiraq	1	23.88 ± 0.02	23.21 ± 0.03	22.96 ± 0.03	59	27	19
	2		23.14 ± 0.03	23.00 ± 0.03	0	28	18
Skathi	1		24.26 ± 0.03	24.24 ± 0.04	0	18	26
	2	24.54 ± 0.04		24.28 ± 0.02	34	22	35
	4	24.45 ± 0.03			35	14	14
Bebhionn	1		24.68 ± 0.03	24.54 ± 0.03	38	31	29
	2			24.60 ± 0.03	0	7	16
	3		24.65 ± 0.03	24.11 ± 0.03	37	17	22

Notes

[a] Magnitude calculated from the stacked flux at each night.

[b] Number of stacked images per each band.

Table C1 *(continued)*

Name	Night	g^a	r^a	i^a	N_g	N_r	N_i
Erriapus	1		23.36 ± 0.03	23.08 ± 0.04	0	14	19
	2	23.77 ± 0.07		23.60 ± 0.02	47	12	21
	3		24.33 ± 0.03	23.38 ± 0.03	0	20	10
	4	24.00 ± 0.02	23.36 ± 0.02	23.00 ± 0.02	28	12	8
Skoll	1		25.04 ± 0.03		0	18	15
	3		25.00 ± 0.03	24.66 ± 0.03	0	28	30
Hyrrokkin	1		23.98 ± 0.03	23.74 ± 0.04	0	19	22
	2			23.91 ± 0.03	37	28	11
	3		24.04 ± 0.03	23.82 ± 0.04	0	10	28
	4	24.58 ± 0.02	24.22 ± 0.03	23.49 ± 0.03	24	15	5
Mundilfari	1	24.73 ± 0.03	24.25 ± 0.03	24.48 ± 0.03	42	35	24
	2		24.33 ± 0.03	24.32 ± 0.03	0	33	32
	3		24.50 ± 0.03	24.29 ± 0.03	29	26	22
	4			24.23 ± 0.03	0	8	27
Narvi	1	24.75 ± 0.02	24.41 ± 0.03	24.10 ± 0.03	42	21	17
	2		24.56 ± 0.03	24.04 ± 0.03	0	15	32
	3	24.70 ± 0.02	24.47 ± 0.03	23.98 ± 0.03	31	21	26
	4		24.48 ± 0.03	24.14 ± 0.04	0	18	9
Suttungr	1	24.67 ± 0.03	24.43 ± 0.03	24.20 ± 0.03	32	35	31
	2			24.04 ± 0.03	0	21	18
	3	24.78 ± 0.03	24.22 ± 0.03	24.05 ± 0.03	49	28	22
	4			24.35 ± 0.04	0	10	8
Bestla	1			24.29 ± 0.04	0	16	34
	2			24.22 ± 0.02	31	27	26
	3		24.64 ± 0.03	24.12 ± 0.03	0	29	22
	4	25.36 ± 0.03		24.42 ± 0.02	37	22	29
Thrymr	1		24.20 ± 0.03	24.06 ± 0.04	0	14	16
	2			23.95 ± 0.03	33	18	27
	3		24.02 ± 0.03	23.82 ± 0.04	0	15	25
	4	24.48 ± 0.02	24.01 ± 0.03	23.90 ± 0.03	29	30	16
Kari	1	24.95 ± 0.03			55	21	24
	2		24.50 ± 0.03		0	34	23
	3		24.80 ± 0.03	24.12 ± 0.04	26	33	20
Loge	2		24.80 ± 0.03		0	34	19
	3			24.66 ± 0.03	26	14	35
Fornjot	1		25.00 ± 0.03		41	35	31
	3		24.86 ± 0.03		26	24	25
	4			24.73 ± 0.04	0	18	16

Notes

[a] Magnitude calculated from the stacked flux at each night.

[b] Number of stacked images per each band.

Annexed D Aleph: Ephemerides for Asteroids

Whether to plan observations or to look for the coordinates on observed images, having reliable ephemerides of minor bodies is an important part for the study of this bodies. There are some good tools to obtain ephemeris of specific bodies at a given time (such as the services provided by NASA's Jet Propulsion Laboratory, JPL, Horizons[6] and `Miriade`[7], provided by the Institut de mécanique céleste et de calcul des éphémérides, IMCCE, France), but often is necessary to know the minor bodies visible in a given field of the sky at certain time, whichever they are. The latter (which for now on, for simplicity I will call *field ephemerides*) is a necessity not well satisfied in the current astronomical community. That is the reason that I wrote `Aleph`, a public Python's package[8] to obtain ephemerides fast and easily. `Aleph` was designed between the years 2020-2021 in the context of provide good ephemerides to ALeRCE (Förster et al., 2021) to identify if a source classified as asteroid is a known minor body. Currently, ALeRCE works with detections of the Zwicky Transient Facility (ZTF, Bellm et al. 2019), but it is designed (and has been chosen) to be a data broker for the Vera C. Rubin Observatory Legacy Survey of Space and Time (LSST Science Collaboration et al. 2009).

The most important field ephemerides services currently available for the community are the `MPChecker`[9] (of the Minor Planet Center, MPC) and `SkyBoT`[10], (Berthier et al. 2006, hold by the Institut de mécanique céleste et de calcul des éphémérides, IMCCE, France). Although the MPC is probably the most important bank of minor bodies data, holding the observations of these bodies and computing their orbital parameters and ephemerides for their identification, their public service `MPChecker` only delivers ephemerides as seen by an specific observatory code[11], it only allows epoch's accuracy of 0.01 days, its radius of search can not be more than 5°, is not available for automatic or external queries (such as the ones provided by `astroquery`, Ginsburg et al. 2019) and it has an error of $\sim 6''$ (as it can be seen in Figures D1 and 2.2a). `SkyBoT` also computes ephemerides only from specific observatories (the same as MPC), but on the other hand, it allows queries of any radius, epoch's accuracy of fraction of seconds, its errors are below $1''$ (as seen in Figure D1) and it allows automatic and intensive queries (as the one provided by `astroquery`[12]). Up to the last trimester of the 2020 year, when I started working on `Aleph`, JPL Horizons had a similar ephemerides service as the ones named above, but it did not worked (at least for the queries I made and that did work in the other services), but currently (March 2022) it has a working field ephemerides service[13], although it does not have an `astroquery` interface as IMCCE's services and, if its performance is similar to the one observed for specific bodies (see Figure 3.1a) its error would be of $\sim 2'' - 3''$ (much better than MPC's, but not as good as IMCCE's).

[6] `https://ssd.jpl.nasa.gov/horizons/`
`astroquery` interface: `https://astroquery.readthedocs.io/en/latest/jplhorizons/jplhorizons.html`

[7] `http://vo.imcce.fr/webservices/miriade/`

[8] `https://pypi.org/project/astro-aleph/`

[9] `https://minorplanetcenter.net/cgi-bin/checkmp.cgi`

[10] `http://vo.imcce.fr/webservices/skybot/`

[11] `https://minorplanetcenter.net//iau/lists/ObsCodesF.html`

[12] `https://astroquery.readthedocs.io/en/latest/imcce/imcce.html`

[13] `https://ssd.jpl.nasa.gov/tools/sbwobs.html`

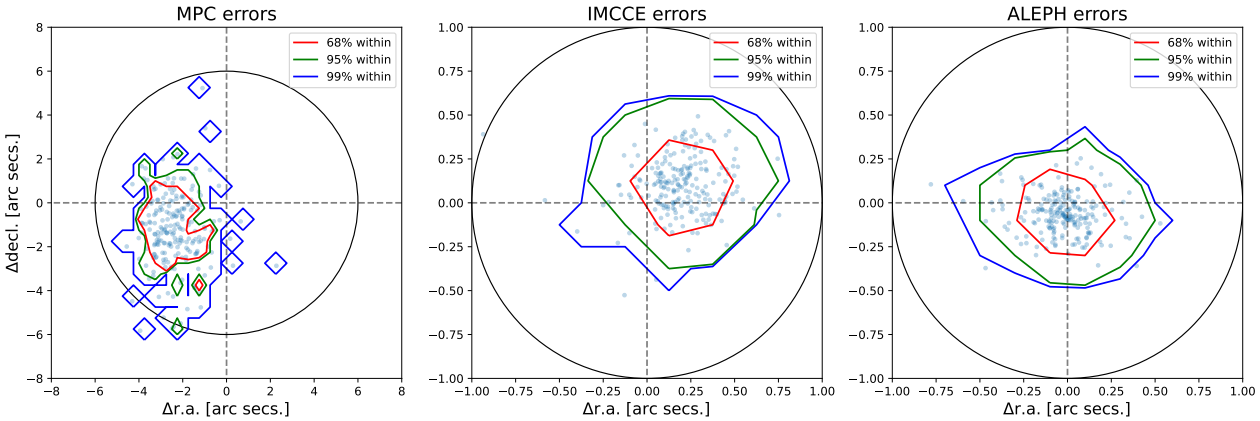

Figure D1: Error on provided ephemeris of different services. The contours indicate the fraction of measurements encircled within. On the left, error of the ephemeris provided by MPC's `MPChecker` (using the coordinates provided by IMCCE's service as the true position, because the low time accuracy allowed by `MPChecker`). On the middle, the error of the ephemeris provided by IMCCE's service (using the coordinates of actual observations by ZTF as true values). On the right, the errors obtained using Aleph (using the same ZTF observations used to evaluate the IMCCE's performance). All ephemerides where obtained in August 2020 for a ZTF's image (observed at 2020-06-16 04:44:58 UTC)

`Aleph` is greatly based in the `astroquery` interface for `SkyBoT`, with the improvements of not needing a connection to the internet (besides the initial installation and acquisition of some minor bodies orbital parameter database), similar to the `astropy`'s functionality to obtain planetary ephemerides, and the ability to compute field ephemerides for an observer located *anywhere* (even outside the Earth). It is written using many of the `astropy`[14] tools, which allowed high flexibility in the input parameters while using methods easily understandable by the astronomical community. The input parameters of a typical query in `Aleph` are:

- `center`: The coordinate of the queried field's center (in equatorial coordinates). It requires an `astropy.coordinates.SkyCoord` object. Using different coordinate frames does not impact the result, since the only values used are the right ascension (r.a.) and declination (decl.) directly extracted from the given coordinates.
- `radius`: The radius of the queried field. It accepts any `astropy.units` value.
- `epoch`: The time of the ephemerides. It requires an `astropy.time.Time` object with the *scale* argument correctly chosen. Internally, all calculations are made in the *Barycentric Dynamical Time* scale. Generally, for ground base observations, the correct scale is *utc* (or maybe *ut1*). Choosing the wrong time scale can reduce the precision of the results to several arc seconds.
- `observer`: The localization of the observer. It can be an `EarthLocation` parameter (part of `astropy.coordinate`), which can be any of the IAU observers or any Earth's position defined by the user. Since it can receive an arbitrary position on Earth, it can also receive the position *anywhere* in the Solar System (such as the one of a space telescope) as long as it is given in coordinates with respect to the Earth; this is very easy using the coordinate transformations provided by `astroquery.coordinate` as long as

[14] `https://www.astropy.org/`

the correct coordinate frames are chosen (`EarthLocation.from_geocentric` receives cartesian coordinates in the *ITRS* frame).

To calculate ephemerides `Aleph` requires a catalog of minor bodies' orbital parameters. The catalogs that accepts are MPC's *MPCORB*[15] and Lowell Minor Planet Services' *astorb*[16]. These catalogs give orbital parameters (in the heliocentric-ecliptic coordinate frame) of the numbered and unnumbered minor bodies at a given epoch. One virtue of astorb over MPCORB is that the former is constantly updated to deliver orbital parameters at an epoch within 50 days from the moment you download the catalog, while the parameters epochs of MPCORB are not unique and can be several months or even years away from the current date. These is important because getting ephemerides by simply integrating the Kepler equations can give very inaccurate results far from the catalog's epoch.

Calculating ephemerides can be separated in two parts: first, being able to integrate the orbits; and second, being able to correct the ephemerides by the light-travel time. The former can be solve in two ways, solving the Kepler equations (fast but inaccurate far from the orbital parameters' epoch) or integrating a more advance model, in this case a model of the Solar System with all the planets as perturbers and the small body as a massless particle (much more accurate but a lot more computational expensive). The later was solved by an iterative process, where the orbit is integrated until the observation time, then is integrated backwards the amount of time corresponding to the light-travel time between the body's position and the observer; that operation is repeated for each body's position until the light-travel time varies less than 1e-10 days from the last iteration. Taking in consideration all the above, `Aleph` computes ephemerides using the following methods:

- *Two-Body Integration*: Orbits are integrated solving the Kepler equations (written in `C`[17], which greatly speeds up the computational time). First, all bodies are integrated until the observation time. Bodies falling in a field centered in the requested field but with a radius 5° bigger are chosen to correct by the light-travel time. Bodies with the latter correction that fall inside the requested field are returned to the user. Solving Kepler equations is very fast, so the computational time is dominated by the correction of the light-travel time. Making that correction only to a fraction of the bodies greatly helps to speed up the results.
- *N-Body Integration*: Orbits are integrated using a model of the Solar System where the planets perturb the body. The model of the Solar System is implemented using `REBOUND`[18] (Rein & Liu, 2012), a `Python` package with different astronomical N-Body integrators (written in `C`, which makes them very fast). In this case, the integrator is the *IAS15* (Everhart, 1985; Rein & Spiegel, 2015) and the model is built with the planets positions obtained using `astropy` and the minor bodies position obtained from their orbital parameters, all of them at the orbital parameters' epoch. Then the algorithm is the same as for the *Two-Body Integration*. In these case, the computational time is dominated by the integration of the model itself, so correcting only a fraction of bodies by the light-travel time does not help much to speed up the calculations. To

[15] `https://minorplanetcenter.net/iau/MPCORB.html`
[16] https://asteroid.lowell.edu/main/astorb/
[17] Based in the `C` codes originally written by Cesar Fuentes.
[18] https://rebound.readthedocs.io/en/latest/

solve that, I implemented a system to integrate all orbits in a grid of times to save the bodies' positions in a large database. Taking the time to integrate everything around the queried epochs allowed to speed up the process by shortening the integration on each query.

- *Mixed Integration*: Finnally, I implemented a method that mixes the ones above. First, all bodies are integrated to the queried epoch using the Kepler equations. Then a sample of bodies falling in a field with a radius 5° bigger than the requested field are selected to be completely integrated and light-travel time corrected using the *N-Body integration*. These method retrieves ephemerides as accurate as the purely *N-Body integration* (see Figure D1) while being greatly faster. The main problem is it has a small probability of missing some bodies if the *Two-Body Integration* send them farther away than 5°. The user can change the radius of the selected bodies to be bigger than 5° to decrease the probability of missing any body. Another option is to integrate all orbits closer to the queried epochs (in the same way as explained for the *N-Body integration*) and transforming those positions to orbital parameters. By default, the program will integrate starting at the stored epoch closer to the queried epoch; in this way, if the orbital parameters are calculated near the queried epoch, the Kepler integration will give small errors and the probability of missing bodies will be small (even small enough to decrease the extra radius below the 5° and reducing even more the computational time of each query).

As indicated, using the combined power of `astropy` and `REBOUND`, `Aleph` delivers ephemerides that can be even more accurate and precise than IMCCE's (the best online field ephemerides service currently available) with the advantage that it does not needs to be connected to the internet. It is more flexible than the discussed public services, since it takes advantage of `astropy` flexibility to set an observer in any coordinate in the Solar System. It was programmed to calculate ephemerides in parallel to speed up as much as possible the execution time. Using ZTF's data around eight months before the astorb's orbital parameter epochs[19], 99% of bodies were cross-matched within 0.8″ of distance, proving that the N-body integration is accurate many months far from the catalog's epoch. It can also calculate ephemerides for user-defined bodies, as long as the provided orbital parameters are in heliocentric-ecliptic coordinates in the MPCORB's or astorb's format.

[19]Using ZTF data from early 2020 and an astorb catalogue downloaded the last trimester of that year.